ANALYSIS OF COULOMB INTERACTION USING MODIFIED PARTICLE–PARTICLE–PARTICLE–MESH METHOD IN MONTE CARLO SIMULATION

BY

WONSOK LEE

DISSERTATION

Submitted in partial fulfillment of the requirements
for the degree of Doctor of Philosophy in Electrical and Computer Engineering
in the Graduate College of the
University of Illinois at Urbana-Champaign, 2011

Urbana, Illinois

Doctoral Committee:

Professor Umberto Ravaioli, Chair
Professor Kanti Jain
Professor Joseph W. Lyding
Professor Narayana R. Aluru

ABSTRACT

We introduce a particle–particle–particle–mesh (P^3M) method modified by a simple yet accurate numerical reference force, which solves the ambiguity of the original P^3M method by effectively eliminating double-counting of pair forces inside the short range. The substantial advantages over the original method are confirmed with extensive verifications.

The modified P^3M method is implemented into an ensemble Monte Carlo (EMC) simulator, MOCA3D, to treat the Coulomb scattering, i.e. carrier-carrier and carrier-impurity scattering. We show that most of the problems in the particle–mesh (PM) based scattering rate approach are solved by the P^3M method. The properties of the Coulomb scattering are analyzed by comparison of the proposed and the conventional approaches.

One of the important observations is that the introduction of discrete dopants in EMC simulation significantly influences the carrier energy and the device performance. The proposed method can also be applied for the random dopant fluctuation (RDF) simulation, in which the accurate treatment of charge granular effect is required.

Furthermore, a 2-D P^3M method is developed based on the 3-D approach. The inherent difficulty in 2-D simulation, due to the line-charge approximation, can be overcome by a quasi 3-D approach. The application results also show the properties and the shortcomings of the 2-D approach.

The validity and the accuracy of the proposed 3-D and 2-D P^3M-EMC simulators are verified with the low-field mobility extraction. We believe that the proposed P^3M approach both in 3-D and 2-D has improved the applicability of the original P^3M method and can be used widely for the calculation of inter-particle forces.

I dedicate this thesis to my wife, Yuri.

ACKNOWLEDGMENTS

First of all, I would like to thank my adviser, Professor Umberto Ravaioli, for his guidance and advice throughout my graduate study.

I also want to thank those who have participated for decades in the development of a Monte Carlo simulator MOCA. This work would not have been possible without the previous efforts that have been made by many previous and current graduate students. I would also like to thank past and current members of the Computational Multiscale Nanosystems Group including Mohamed, Zlatan, Hyung-Seok, Pierre, Kyung-Hyun, Fawad, and Michael.

I'm grateful to Samsung Electronics for financial support and to colleagues in the CAE team, including Jeong-Taek Kong, Young-Kwan Park, and Keun-Ho Lee, who have made all things possible.

I would also like to thank my son Aiden and new-born daughter Alaina for having been so nice and giving me and my wife enormous happiness. Finally, I wish to thank all my family members for their enthusiastic support and encouragement over the years.

TABLE OF CONTENTS

LIST OF TABLES

LIST OF FIGURES

CHAPTER 1

INTRODUCTION

Traditionally, continuous down-scaling of the semiconductor device dimension has been the main reason for the improvement of device performance and the reduction of cost per unit [1]. However, the applied bias has not been reduced enough and thus the electric field inside the device has increased significantly. Therefore, the high-energy carriers have caused problems including hot carrier effects such as gate oxide leakage and impact ionization. Moreover, the complexity of devices has increased significantly with the introduction of novel devices such as double-gate transistors, trigate, and surround-gate-transistor (SGT) to improve the device performance and to reduce the short-channel effects [2–7].

Relentless scaling and the increase of complexity are challenges not only for device integration but also for device simulation. To cope with the increased electric field, drift-diffusion (DD) based methods have been improved by hydrodynamic (HD) and energy-transport approaches. However, these continuum based approaches have had difficulties incorporating the sophisticated effects of underlying physics in highly scaled devices [8].

One of the critical issues is the consideration of Coulomb scattering, i.e. carrier-carrier scattering and carrier-impurity scattering, in highly scaled semiconductor devices. While other predominant scatterings, e.g. phonon scattering, have decreased along with the scaling of device dimensions, Coulomb scattering has become relatively more important [9]. Increased current density results in more frequent interactions between carriers, and heavily doped source/drain combined with short-channel makes the carrier-impurity scattering inside the contact more influential. Random dopant fluctuation (RDF) also needs to be analyzed properly to examine the stochastic variation of device performance [10, 11].

Generally, charge carriers and ionized impurities have been treated as charge densities on

the mesh nodes. However, for highly scaled nanoscale devices, a more sophisticated model is required to capture the granular effect of each charge particle. Historically, Coulomb scattering has been treated using the scattering rate method based on Fermi's golden rule. However, there have been many problems associated with the approach [12, 13].

In this study, we apply the semiclassical particle–particle–particle–mesh (P^3M) approach, an alternative method, to account for accurate inter-particle forces. The concept of the P^3M method is very straightforward and easy to understand. However, P^3M has not been considered a popular method for the electrostatic force calculations between charge particles in semiconductor simulations. One of the main reasons comes from the uncertainty in determining net pair forces inside the short range [14, 15].

In this work, the uncertainty of the original P^3M method is eliminated by introducing a novel numerical method. The proposed method is verified under various conditions including non-uniform meshes. After the benchmark of the proposed method, we integrate it into an ensemble Monte Carlo (EMC) simulator for the device simulation. We also present a comprehensive analysis of carrier-carrier scattering and carrier-impurity scattering utilizing P^3M-EMC.

The physical background of transport and electrostatic simulation using the Monte Carlo approach is presented in Chapter 2. In Chapter 3, the properties of carrier-carrier scattering and carrier-impurity scattering are discussed. The limitations of the conventional scattering rate method for the Coulomb scattering are also presented. An alternative, the P^3M method, is introduced based on the basis of the particle–particle (PP) and the particle–mesh (PM) methods. The strengths and the practical issues of the original P^3M method are discussed and we introduce a modified P^3M method to cope with the problem. The validity and the accuracy are confirmed with various examples. In Chapter 4, the modified P^3M method is integrated into the P^3M ensemble Monte Carlo (EMC) simulator. The strengths of the P^3M method over the PM based scattering rate method are discussed. The influence of carrier-carrier and carrier-impurity scattering is examined. The validity of the method is examined with the low field mobility extraction.

Finally, in Chapter 5 we introduce a 2-D P^3M method. The equations required for 2-D P^3M are presented and tested for 2-D EMC simulations. The practical problem due to the line charge approximation is solved with a quasi 3-D approach. The properties of 2-D EMC simulation and its shortcomings are discussed.

CHAPTER 2

MONTE CARLO METHOD

As a result of continuous scaling and increasingly complex device structure, it has become more difficult to incorporate underlying physics into device simulation. Many efforts have been made to capture the sophisticated effects in modern, highly scaled devices. However, simulation tools still have difficulties in taking into account these effects [8].

Figure 2.1 shows the hierarchy of the device simulation models. The well-known drift-diffusion (DD) approach [16] has been improved by so-called the energy-transport or hydrodynamic (HD) model [17, 18] to capture hot carrier effects and velocity overshoot in small devices [19, 20]. In recent decades, the device characteristics have been represented by the DD and the HD models using fitting parameters. However, in nature these approaches are insufficient for highly scaled devices in which a more rigorous physical basis is required. Accordingly, the lack of underlying physics has continuously caused problems in new technology nodes, and it has been getting harder to predict device characteristics of the next technology generation.

Another approach is to utilize a full quantum mechanical method which treats the wave nature and interference of carriers. This is the most rigorous approach in the hierarchy of device models, as shown in Fig. 2.1. However, such a full quantum approach has not been mature enough to be applied to practical device simulation [8].

In between, there is a method known as a very practical approach: the Boltzmann transport equation (BTE) based method, which is accurate up to the semiclassical limit. The BTE based method can be explained as follows.

In a semiconductor device, the device characteristics can be determined by carrier positions both in real space and in momentum space. Alternatively, we can use the probability

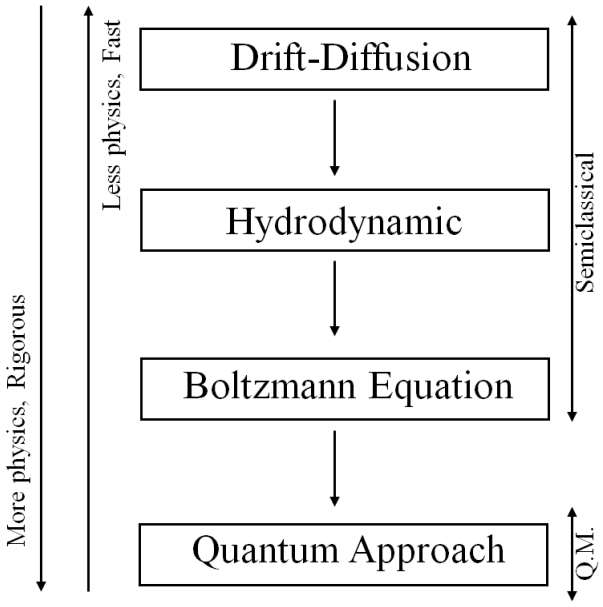

Figure 2.1: Hierarchy of semiconductor device simulation models.

of finding a carrier with wave vector $\mathbf{k}$, at position $\mathbf{r}$, and at time $\mathbf{t}$. This can be referred to as the distribution function, $f(\mathbf{r}, \mathbf{k}, \mathbf{t})$, which is a number between zero and one. In order to find the distribution function, we need to solve the semiclassical BTE, which is basically based on the simple charge conservation [21], described by

$$\frac{\partial f}{\partial \mathbf{t}} + \mathbf{v} \cdot \nabla_{\mathbf{r}} f + \frac{\mathbf{F}}{\hbar} \cdot \nabla_{\mathbf{k}} f = \frac{\partial f}{\partial \mathbf{t}}|_{coll} \tag{2.1}$$

where

$$\frac{\partial f}{\partial \mathbf{t}}|_{coll} = \sum_{\mathbf{k}'} [s(\mathbf{k}', \mathbf{k}) f(\mathbf{r}, \mathbf{k}', \mathbf{t}) - s(\mathbf{k}, \mathbf{k}') f(\mathbf{r}, \mathbf{k}, \mathbf{t})] \tag{2.2}$$

Here, $\mathbf{r}$ is the position, $\mathbf{v}$ is the velocity, $\mathbf{F}$ is the electric field, $\mathbf{k}$ is the wave vector, and $s(\mathbf{k}', \mathbf{k})$ represents transition probability from state $\mathbf{k}'$ to $\mathbf{k}$.

Simpler methods, such as the DD model and the HD model, are also based on the approximations of BTE. The left-hand side shows the dependence of the distribution function

on time, space, and momentum. The right-hand side takes into account the collision term, which accounts for all the scattering events as in equation (2.2) that will be discussed later. With the distribution function, we can obtain various quantities of interest such as carrier density, current, and energy of carriers [22]. However, solving BTE is only viable for very limited cases due to the complexity of the equation which is a integro-differential equation with seven variables including time, 3-D space, and 3-D momentum [22].

An alternative equivalent method of solving the BTE is Monte Carlo (MC) simulation [13, 23, 24]. It stochastically solves the equivalent problem with the BTE by tracking the individual carrier trajectories in momentum and in real space as a function of time [25]. Considering the complexity of the BTE, the MC method is very simple and straightforward. It treats carriers as point-like semiclassical particles moving within a device under the action of electric field and interrupted by scattering events [13, 26–28]. Instead of storing all the information, the MC simulator only stores average values by sampling the data with a given time interval. The statistical noise can be reduced by increasing the number of samples. By simulating a large number of carriers or increasing the number of iterations, one can make the results represent the behavior of the carriers in a real device [22].

The MC simulation is known as one of the most accurate methods and it is frequently used as a standard tool to measure the validity of simpler approaches including DD and HD. Because MC simulation directly mimics the physics, an understanding of the technique is also helpful for the insight it affords [22, 29, 30]. For many years, due to the computational expense, the MC method has been used only for limited applications. However, the advances in computational power and the need for physically based simulation have made the MC method a more general technique to investigate the characteristics of semiconductor devices.

This work is based on MOCA, which is the MC simulator of the Computational Multiscale Nanosystems Group at the University of Illinois at Urbana-Champaign. It has been developed over two decades and many notable results have been obtained throughout the development [31–33]. Full-band structure was introduced to cope with the increased electric field in highly scaled devices. Quantum correction was included in the semiclassical frame-

work to capture the size quantization effect, which extended the validity of semiclassical MC simulation to the 10 nm regime [34]. MOCA3D has been developed to account for the miniaturization and 3-D effect of the novel structures [34–36].

2.1 Band Structure Models

It is important to include the influence of crystal on the behavior of carriers. As one can expect, the carrier motion is more complicated in semiconductor crystal than that in free space due to the interactions with the periodic atoms of the crystal lattice [37].

The influence of the crystal can be accounted for by the band structure, which describes the relationship between energy and the wave vector $\mathbf{k}$. This gives detailed information about the energy and velocity of the carrier under the action of electric field, density of states (DOS), scattering rate, and final state selection after scattering [8, 34]. In order to understand the concept of the band structure, we generally assume parabolic energy bands:

$$E_n(\mathbf{k}) = \frac{\hbar^2 \mathbf{k}^2}{2m_n^*} \tag{2.3}$$

$$\frac{1}{m_n^*} = \frac{1}{\hbar^2} \frac{\partial^2 E_n(\mathbf{k})}{\partial \mathbf{k}^2} \tag{2.4}$$

where $E_n(\mathbf{k})$ represents energy at wave vector $\mathbf{k}$ in band n, $\hbar$ is the reduced Plank constant, and m_n^* is an effective mass for carriers in band n.

However, parabolic band structure is too simple to provide reasonable results except for relatively low field applications since this approximation is only valid near the bottom of the conduction band or the top of the valence band [38].

Equation (2.5) shows nonparabolic band structure, which includes the warping of the band.

$$E_n(\mathbf{k})(1+\alpha E_n(\mathbf{k})) = \frac{\hbar^2\mathbf{k}^2}{2m_n^*} \tag{2.5}$$

where α is a parabolicity factor given by

$$\alpha = \frac{1}{E_g}\left(1 - \frac{m_n^*}{m_0}\right) \tag{2.6}$$

where E_g is the band gap. Unlike the parabolic band structure, the nonparabolic band structure shows reasonable accuracy for moderate field applications, but it also can be problematic as the second conduction band appears in high energy.

Consequently, sophisticated full-band structure is important at very high field applications [8, 10]. There is no analytical description for the full-band structure and it should be calculated by numerical methods. One of the most popular methods is the empirical pseudopotential method [27,39,40], which is also applied for the calculation of the band structure in MOCA. Figure 2.2 shows an example of silicon band structure, which is pre-computed and tabulated in MOCA for convenience. The energy and its gradient are calculated for the $\mathbf{k}$ points inside the irreducible wedge (see Fig. 2.3) of the Brillouin zone [34].

$$\mathbf{0} \le \mathbf{k_z} \le \mathbf{k_x} \le \mathbf{k_y} \le \mathbf{1} \tag{2.7}$$

$$\mathbf{k_x} + \mathbf{k_y} + \mathbf{k_z} \le \frac{\mathbf{3}}{\mathbf{2}} \tag{2.8}$$

The irreducible wedge only covers 1/48 of the Brillouin zone, but all points in the Brillouin zone can be mapped to the irreducible wedge by symmetry operations [28]. The density of states (DOS), which is crucial for the scattering rate calculation, is also based on the band structure. Figure 2.4 shows the DOS for conduction bands up to 5 eV.

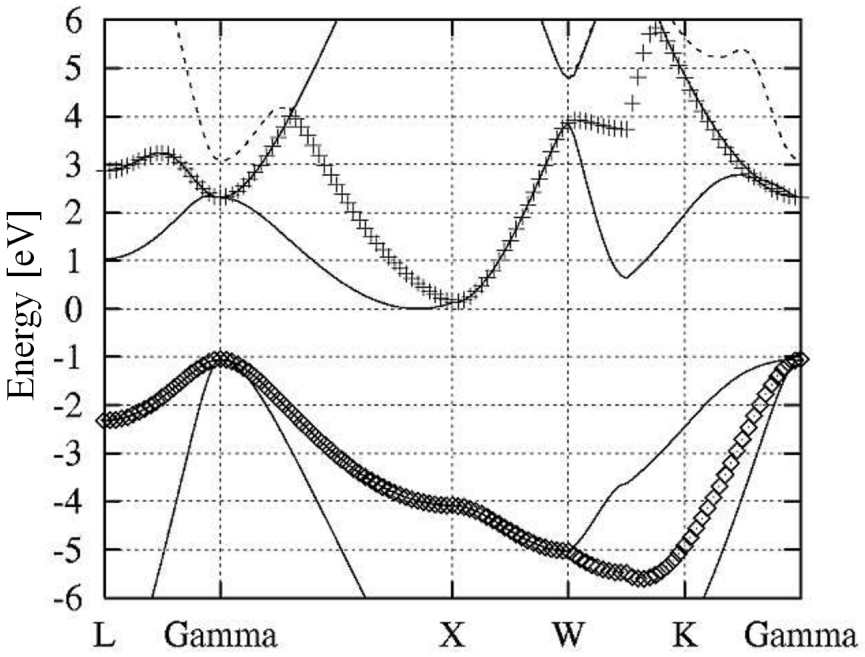

Figure 2.2: An example of an electronic full-band structure for silicon.

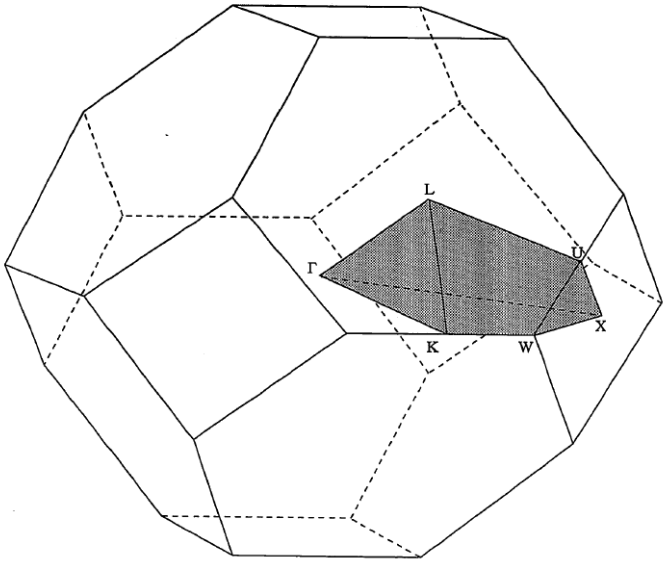

Figure 2.3: The first Brillouin zone of the face centered cubic lattice. The shaded region is the irreducible wedge. The labels show important symmetry points. Γ is the zone center, X is the endpoint in [1,0,0] direction, L is the endpoint in [1,1,1] direction, and K is the endpoint in [1,1,0] direction.

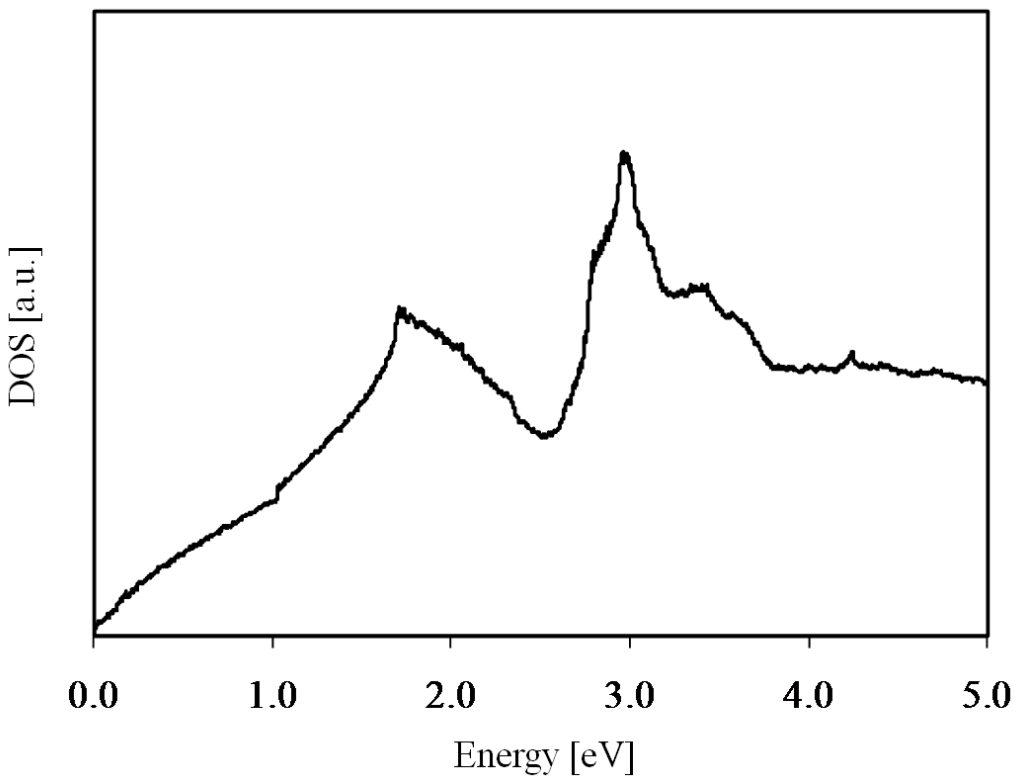

Figure 2.4: Density of states (DOS) for the silicon conduction bands.

2.2 Equations of Motion (Kinematics)

Except for the difference in mass, the motion of electrons in a crystal can be described by the classical equations of motion [10]. The velocity and the momentum of the carriers between the scattering events are governed by the semiclassical Newton's mechanics:

$$\frac{d\mathbf{r}}{d\mathbf{t}} = \frac{1}{\hbar}\nabla_{\mathbf{k}} E_n(\mathbf{k}) \tag{2.9}$$

$$\frac{d\mathbf{k}}{d\mathbf{t}} = \frac{q\mathbf{F}(\mathbf{r},\mathbf{t})}{\hbar} \tag{2.10}$$

where $\mathbf{k}$ is the carrier's wave vector, $\mathbf{F}$ is the electric field, $\mathbf{r}$ is the carrier position, $E_n(\mathbf{k})$ is the energy of the carrier at wave vector $\mathbf{k}$ in band n, $\hbar$ is the reduced Plank constant, and q is the electric charge. From the quantum mechanical point of view, the first equation gives the group velocity of the electron wave-packet. The introduction of sophisticated $E(\mathbf{k})$ relation in the equation, i.e. full-band structure, makes the motion of a carrier more complicated than the motion of a free carrier. The second equation represents conservation of energy. The above carrier dynamic is true based on the assumption that the potential energy felt by electrons varies slowly compared to the crystal potential so that quantum mechanical effects such as reflection can be ignored [10, 41].

2.3 Scattering Mechanism

Free flights of the carriers are interrupted by scattering events which limit the velocity of charge carriers. In MOCA, most of the important scattering mechanisms are considered, including intravalley acoustic phonon, f- and g-type X-X and X-L intervalley optical phonon scattering, ionized impurity scattering, impact ionization [42, 43], and surface roughness scattering. In this thesis, the emphasis is on the Coulomb scattering such as carrier-carrier scattering and carrier-impurity scattering, which will be discussed in detail in the following chapters.

Throughout the MC simulation, random numbers are generated to determine free flight times for all charge carriers. For a carrier, a scattering occurs at the end of free flight and a scattering mechanism is determined by another random number. Figure 2.5 illustrates random selection of scattering mechanism. In MOCA, the scattering rates are pre-computed and tabulated for random selection. In the event of scattering, a certain scattering mechanism is selected to determine the final energy and the momentum of the carriers. In general, the total scattering rate is fixed to a higher value than the actual physical scattering rate to simplify the overall calculation [44]. The difference between total scattering rate and real scattering rate is denoted as self-scattering, which is not a physical scattering and thus does

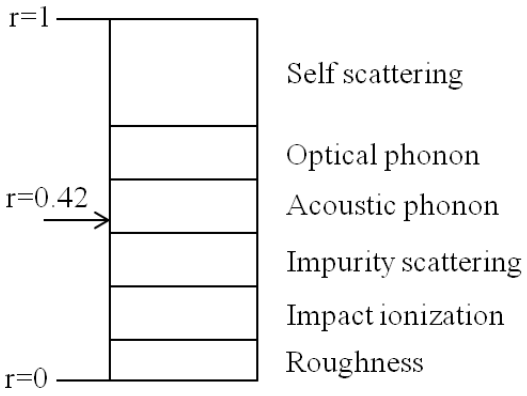

Figure 2.5: Illustration of determination of scattering mechanism with random number r.

not change any property of the carrier including wave vector $\mathbf{k}$.

In physical scattering, the position in real space will not change by the instantaneous scattering events, but the wave vector $\mathbf{k}$ can change abruptly depending on the scattering mechanism. An electron can lose or gain energy by inelastic scattering such as phonon emission or absorption, respectively. However, the energy of an electron will not change by elastic scattering such as ionized impurity scattering.

The scattering rate method is based on Fermi's golden rule. Transition probability and corresponding scattering rate can be obtained by

$$S(\mathbf{k}, \mathbf{k}') = \frac{2\pi}{\hbar} \left|\mathbf{H}_{\mathbf{k}',\mathbf{k}}\right|^2 \delta[E(\mathbf{k}') - E(\mathbf{k}) - \Delta(E)] \tag{2.11}$$

$$\frac{1}{\tau(\mathbf{k})} = \sum_{\mathbf{k}'} S(\mathbf{k}, \mathbf{k}') \tag{2.12}$$

where $S(\mathbf{k}, \mathbf{k}')$ is the transition probability from state $\mathbf{k}$ to $\mathbf{k}'$, and $\mathbf{H}_{\mathbf{k}',\mathbf{k}}$ is the matrix element of the corresponding scattering mechanism. Dirac δ-function stands for the conservation of energy and $\tau(\mathbf{k})$ is the average time between scattering. Therefore, $1/\tau(\mathbf{k})$ represents the scattering rate.

Another approach to calculate the Coulomb scattering, e.g. ionized impurity scattering and carrier-carrier scattering, is the semiclassical particle–particle–particle–mesh (P^3M) method. More detail about the P^3M method will be presented in the following chapter.

2.4 Quantum Correction

Due to the quantum confinement of highly scaled devices, the electron concentration peak is lower than the silicon-oxide interface. This is in contrast to the classical model in which the peak is at the interface. This quantum-mechanical behavior of the inversion layer changes the characteristics of a MOSFET. Threshold voltage increases as more band bending is required to populate the lowest subband. Transconductance and the drive current decrease as the effective oxide thickness slightly increases as a result of quantum confinement [45, 46].

Quantum correction is a process to incorporate these effects in classical MC simulation [47]. As a result, the validity of the conventional MC simulation can be extended to the 10 nm gate length regime [34]. Several different approaches can be applied for the quantum correction, which is discussed in detail by Winstead [35]. In MOCA, a Schrödinger equation based quantum correction model is implemented [34, 35]. Quantum correction potential can be described by

$$V_{qc}(y,z) = -k_B T_t \log[n_q(y,z) - V_p(y,z) + V_0] \tag{2.13}$$

where $n_q(y,z)$ is the carrier density from the solution of the Schrödinger equation, T_t is the transverse temperature, $V_p(y,z)$ is the potential from the Poisson equation, and V_0 is a reference potential point in the device where the quantum correction becomes negligible. The obtained results agree well with the results by the reference approach, the Schrödinger-Poisson solver [34].

2.5 Electrostatic Simulation

Throughout the MC simulation, the field equation needs to be solved with a certain time interval to obtain the electrostatic potential and field. This procedure is essential to maintain the self-consistency with the carrier transport simulation. The solution of Poisson's equation yields mesh-defined electrostatic potential, and the electric field can be obtained by the differentiation of obtained potential. In order to find the driving force at the position of a carrier, an interpolation technique is applied based on the mesh-defined electric field.

To solve the problems on the mesh nodes, it is necessary to assign charge on the mesh nodes.

Here we explain three popular charge assignment schemes. The charge assignment scheme includes the nearest-grid-point (NGP), the cloud-in-cell (CIC), and the triangular-shaped-cloud (TSC) as shown in Fig. 2.6. The order of the charge assignment scheme increases as we change the method from NGP to CIC and to TSC, and thus more mesh nodes are involved. Among them, CIC is the most popular method for the Monte Carlo simulation. The CIC scheme assumes, for example in 3-D, that a charge is uniformly distributed in a volume of the mesh cell. As explained above, the electric field at the particle position can be obtained by interpolation of the electric field on the mesh. It is important to note that the interpolation scheme should be consistent with the charge assignment scheme to prevent the self-force problem. The following shows the Poisson equation for the electrostatic potential and the differential equation for the electric field:

$$\nabla(\epsilon\nabla\phi) = -\rho(\mathbf{r}) \tag{2.14}$$

$$\mathbf{F} = -\nabla\phi \tag{2.15}$$

where $\rho(\mathbf{r})$ is the charge density, ϵ is the dielectric permittivity, ϕ is the electrostatic potential, and $\mathbf{F}$ is the electric field. In MOCA, the nonlinear Poisson's equation is solved with the Newton method, using the conjugate-gradient technique, and a line search approach is used to determine the steepest descent direction [48].

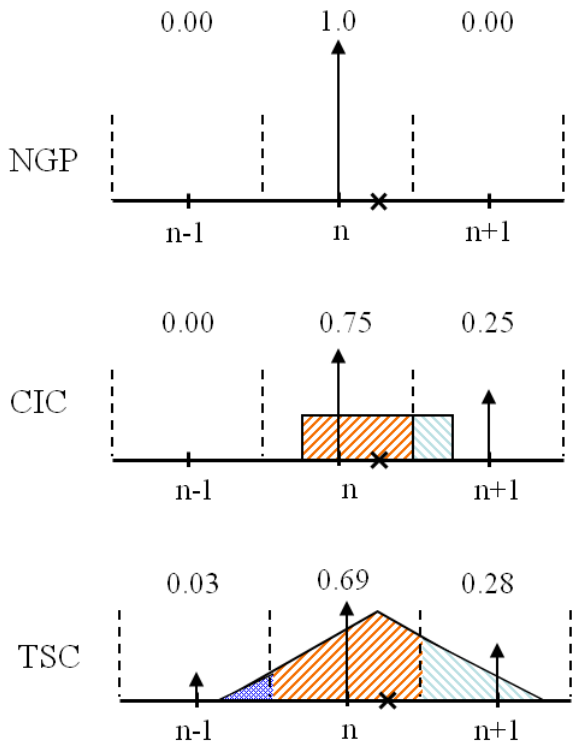

Figure 2.6: Illustration of charge assignment schemes in 1-D example [49]. In this example, the position of a particle is assumed to be at 1/4 distance from node n to n+1. Vertical arrows and numbers above represent the amount of charge assigned with the configuration.

2.6 Self-Consistent Ensemble Monte Carlo (EMC) Simulation

In order to apply the MC simulation to a device, there are several things that have to be taken into account. Boundary conditions need to be determined to solve the Poisson equation based on the device configuration and applied bias. Dirichlet boundary conditions are applied where the specific bias conditions are given. Generally, Neumann boundary conditions are applied for the other boundaries [10].

The weight of a charge can be decided depending on the situation. In the past, super-particles, which have charge weight larger than 1, are commonly used to reduce the number of charges considering the limited computational power. As the device scaling continues and fewer carriers are involved, a fractional weight scheme, i.e. charge weight less than 1, is commonly used to reduce the statistical variance. In this case, however, the screening effect

can be over-emphasized and interactions between carriers and between carrier and impurities cannot be calculated properly [36]. In this study, unit weight for a charge is applied throughout the simulation to capture the forces between charge particles correctly.

Time step and mesh size also need to be carefully determined based on the device characteristics and computational complexity. Time step is related to the plasma frequency to capture the plasma fluctuation inside the heavily doped regions such as source and drain of the MOSFET. The mesh size needs to be determined by the charge variations and the importance of regions for device performance [10].

The overall procedure of the transport simulation using the EMC simulator is described in Fig 2.7. Based on the information given in the input files, the MC simulator initializes the problem with an ensemble of charge particles. The electric field can be calculated by potential obtained using Poisson's solver and the influence of the semiconductor crystal can be included by band structure and effective mass. The position and the momentum of the carriers are determined by Newton's mechanics. The motion of the carriers is interrupted by scattering events and final states are determined by the properties of scattering mechanisms. These steps are repeated until the system reaches steady state or until the maximum given iteration number. Based on the gathered data during the simulation, we can observe various device characteristics including carrier density, current, and energy of the carriers.

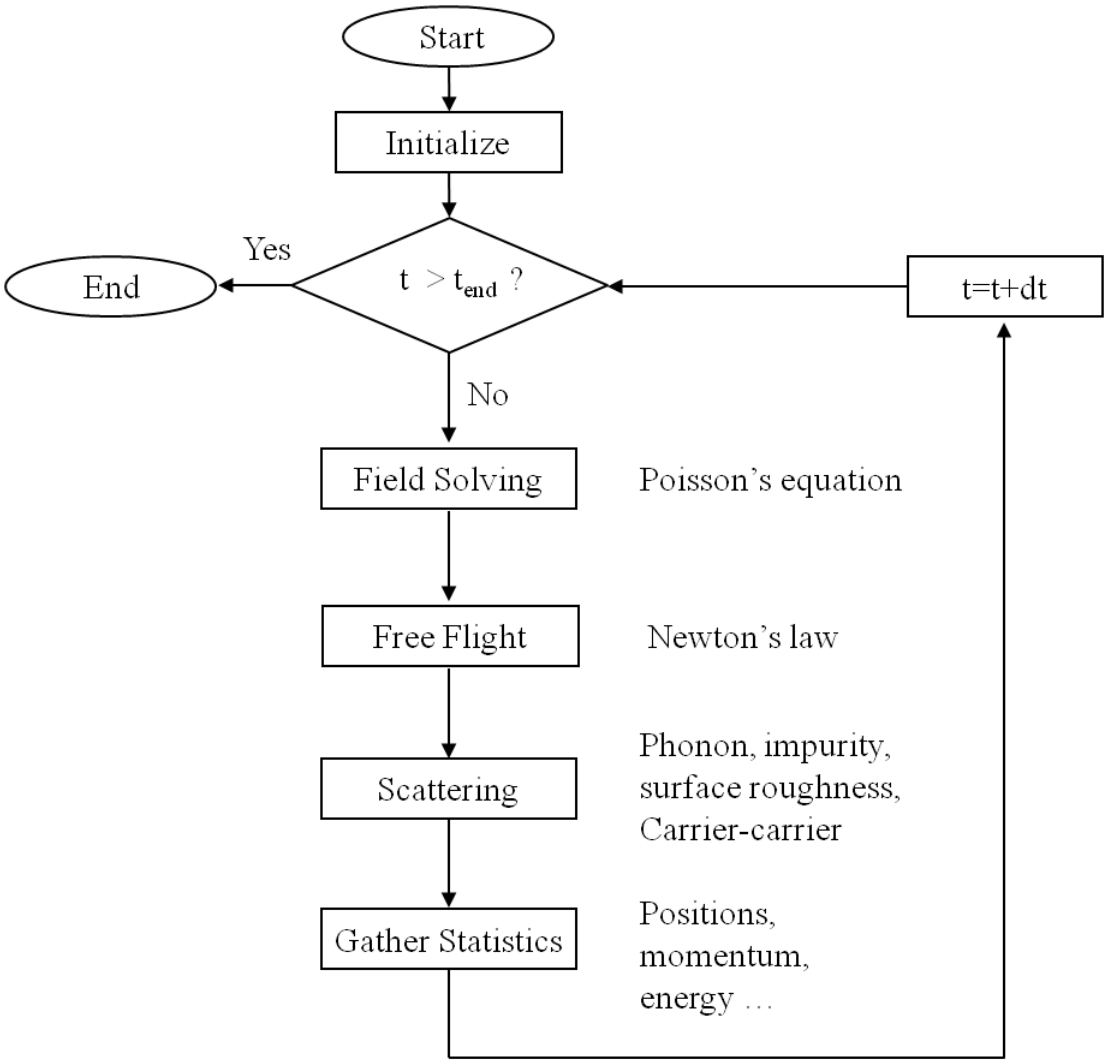

Figure 2.7: Flowchart of the self-consistent ensemble Monte Carlo (EMC) simulation.

CHAPTER 3

MODIFIED PARTICLE–PARTICLE–PARTICLE–MESH METHOD

Coulomb scattering, including carrier-carrier and carrier-impurity scattering, is considered to be more important to device performance due to increased current density and highly doped source and drain regions. [9, 10]. This chapter deals with the methods that can be used to treat the Coulomb scattering. The properties and the limitations of the methods will be discussed. Finally, the modified P^3M method will be presented and evaluated to confirm the accuracy and the efficiency.

3.1 Fermi's Golden Rule Based Scattering Rate Method

Generally, both carrier-impurity and carrier-carrier scattering mechanisms have been treated by the Fermi's golden rule based scattering rate approach. The properties of each scattering mechanism are as follows.

3.1.1 Carrier-impurity scattering

Ionized impurity scattering (see Fig. 3.1) is an elastic scattering in the sense that a fixed impurity ion is much heavier than an electron and thus an ion is not affected by the interaction with an electron. In addition, impurity scattering is an anisotropic scattering, which means that the direction of a scattered electron is a function of the direction before the scattering. Note that an isotropic scattering implies that the scattered electron has the same probability of being in any direction after scattering, which is true, e.g., for most phonon scattering except polar optical phonon scattering [10]. Impurity scattering prefers small angle scattering

and the wave vector **k** also needs to be determined considering the scattering angle. The details may be found in [10]. In MOCA, the wave vector **k** is determined using the parabolic band model and the corresponding energy is selected from the full band model [12]. Even with the basic assumption of elastic scattering, a small change of energy after scattering is inevitable considering the procedure. If the final state energy is outside the specified energy range, the simulator selects a different wave vector **k** to make the scattering satisfy the energy conservation condition.

One of the most important properties which needs to be considered for Coulomb scattering is the screening effect. The electrostatic force by an isolated charge is coulombic. However, the force in a crystal can be quite different depending on the density of surrounding free carriers. Basically, the impact of an ionized impurity scattering decreases as the screening gets stronger since more mobile carriers will screen out the influence of ionized impurities. Therefore, the screening is strong when the carrier density is high and is weak when the carrier density is low. This effect on ionized impurity scattering has been included by screening potential in two different approaches: the Conwell-Weisskopf (CW) model and the Brooks-Herring (BH) model. Later, Ridley combined two models [50] in a way that reduces to the CW model when the screening is weak or to the BH model when the screening is strong. In MOCA, Ridley's model is implemented to treat the impurity scattering.

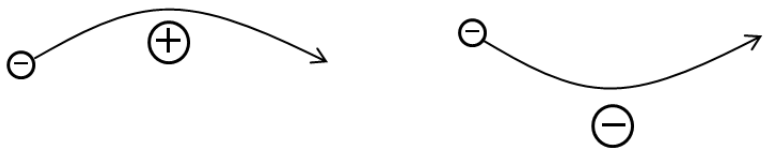

Figure 3.1: Illustration of scattering between an electron and ionized impurities. In scattering rate approaches, unlike as in the illustration, ions are represented as charge densities on the mesh rather than point charges and the scattering is an instantaneous event. The momentum and the energy before and after the scattering need to be conserved; i.e., k=k' and E=E'.

3.1.2 Carrier-carrier scattering

During the carrier-carrier scattering as in Fig. 3.2, the total momentum and energy before and after the scattering are considered to be conserved. However, the scattering may redistribute the energy and the momentum between carriers. Therefore, the carrier interactions are expected to show secondary effects rather than direct influence on the device performance.

Carrier-carrier scattering can be divided into long-range scattering and short-range scattering. Long range carrier-carrier scattering can be implicitly considered by the solution of self-consistent Poisson's equation [10]. In MOCA, the short-range carrier-carrier scattering based on the scattering rate method has not been implemented due to the ambiguity of the method, the difficulties of the implementation, the computational complexity, and the uncertainty of the impact on device performance [51].

In general, many attempts have been made to include short-range carrier-carrier scattering including DAMOCLES [8], but none of them has been satisfactory so far. The details of the method in [8] can be found in [19].

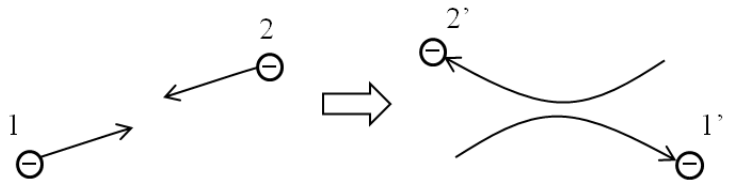

Figure 3.2: Illustration of scattering between electrons. In scattering rate approaches, unlike the illustration, the scattering is an instantaneous event. The total momentum and the energy before and after the scattering need to be conserved; i.e., k1+k2=k1'+k2' and E1+E2=E1'+E2'.

3.1.3 Issues with the scattering rate approach

Even though the scattering rate based method is the most popular approach, there are serious issues with the method [36]. It is well known that carrier-carrier scattering in Monte Carlo

simulation is extremely difficult to treat [14,15,19]. Unlike other scattering mechanisms, the analytical expression for carrier-carrier scattering as in [19] is a function of local distribution function, which is unknown at the moment of evaluation. This makes the problem nonlinear and increases the computational complexity.

In the case of impurity scattering, the ionized impurities are considered as charge densities on the mesh, which is far from the reality and makes it harder to capture the discreteness of the dopants. Therefore, the granular effects including RDF are difficult to treat with the approach. Typically, only a two-body problem can be considered as an instantaneous scattering event. In reality, however, many bodies are involved and they are interacting continuously with each other. In addition, as discussed earlier, screening is a very important property that needs to be considered properly, but it is almost impossible to consider various and dynamic screening situations with analytical approximations such as Debye approximation to find the screening parameter. Besides, the scattering rate approach does not consider the type of the dopants. Depending on the nature of the forces, however, the interaction and the influence can be different, which will be discussed in detail in the following chapter.

One of the most critical but not well-known problems is double-counting of the scattering effect especially for the carrier-carrier scattering in 3-D. The interaction can be treated by Poisson's solution with the application of a fine mesh. In a coarse mesh, on the other hand, the interaction cannot be captured properly with the self-consistent Poisson's solution. However, the scattering rate and the final state after the scattering are not functions of mesh size. As a result, the amount of double-counting is a function of local mesh size and thus it is extremely difficult to estimate the double-counting and eliminate it.

3.2 Alternative Approach: P^3M Method

One of the alternatives for Coulomb scattering is the particle–particle–particle–mesh (P^3M) algorithm [12,49]. In this method, the short-range forces are calculated directly by Coulomb's law and the long-range forces are obtained by the self-consistent Poisson's equation. In the

classical limit, P^3M is the most attractive method since it combines the merits of the particle–particle (PP) and particle–mesh (PM) methods [12, 49].

3.2.1 Particle–particle (PP) method

One of the simplest ways to calculate forces between particles is to use the PP method as shown in Fig. 3.3. For charge particles, we can use Coulomb's law to calculate forces on primary particle i by associated partner particle j as follows:

$$F_{ij}^{coul} = \frac{q_i q_j}{4\pi\varepsilon} \frac{(r_i - r_j)}{|r_i - r_j|^3} \tag{3.1}$$

where q_i and q_j are charges of the particles, and r_i and r_j are the particle positions. If more than one partner particles are involved as in Fig. 3.3, the superposition of the forces can be applied for the total short-range interparticle forces on i.

The PP method is straightforward, accurate, and easy for the implementation. The biggest shortcoming of the method is that the CPU time for the PP calculation is proportional to the square of the number of involved particles. Thus, the PP method is viable only either for small systems or for large systems in which long-range inter-particle forces can be neglected [49]. Another problem is that the information, e.g. the electric field, is only

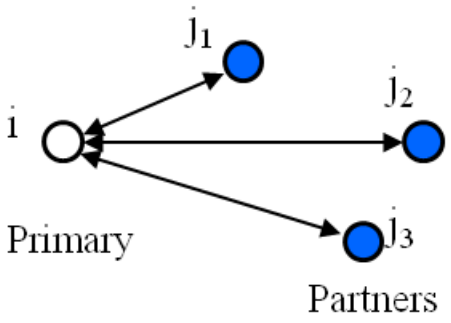

Figure 3.3: Illustration of the PP method. The inter-particle forces can be evaluated by Coulomb's law between particles.

available at the position of the particles. Therefore, unlike with the PM method, it is hard to get the information for the whole simulation domain. One of the notable properties of the method is that the external forces, i.e., the forces due to the boundary conditions, need to be considered by separate procedure [11]. The significance of the property in this study will be discussed later.

3.2.2 Particle–mesh (PM) method

The force between particles can also be calculated using the PM method as illustrated in Fig. 3.4. Unlike the PP method, in which the particle positions are used, the PM method exploits mesh points. The accuracy and the speed of the simulation can be controlled depending on the configuration of a system, e.g., the number of particles and mesh nodes.

In order to obtain the mesh-defined properties, it is necessary to assign charges on the mesh nodes using the charge assignment schemes, such as NGP, CIC, and TSC. A typical example of the PM method is a self-consistent electrostatic simulation using Poisson's equation as explained in the previous chapter. As discussed earlier, Poisson's equation needs to be solved regularly for the mesh-defined electrostatic potential. Differentiation of the obtained potential and the interpolation procedure are required to calculate the electric field on the mesh nodes and at the particle positions, respectively.

One of the important roles of the PM method is to include the influence of external force. In any case, the boundary conditions need to be specified to solve the Poisson equation, which can be included with simple modification of matrix entries.

The general procedure of the PM method includes:

1. Assign charge to the mesh nodes (NGP, CIC, and TSC)
2. Solve Poisson's equation on the mesh
3. Compute electric field from the mesh-defined potential
4. Interpolate electric field at particle positions

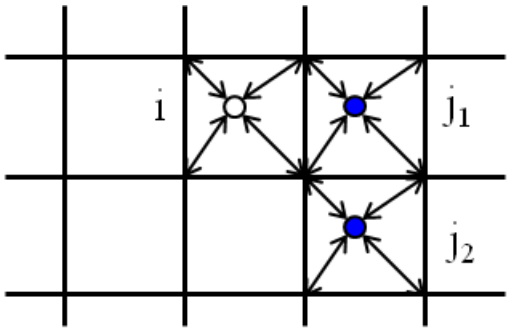

Figure 3.4: Illustration of the PM method using 2-D example for simplicity. The arrows are pointing charge assignment from charges to mesh nodes and electric field interpolation from mesh nodes to the positions of charges. Both schemes should be consistent to avoid a serious self-force problem. The CIC method is illustrated in this figure. In the case of NGP, only the shortest arrow will be used for the charge assignment and electric field interpolation.

In the procedure, CPU time for steps 1 and 4 depends on the number of particles. On the other hand, CPU time for steps 2 and 3 is determined by the number of meshes. Since steps 2 and 3 occupy most of the CPU time for the entire procedure, enormous speed gain is expected for many particle systems with reduced number of meshes. The limitation of the method is that the speed gain is obtained at the cost of resolution in the potential and the electric field in short range. Therefore, the pair forces between the charge particles are poorly represented when they are closer than one or two mesh spacings [12, 49].

3.2.3 Original P^3M method

The P^3M method is a hybrid of the PP and the PM methods as shown in Fig. 3.5. The PP method is used for accuracy in short range and the PM method is used for efficiency in long range. In this way, accurate short-range force calculation can be extended to a full device structure with small overhead, beyond the cost already involved with the Poisson equation.

Accordingly, the P^3M method can be applied to a much larger ensemble of particles without loss of accuracy and speed [49]. The P^3M method is a very popular technique for cosmological simulations, but has not been used widely for semiconductor device simulations

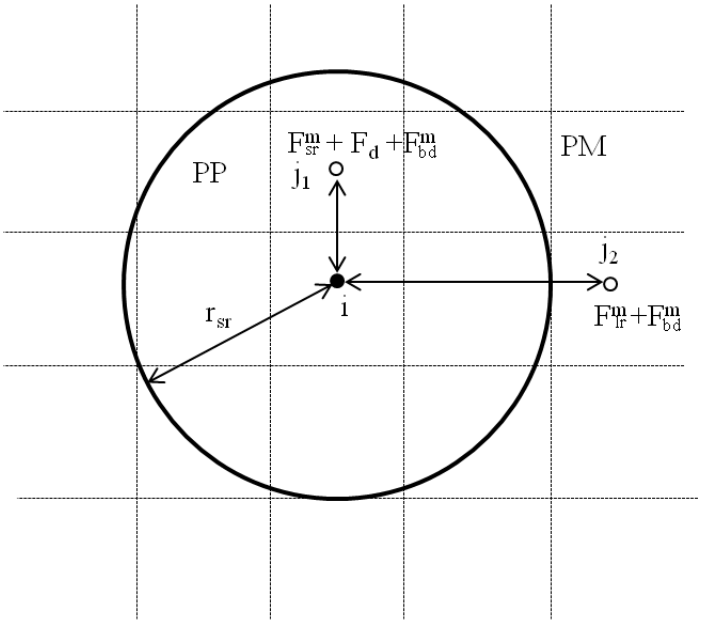

Figure 3.5: 2-D illustration of the P^{3}M approach. Long-range force can be calculated using the PM method and short-range force can be calculated by the PP method.

[52, 53].

Even though the concept of the P^{3}M method is simple and easy to understand, the developers of the method, Hockney and Eastwood, noticed that there was a practical problem for the short-range force calculation [49].

The PM and the PP force can be expressed as

$$F_{PM} = F^m_{lr} + F^m_{sr} + F^m_{bd} \tag{3.2}$$

$$F_{PP} = F_d \tag{3.3}$$

where F_{PM} is force from the PM method, which is the sum of the long-range mesh force F^m_{lr}, the short-range mesh force F^m_{sr}, and the forces by the boundary conditions F^m_{bd}. F_{PP} is force from the PP method, which represents the direct force F_d. From the configuration of the method, we can expect that there will be some overlap of the forces between short-range mesh force and the direct force. Accordingly, the local mesh force needs to be eliminated to

avoid double computation of pair forces inside the short range.

The components of the forces on particle i can be given by

$$\begin{aligned} F_i &= F_{PM} + F_{PP} - F_r && (3.4) \\ &= F_{lr}^m + F_{sr}^m + F_{bd}^m + F_d - F_r && (3.5) \\ &= F_{lr}^m + F_d + F_{bd}^m && (3.6) \end{aligned}$$

F_r is the so-called reference force introduced to account for the overlap of the simulation domain in short range, i.e., to eliminate the double computation of the pair force inside the short range.

Our goal is to make F_i the sum of F_{lr}^m, F_d, and F_{bd}^m. It can be achieved when F_r is the same as F_{sr}^m. By doing so, the short-range force between particles can be determined by accurate Coulomb's law, and we can still conserve the influence of long-range mesh force and external forces by boundary conditions.

The double-counting problem itself seems to be clear; however, it is extremely difficult to find the proper solution. Probably, we can think of several options for the reference force calculation. Based on the fact that the short-range local mesh force originates from Poisson's equation, we may solve Poisson's equation in short range to find the local mesh force. However, it poses difficulties in defining boundary conditions. Or we may solve Poisson's equation for the entire simulation domain to find the local mesh force. However, it will require too much computational resources and thus there will be no benefit of using the P^3M method.

Since there has been no known method to precisely reproduce F_{sr}^m, an approximate analytical model was suggested to obtain F_r as follows [12, 49]:

Hockney suggested several example shapes including the uniformly charged sphere, the sphere with uniformly decreasing density, and the gaussian distribution of density [49]. Among them the following $S(r)$, the second shape above, showed better accuracies.

$$S(r) = \begin{cases} \frac{48}{\pi r_{sr}^4}(r_{sr}/2 - r) & r \le r_{sr}/2 \\ 0 & r > r_{sr}/2 \end{cases} \tag{3.7}$$

$$F^r(r) = F^r(x) \cdot \hat{r} = \frac{\hat{r}}{4\pi\varepsilon} \int dx' \int dx'' S(x'') S(x' - x'') \frac{(x' - x'')}{|x' - x''|^3} \tag{3.8}$$

Based on the above equations, the reference force can be obtained by

$$F_{ij}^r(r) = \frac{q_i q_j}{4\pi\varepsilon} \times \begin{cases} \frac{1}{35r_{sr}^2}(224\xi - 224\xi^3 + 70\xi^4 + 48\xi^5 - 21\xi^6) & 0 \le r \le r_{sr}/2 \\ \frac{1}{35r_{sr}^2}(\frac{12}{\xi^2} - 224 + 896\xi - 840\xi^2 + 224\xi^3 & \\ \qquad +70\xi^4 - 48\xi^5 + 7\xi^6) & r_{sr}/2 \le r \le r_{sr} \\ \frac{1}{r^2} & r > r_{sr} \end{cases} \tag{3.9}$$

where

$$\xi = \frac{2r}{r_{sr}} \tag{3.10}$$

where r is the distance between particles, r_{sr} is the short-range radius. Considering the complexity of the PM calculations, however, the analytical solution is too simple, since it only involves the short-range radius r_{sr} and the distance between particles r.

In the original P^3M method, two different kinds of meshes are implemented. One is charge-potential mesh for the Poisson's solution and the other is chain mesh for the P^3M procedure. Typically, the chain mesh is a regular lattice with bigger size than the charge-potential mesh to improve the speed [49].

3.3 Modified P^{3}M Method Using Numerical Reference Force

In this study, we develop a new numerical approach to replace the analytical reference force by reverse engineering the PM method [11]. The general PM method consists of four steps as shown in the left branch in Fig. 3.6. Our numerical scheme, to reproduce local mesh force, follows a similar procedure with the main difference being in the governing equation in the second step.

The basic assumption of our approach is that the procedure based on Poisson's equation and Coulomb's law are equivalent. After assigning charges of primary particle i and partner particle j to the mesh nodes as in Fig. 3.7, we apply the PP method to evaluate the reference force of particle j on particle i, using

$$F_{ij}^{r} = \sum_{m \neq n} \frac{w_{i_n} w_{j_m} q_i q_j}{4\pi\varepsilon} \frac{(r_{i_n} - r_{j_m})}{|r_{i_n} - r_{j_m}|^3} \tag{3.11}$$

where q is the electric charge, ε is the dielectric constant, w is the fraction of charge, r is the position, and n and m are the node indices for the mesh nodes to which the charges of i and j are assigned, respectively. Note that this equation is also based on Coulomb's law as the direct force calculation (see equation (3.1)) in short range. However, the equation (3.11) is to obtain the reference force, which is originated from the mesh force of the Poisson's solution. Even though the number of calculations increases with the charge assignments and the force evaluations on the charge assigned mesh nodes, the influence on the CPU time is marginal since the number of calculations is limited by the short-range radius.

One of the notable properties of the reference force is that, in principle, it should not include external forces since it represents the local mesh forces induced only by charge distribution inside the short range. This implies that if we calculate the reference force using the PM approach, an additional technique is required to eliminate the influence of external force. However, the external force can be excluded automatically as we use Coulomb's law and the PP method for the evaluation of reference force.

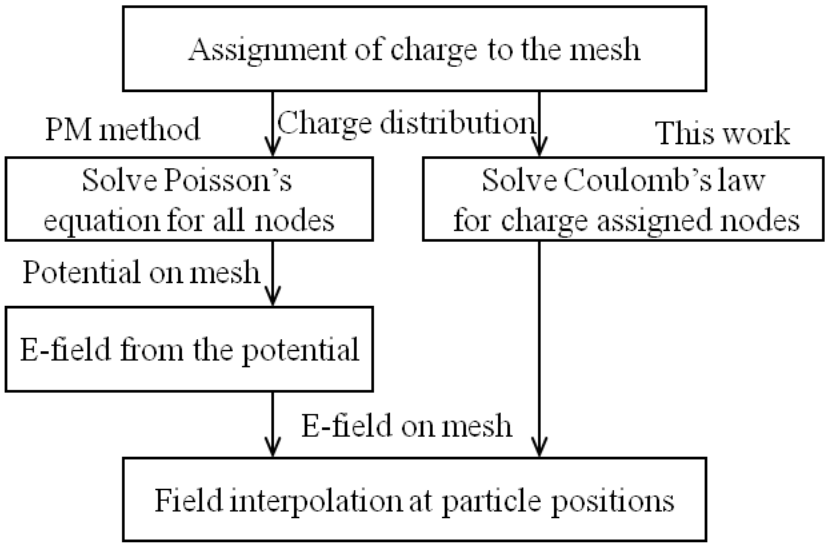

Figure 3.6: Flowchart of the PM method and this work to obtain the numerical reference force. Instead of solving Poisson's equation on all the mesh nodes, equivalent Coulomb's equation is solved only for the charge assigned mesh nodes.

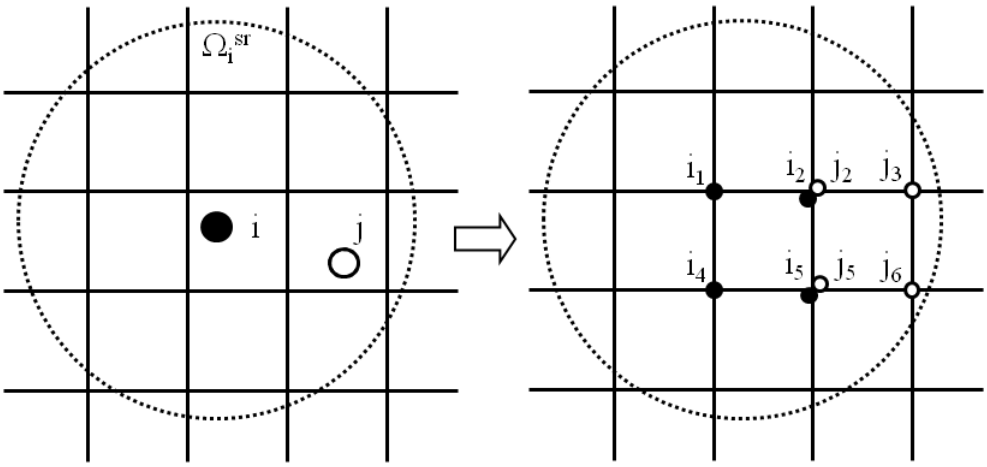

Figure 3.7: Charge assignments of the particles inside the short range (r_{sr}) using the cloud-in-cell (CIC) scheme. For the simplicity, a 2-D example is described and the fractional differences of assigned charge are not precisely illustrated here.

The proposed method is compared with the analytical reference force in Fig. 3.8. It shows that the proposed numerical method gives results similar to those of the existing analytical solution. The results imply that the numerical reference force scheme is promising and needs to be verified for more cases.

For the further evaluations, we extended our tests using more general conditions. At this point, we applied a 3-D Poisson's solver to make standard solutions for the reference force. As discussed earlier, the 3-D Poisson's solver cannot be used for the regular reference force calculations due to the enormous computational expenses. However, it can be used for the evaluation of simpler methods. The 3-D simulation domain was set to be wide enough to minimize the influence of the external forces, even though the influence cannot be eliminated completely. A charge particle is positioned in the middle of the simulation domain as shown

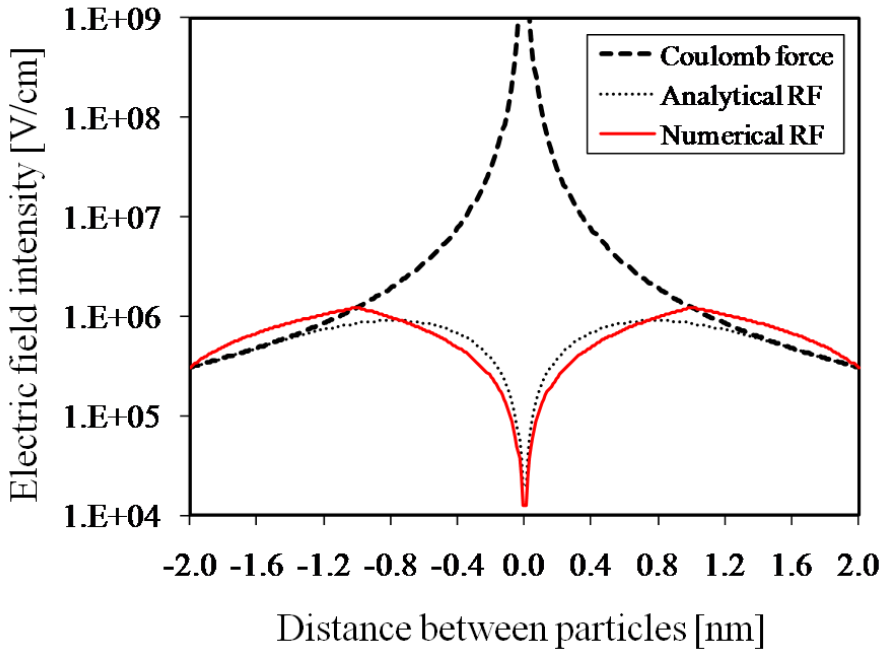

Figure 3.8: Reference forces (RF) and the direct Coulomb force are described. Analytical RF is based on the equation (3.9). CIC scheme is used and r_{sr} is set to 2 meshes (i.e. 2 nm). Uniform cubic mesh, 1×1×1 nm, is used. In this example, we assume that the location of the primary particle i is 0.0 and the position of the partner particle j is varied from -2.0 to 2.0 nm. (Note : Electric field=Force/q.)

in Fig. 3.9. The potential of all mesh nodes inside the simulation domain is obtained by solving the 3-D Poisson's equation as in Fig. 3.10. Based on the obtained potential, electric field is calculated using the second order central difference method. Figure 3.11 shows the resulting electric field of the mesh line on which the charge particle is located. In this example, electric field between the mesh nodes is interpolated by the CIC method.

We varied the short-range radius (r_{sr}) and charge assignment schemes. The short-range radius is varied from 1 to 3 mesh spacings. In the case of the charge assignment scheme, NGP and TSC are applied in addition to the CIC method, which is considered as a default scheme. The evaluation results in Figs. 3.12–3.16 show that the numerical reference forces match well with the solutions of the Poisson's solver for various conditions. This indicates that the numerical method can be more flexible in selecting the charge-assignment scheme and short-range radius.

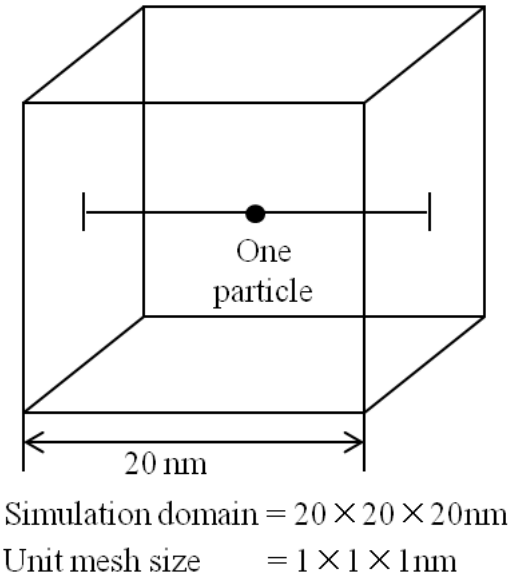

Figure 3.9: Evaluation by solving 3-D Poisson's equation. A charge is located in the middle of the simulation domain. Dirichlet condition is imposed for the boundaries.

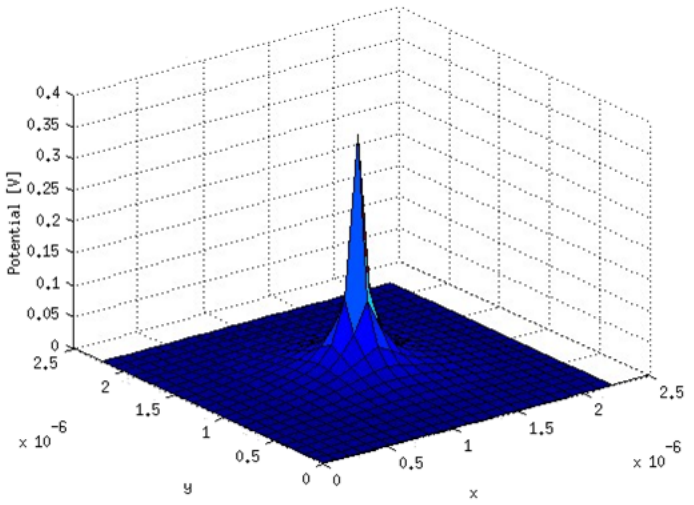

Figure 3.10: Potential profile of a plane on which a positive charge is placed.

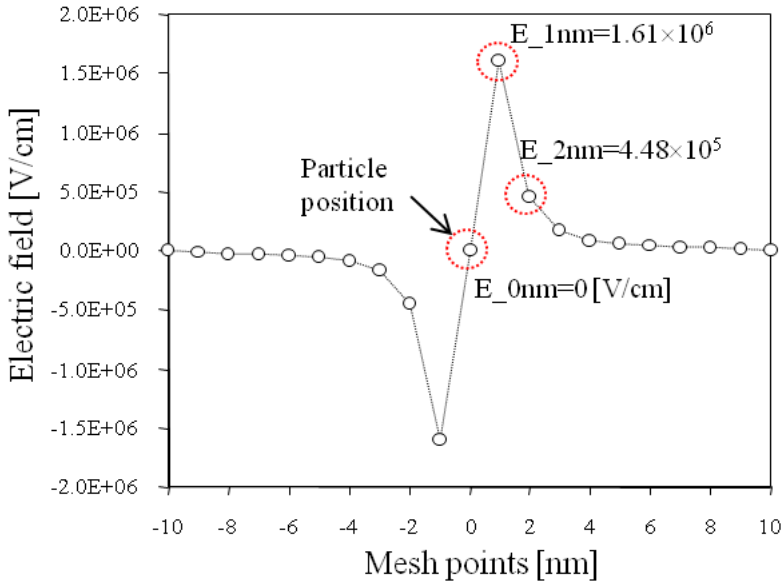

Figure 3.11: Electric field of the line on which a single charge is located. Electric fields of several mesh nodes are obtained and values in between are interpolated using CIC in this case. Note that the linear scale is used for the electric field.

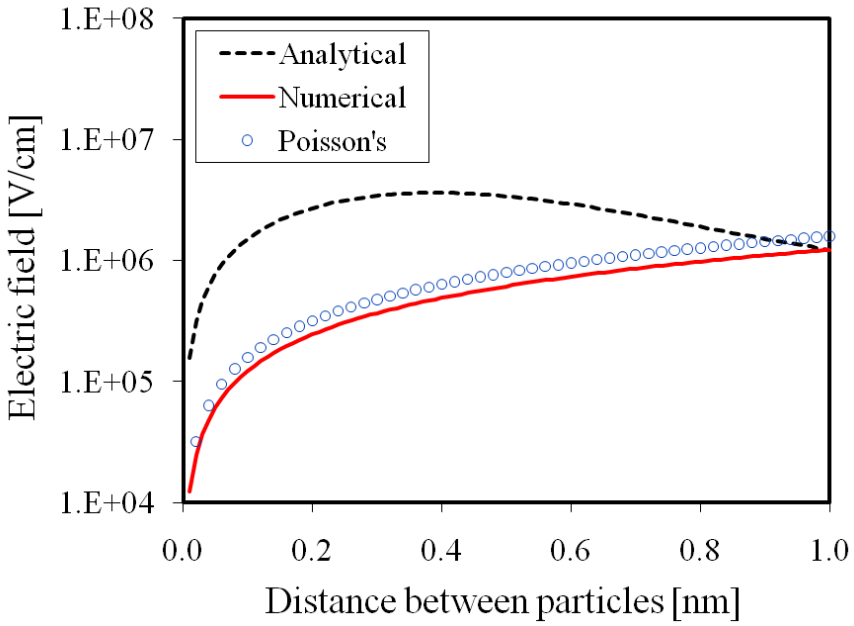

Figure 3.12: Comparison of the reference forces for r_{sr}=1 nm.

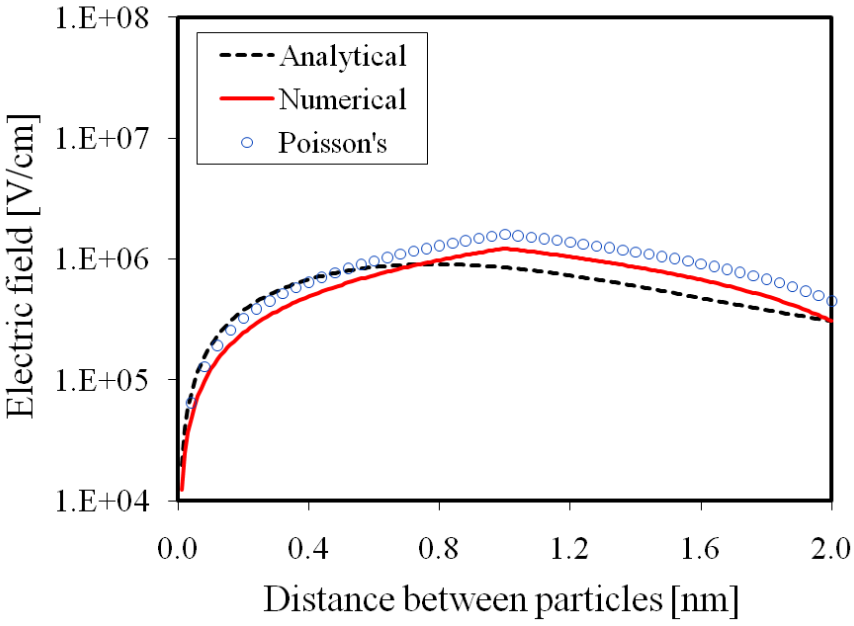

Figure 3.13: Comparison of the reference forces for r_{sr}=2 nm.

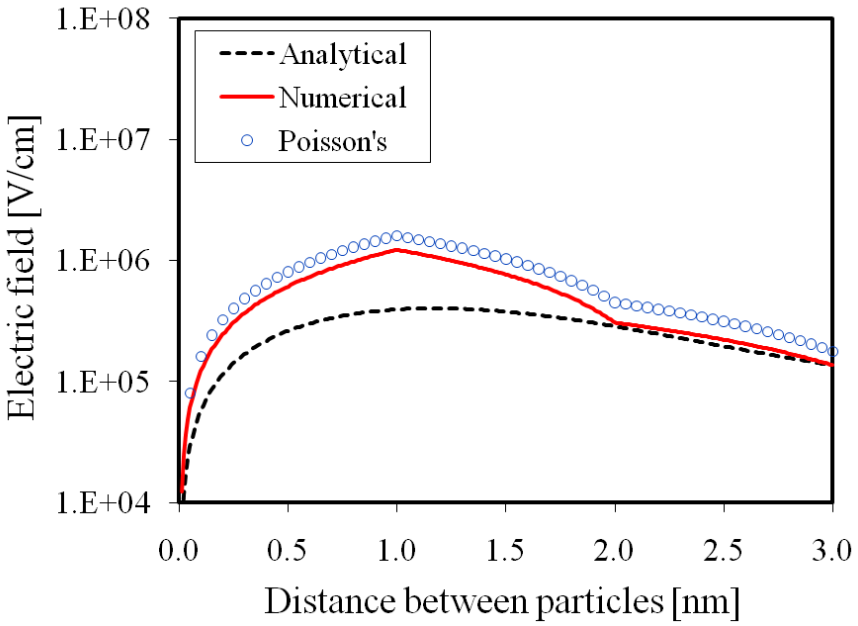

Figure 3.14: Comparison of the reference forces for r_{sr}=3 nm.

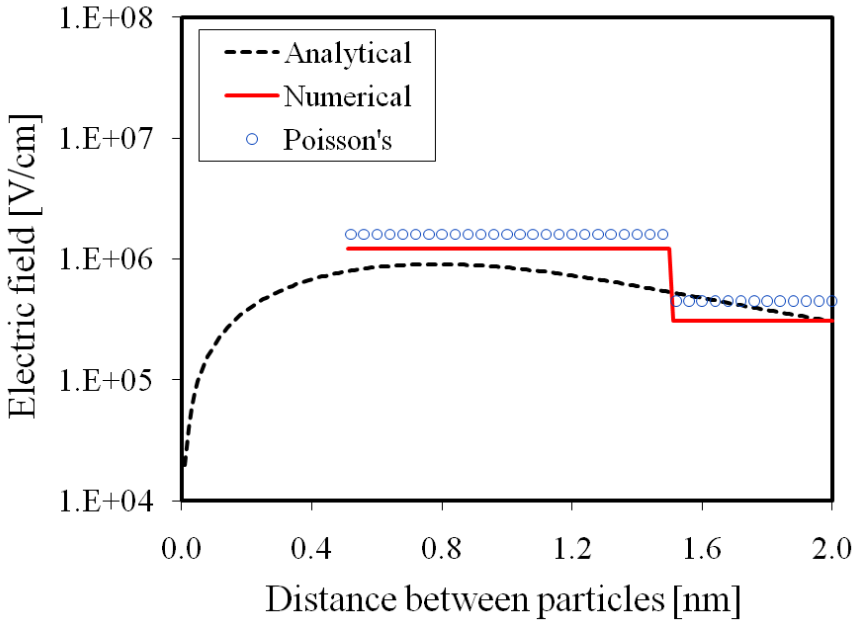

Figure 3.15: Comparison of the reference forces for NGP charge assignment scheme.

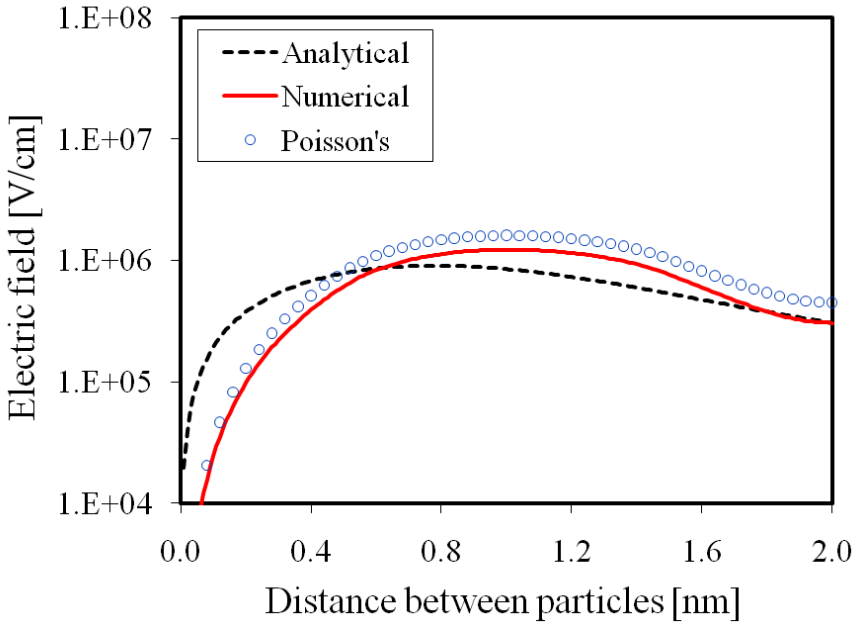

Figure 3.16: Comparison of the reference forces for TSC charge assignment scheme.

In order to apply to the device simulations, the applicability on non-uniform mesh has great importance. In device simulation, non-uniform mesh is very common to effectively utilize the limited computational resources while focusing on the region of interest.

We used a test case (see Fig. 3.17) to compare two approaches with the application of non-uniform mesh. The physical distances of $i - j_1$ and $i - j_2$ are the same. The difference lies in the mesh size for two cases as can be seen in the figure. In Fig. 3.18, the intensities of short-range electric field, which can be considered as a reference force, are compared. In the case of analytical reference force, two forces, i.e. $i - j_1$ and $i - j_2$, are the same since the distances between them are the same. However, in Poisson's solution and in numerical reference force, the force of $i - j_2$ is much lower than that of $i - j_1$. The step size of $i - j_2$ is twice and the assigned charge will be a half. Accordingly, the force of $i - j_2$ will be about 1/8 of the force of $i - j_1$ considering Coulomb's law. The process will be the same for Poisson's solution and numerical reference force except for the governing equation and truncation error for the PM method. Therefore, they show good agreement as can be seen in the graph.

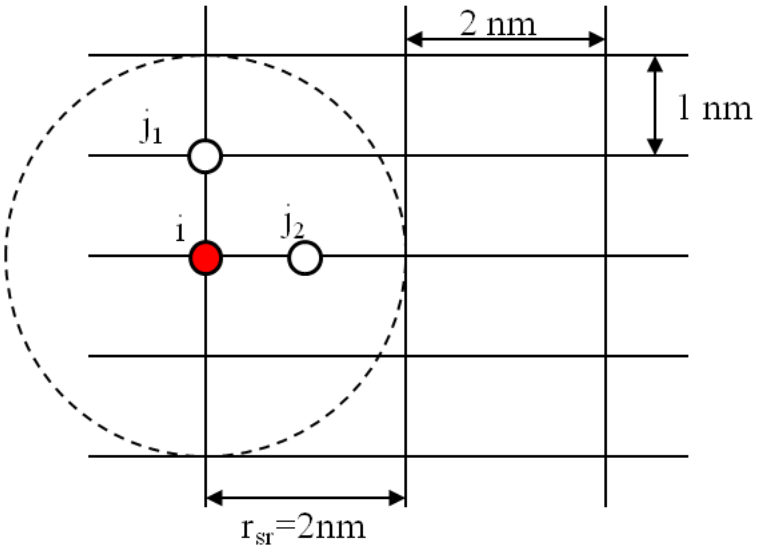

Figure 3.17: A test case for the evaluation on the non-uniform mesh. CIC method is assumed for the charge assignment. The particles are considered on a plane for the simplicity.

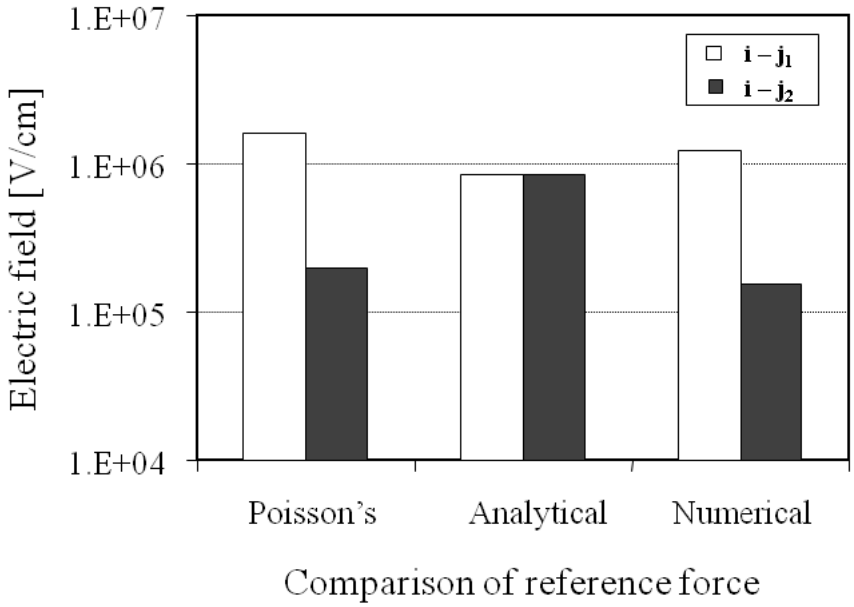

Figure 3.18: Electric field intensity of different approaches for short-range inter-particle forces.

After the evaluation with a simple structure, we applied the method for more general examples. The evaluations on non-uniform mesh (see Figs. 3.19 and 3.20) clearly show the improvement of accuracy in numerical approach. The results are natural because the numerical method is designed to follow a procedure similar to that of the PM as much as possible.

The analytical solution also yields reasonable results when the short-range radius corresponds to 2 mesh space with uniform cubic mesh as in Fig. 3.8. However, it shows large errors in general cases especially with the application of non-uniform mesh. We may use the different analytical expressions for different short-range radius or charge assignment scheme. However, it would be impossible to come up with an analytical expression that can be used for general non-uniform mesh.

Presumably, this is one of the reasons why the original P^3M method should have a regular lattice chain mesh, which is different from the charge-potential mesh. In our approach, on the other hand, the charge-potential mesh can be used directly to evaluate the reference force. In doing so, we can maintain the consistency with the source of the reference force, and the complexity of the method can be lowered as well. Therefore, the difficulties with the implementation of the method in device simulation can be reduced.

In summary, the uncertainty of the original P^3M method has been successfully eliminated with the application of numerical reference force approach. The application area of the P^3M method can be expanded as it can be applied in various conditions.

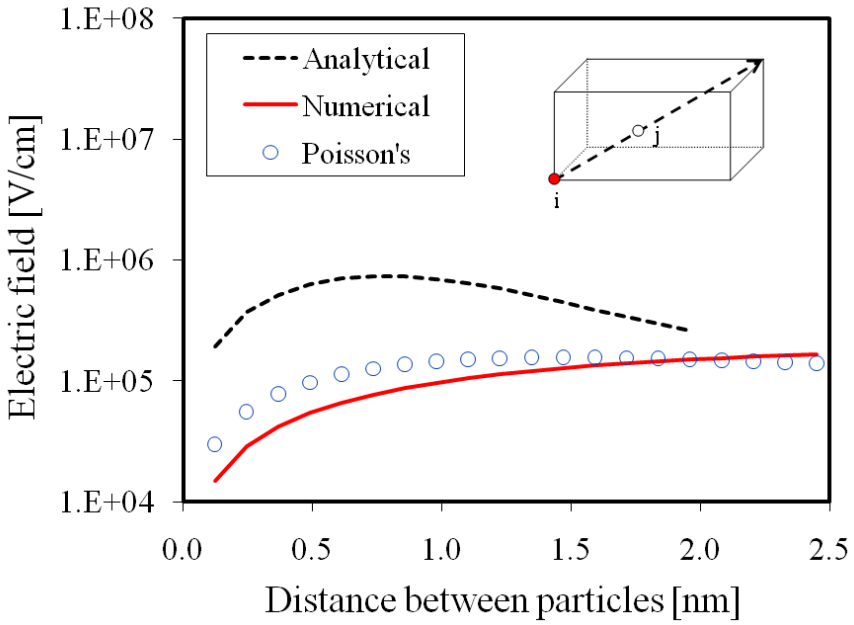

Figure 3.19: Evaluation on the non-uniform mesh, 2×1×1 nm, application. Particle i is at the mesh node and j is moved along the diagonal direction.

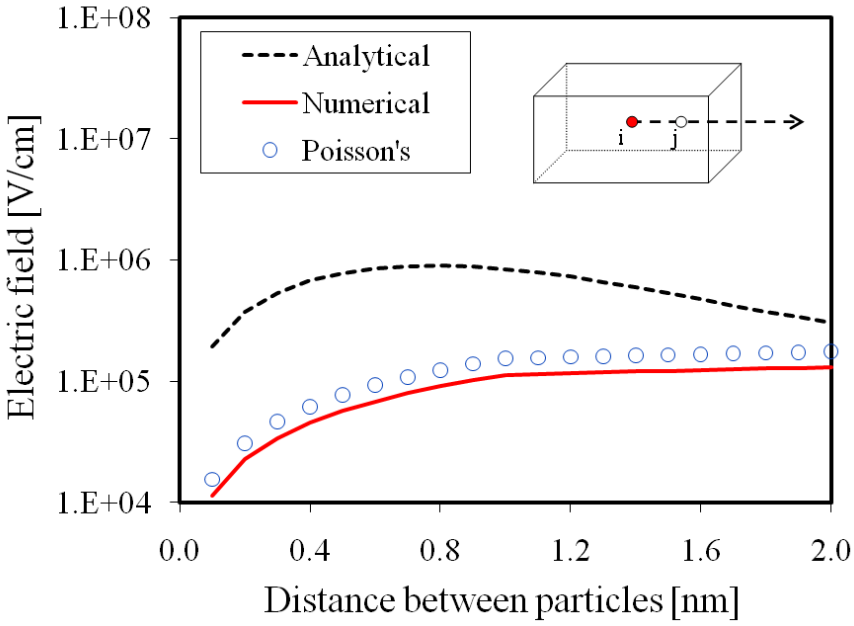

Figure 3.20: Evaluation on the non-uniform mesh, 2×1×1 nm, application. Particle i is at the center of the mesh cell and j is moved along the center line.

3.4 Improvement of Accuracy in the Numerical Reference Force Calculation

As explained above, we calculate the numerical reference force using Coulomb's law and the PP method, which is known as the most accurate method to calculate forces between point charges. In principle, however, the reference force represents the local mesh force based on Poisson's solution, which has inherent errors including truncation errors by finite difference method to solve the differential equation. Accordingly, a certain level of disagreement is inevitable between the local mesh force and the numerical reference force.

To some extent, we may exploit the properties of error from the PM method to minimize the discrepancy between numerical reference force and the local mesh force. Note that the finite difference method is used both for the potential calculation using Poisson's equation and for the following electric field calculation.

In order to explain the properties of the PM method and its errors, we show potential and corresponding electric field for various mesh spacings in Fig. 3.21. For the test, cubic mesh is used with node spacings of 0.5 nm, 1.0 nm, and 2.0 nm, respectively. As we increase the mesh spacing, the potential at the point of a positive charge goes down, and this is also true for the electric field at the next mesh node. In Tables 3.1, 3.2, and 3.3, electric field intensities are compared between Poisson's approach and Coulomb's approach. As we can expect, the absolute errors of the Poisson's approach for the same physical length can be reduced by finer mesh. On the other hand, the relative errors, i.e. the ratio of the electric field between Poisson's and Coulomb's, remains the same for the same mesh steps. This indicates that we may use these values as fitting parameters to eliminate the discrepancy between Poisson's solution and the numerical reference force.

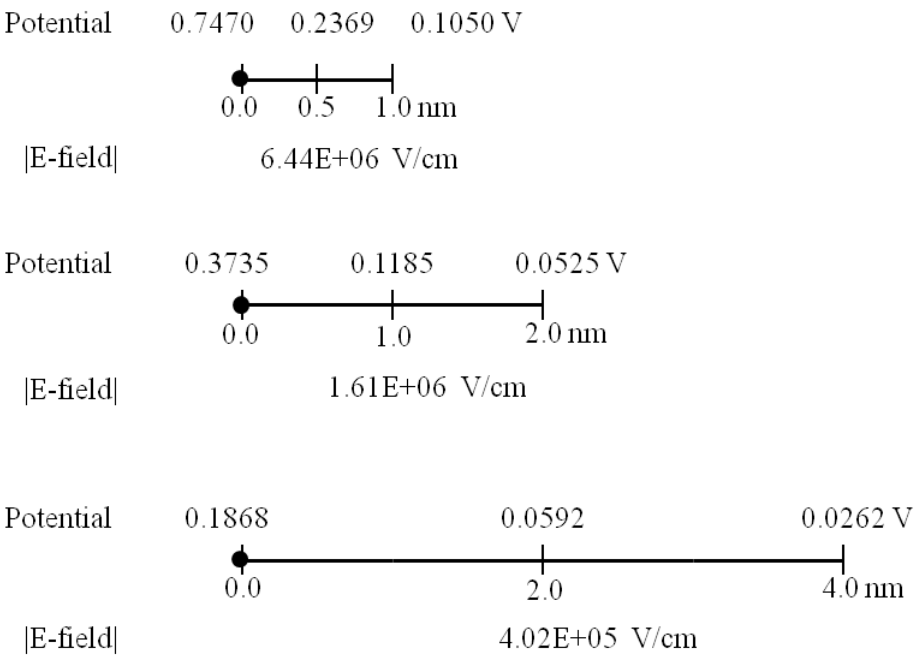

Figure 3.21: Potentials and corresponding electric fields with the variations of mesh spacing. We assume that a positive charge is located at 0.0 nm for each case. Potential and corresponding absolute value of electric field decrease as we increase the spacing.

Table 3.1: Electric field as a function of distance. Mesh spacing is 0.5 nm.

0.5 nm	0.5 nm	1.0 nm	1.5 nm
Poisson	6.44E+06	1.80E+06	7.06E+05
Coulomb	4.90E+06	1.23E+06	5.45E+05
Factor	1.3127	1.4707	1.2961

Table 3.2: Electric field as a function of distance. Mesh spacing is 1.0 nm.

1.0 nm	1.0 nm	2.0 nm	3.0 nm
Poisson	1.61E+06	4.51E+05	1.77E+05
Coulomb	1.23E+06	3.06E+06	1.36E+05
Factor	1.3127	1.4707	1.2961

Table 3.3: Electric field as a function of distance. Mesh spacing is 2.0 nm.

2.0 nm	2.0 nm	4.0 nm	6.0 nm
Poisson	4.02E+05	1.13E+05	4.41E+04
Coulomb	3.06E+05	7.66E+04	3.40E+04
Factor	1.3127	1.4707	1.2961

Figure 3.22 shows the square of the distances from the origin to the neighboring mesh nodes. Number of points can be limited by assigned short-range radius (r_{sr}). In this example, 2 mesh spacing is used for r_{sr}.

The fitting parameters, which represent the ratio between the PM and the PP method, are shown in Table 3.4. The parameters are applied to test cases with cubic mesh as shown in Fig. 3.23.

In Figs. 3.24, 3.25, and 3.26, the results with the obtained fitting parameters are presented. The results show that the numerical reference forces with fitting parameters perfectly match with those of Poisson's solutions.

In Figs. 3.27, 3.28, and 3.29, we also confirm that the same fitting parameters can be used for any cubic mesh with different mesh spacing.

Furthermore, the same procedure can be used even for the non-cubic mesh. Figure 3.30 shows the square of the distances from the origin to the neighboring mesh nodes in non-cubic

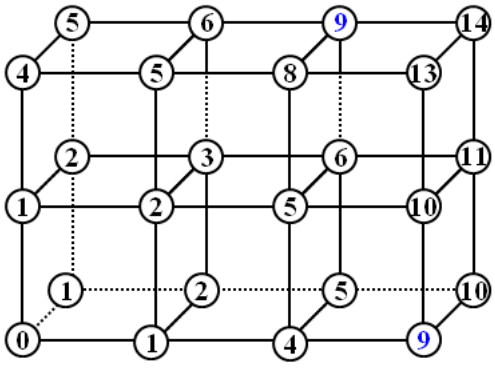

Figure 3.22: Cubic mesh nodes and square of the distance from the origin.

Table 3.4: Fitting parameters for cubic mesh based on the discrepancies.

Distance^2	x	y	z	Factor
1	1	0	0	1.3185
2	1	1	0	0.8909
3	1	1	1	0.7583
4	2	0	0	1.4709
5	2	1	0	1.0422
6	2	1	1	0.9026
8	2	2	0	0.9849
9	2	2	1	0.9164
9	3	0	0	1.2793
10	3	1	0	1.0880
11	3	1	1	1.0018
12	2	2	2	0.9148
13	3	2	0	1.0034

mesh application. As in the previous case, number of points can be limited by r_{sr}, which is the same as the cubic mesh. The fitting parameters for non-cubic mesh ($2 \times 1 \times 1$) are shown in Table 3.5.

Figure 3.31 shows the structures with non-cubic meshes, and the corresponding results are shown in Figs. 3.32, 3.33, and 3.34. The only practical problem of the method is that the fitting parameters need to be pre-calculated for the corresponding mesh configurations. However, remarkable improvement on the elimination of the local mesh force has been made considering the limitation of the original P^{3}M method.

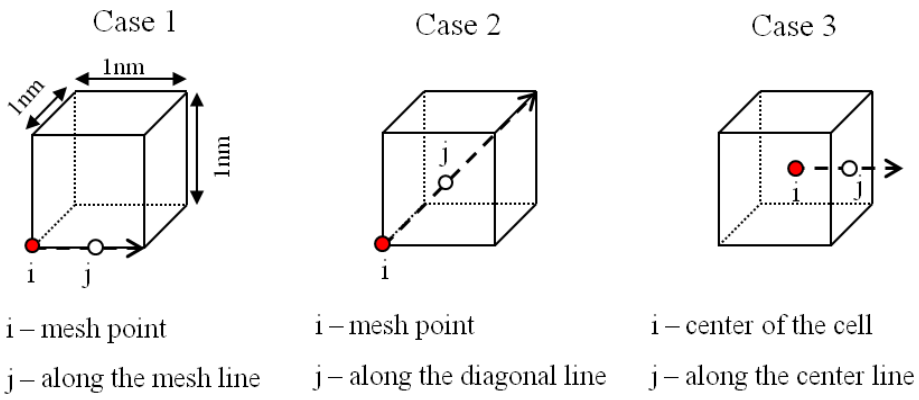

Figure 3.23: Test cases for the cubic mesh.

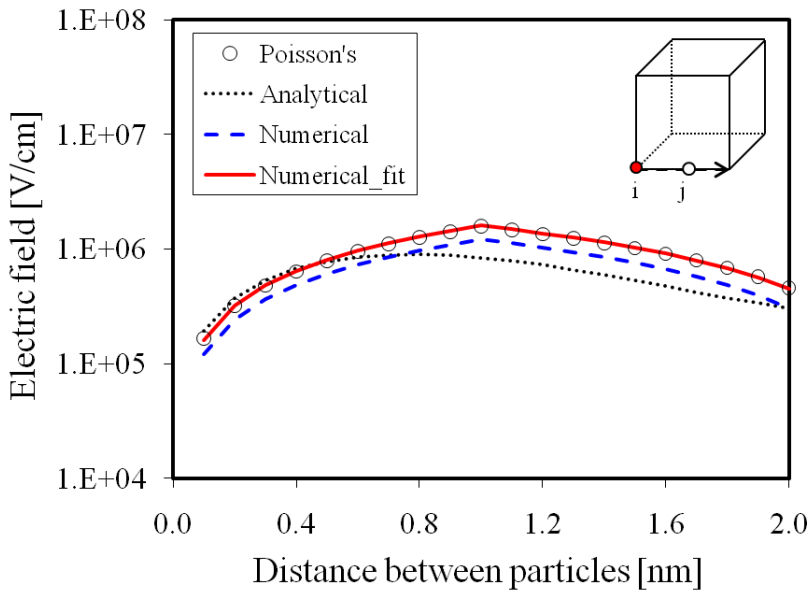

Figure 3.24: Comparison of the reference forces for case 1. Cubic mesh with 1 nm spacing.

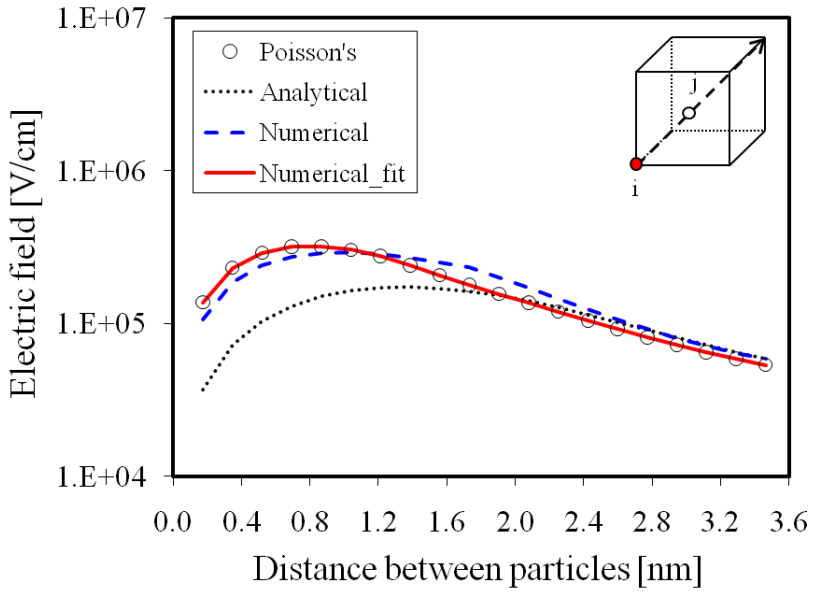

Figure 3.25: Comparison of the reference forces for case 2. Cubic mesh with 1 nm spacing.

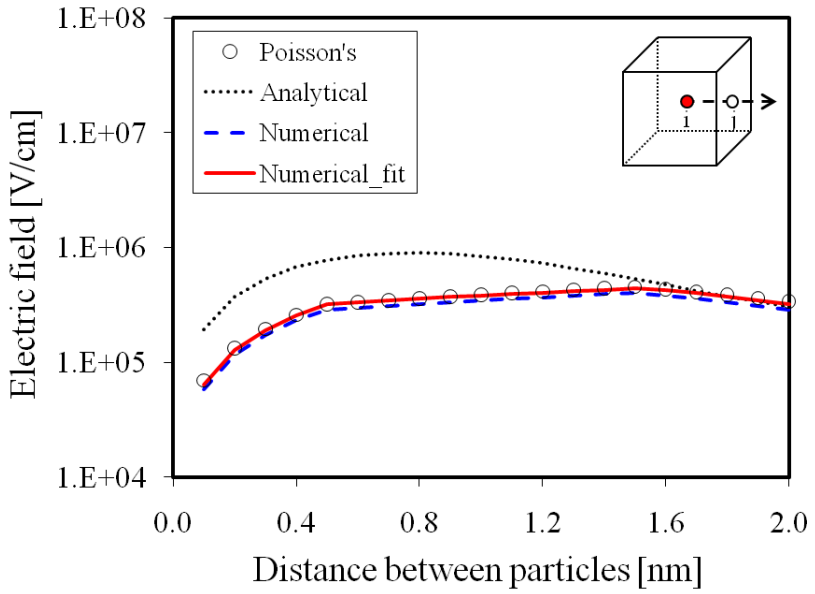

Figure 3.26: Comparison of the reference forces for case 3. Cubic mesh with 1 nm spacing.

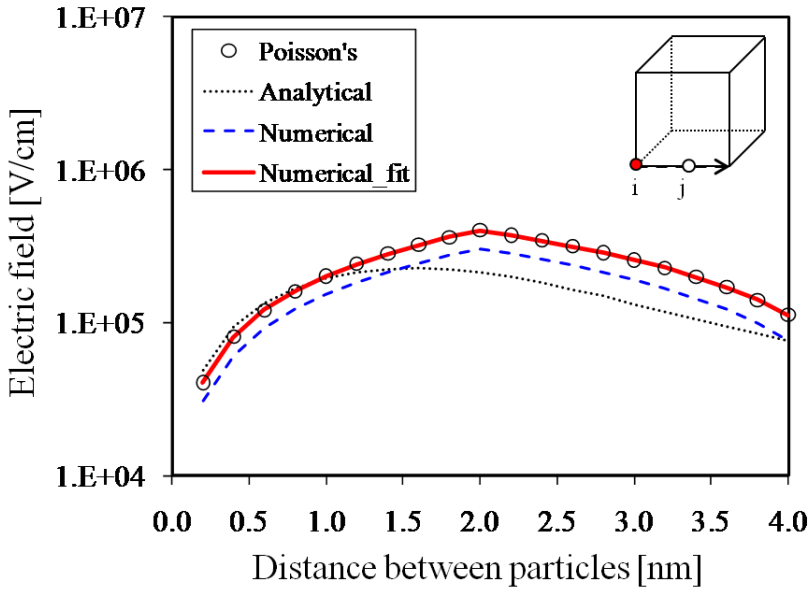

Figure 3.27: Comparison of the reference forces for case 1. Cubic mesh with 2 nm spacing.

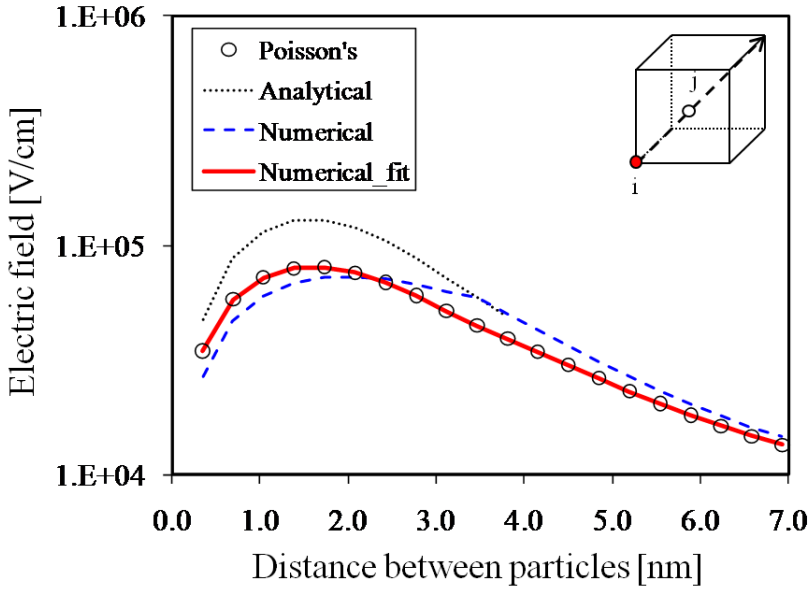

Figure 3.28: Comparison of the reference forces for case 2. Cubic mesh with 2 nm spacing.

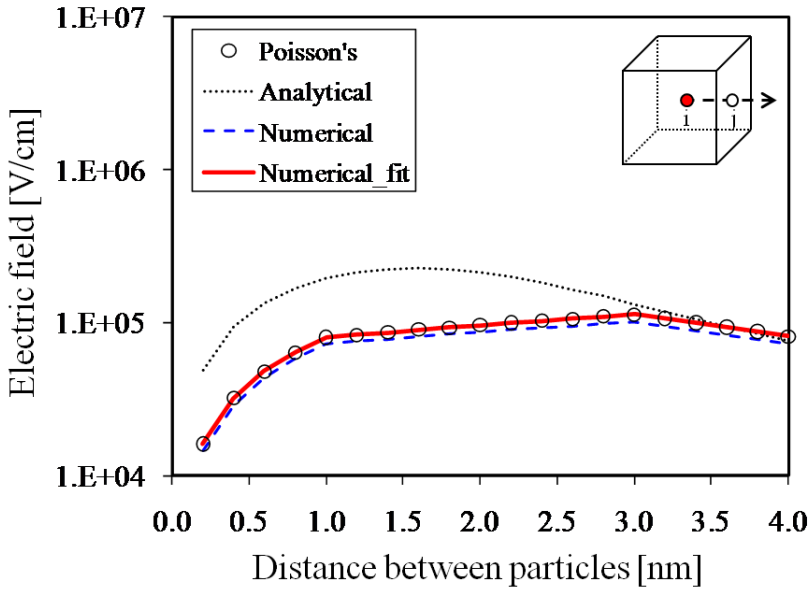

Figure 3.29: Comparison of the reference forces for case 3. Cubic mesh with 2 nm spacing.

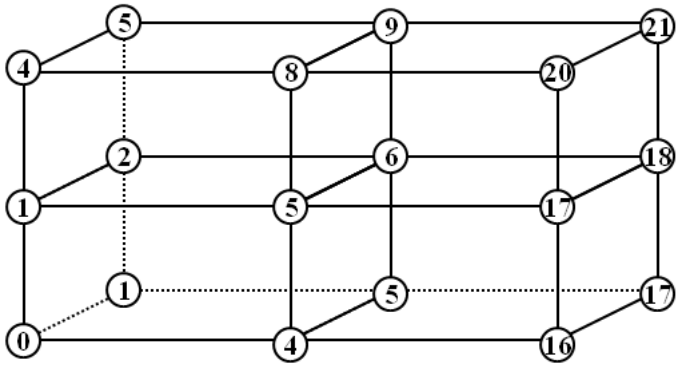

Figure 3.30: Non-cubic mesh nodes and square of the distance from the origin.

Table 3.5: Fitting parameters for non-cubic mesh, (2×1×1), based on the discrepancies.

Distance^2	x	y	z	Factor
1	0	1	0	1.3185
2	0	1	1	0.8909
4	0	2	0	1.4709
4	2	0	0	2.0667
5	0	2	1	1.0422
5	2	1	0	1.0272
6	2	1	1	0.8082
8	2	2	0	0.8650
16	4	0	0	1.3203
17	4	1	0	1.0428
18	4	1	1	0.9248

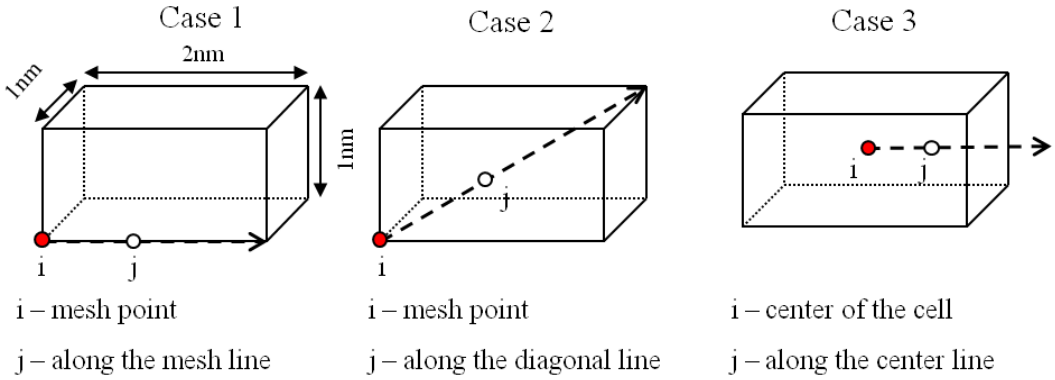

Figure 3.31: Test cases for the non-cubic mesh.

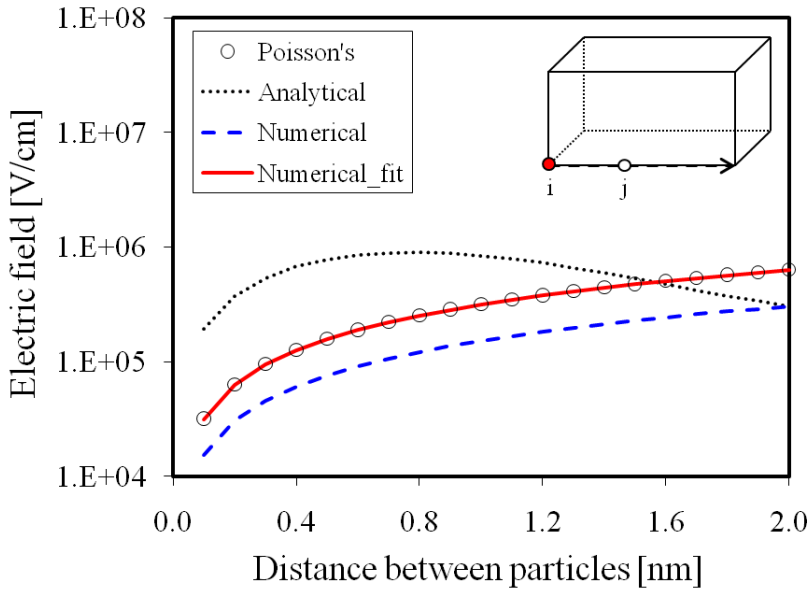

Figure 3.32: Comparison of the reference forces for case 1. Mesh size with 2×1×1 nm.

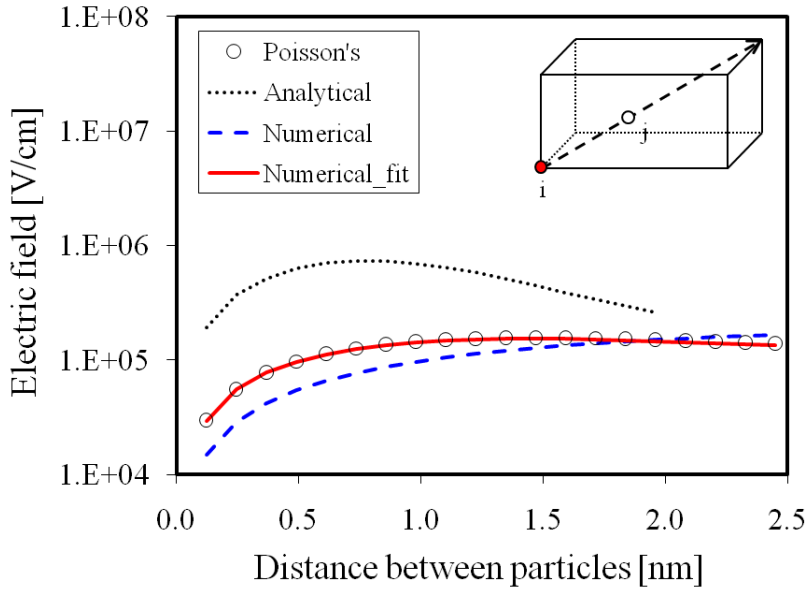

Figure 3.33: Comparison of the reference forces for case 2. Mesh size with 2×1×1 nm.

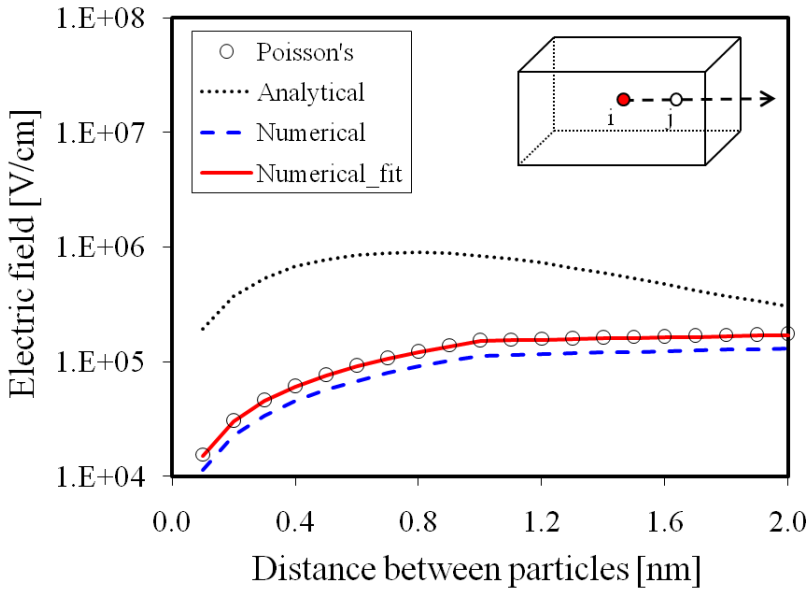

Figure 3.34: Comparison of the reference forces for case 3. Mesh size with 2×1×1 nm.

3.5 Conclusion

In this chapter, the properties of Coulomb scattering are described and the most popular approach to treat the scattering, i.e. Fermi's golden rule based scattering rate method, are discussed. The issues associated with the approach are presented for carrier-carrier and carrier-impurity scattering.

The properties of an alternative method, P^3M, are discussed based on the two basis methods, the PP method and the PM method. The practical problem of the original P^3M method is the uncertainty of analytical reference force, which needs to be introduced to avoid the double computation of pair force inside the short range. In this chapter, the analytical reference force is replaced by a novel numerical approach. Basically, we apply Coulomb's law instead of Poisson's equation at the mesh points on which charge particles are assigned. The efficiency of the method is verified with various examples, which confirms that the proposed method can be applied to more general cases.

Accuracy of the numerical method can be made even better by applying fitting parameters. The fitting parameters can be pre-calculated depending on the mesh configuration. By understanding and taking advantage of the source of the errors in the PM method, we can obtain the fitting parameters, which can eliminate the errors of the reference force calculation significantly.

CHAPTER 4

ANALYSIS OF COULOMB SCATTERING USING MODIFIED P^{3}M-EMC SIMULATOR

In the previous chapter, we developed the P^{3}M method based on the numerical reference force calculation. In this chapter, we implemented the method on a 3-D ensemble Monte Carlo (EMC) simulator, MOCA3D. Using the simulator, carrier-carrier scattering and carrier-impurity scattering are evaluated for various cases.

4.1 Evaluation of the Modified P^{3}M-EMC Simulation

A surround-gate-transistor (SGT) with 60 nm length, 20 nm body thickness, and 1 V supply voltage as shown in Fig. 4.1 is used for the analysis of P^{3}M-EMC simulation. In this section, the properties of the PM and P^{3}M methods are compared and discussed based on the analysis of carrier-carrier scattering. It is important to note that, in this section, the carrier-impurity scattering is treated by conventional scattering rate method for both of the cases to simplify the problem.

The device simulation results of P^{3}M-EMC are compared with those of the PM-EMC method, which is important because the scattering rate approach, an alternative to consider carrier-carrier scattering, is based on the PM method. Accordingly, the strengths and weaknesses of the PM method directly influence the scattering rate approach. In carrier-carrier scattering, it is well known that the total energy of the carriers should be conserved during the interaction as explained in the previous chapter. In the previous chapter, however, we observed that the PM force approaches zero as the distance between two particles gets smaller than the mesh spacing, even though the actual force should be extremely high as can be seen in Fig. 3.8. This implies that the energy of the carriers may decrease during the

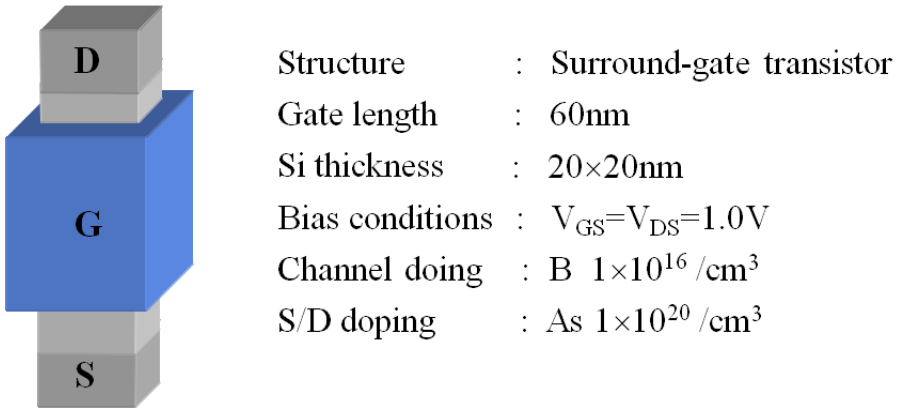

Figure 4.1: Surround-gate transistor is used for the evaluation of the P^{3}M-EMC simulator.

carrier-carrier interactions if the meshes in between are not fine enough. We can estimate the PM forces as a function of mesh size using the test meshes as in Fig. 4.2. In the test, the distance between the particles is fixed to 2 nm, but the mesh size is varied for each case. The results show that with the sparse mesh as in Fig. 4.2 (c), only 14% of the actual pair force can be captured. This implies that the energy will decrease when we use sparse mesh for the Poisson's equation. However, the loss of energy will not be recovered by the scattering rate method, in which the total energy after the scattering will be the same. Accordingly, when electrostatics by Poisson's solution is combined with the scattering rate method, the energy will be reduced by short-range interactions, which is a function of mesh size. After the confirmation of our assumption using the test, we performed P^{3}M-EMC device simulation with various mesh sizes. Figure 4.3 (a) and (b) compare the distribution function of the PM-EMC and the P^{3}M-EMC methods inside the channel region. From the distribution functions, we can estimate that the number of carriers with high energy decreases as we increase the size of the mesh in PM-EMC. On the other hand, in P^{3}M-EMC, the variation is reduced significantly. The corresponding average energy of the carriers and on-currents of the SGT are described in Fig. 4.4. The figure clearly shows the dependency of energy on mesh size in PM-EMC. In this graph, we also notice that the on-current is inversely proportional to average energy of the carriers. This can be explained by Figs. 4.5 and 4.6.

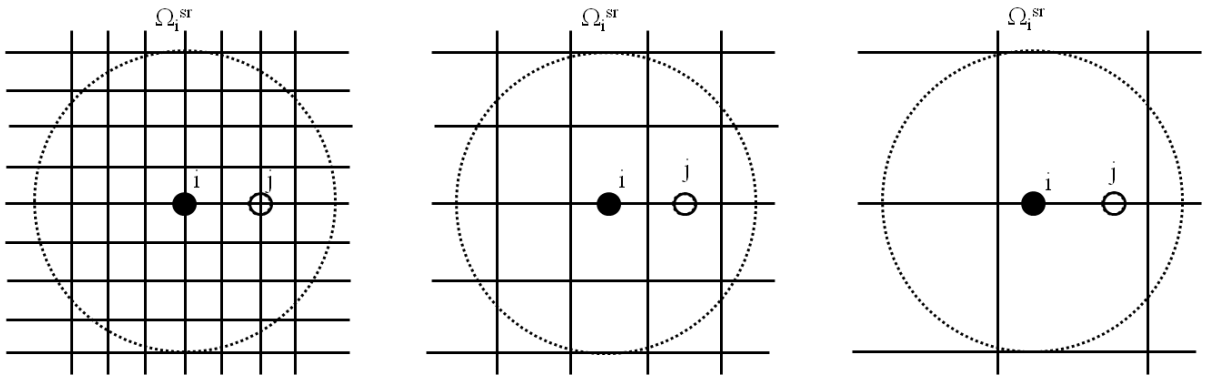

(a) Mesh space=1nm (b) Mesh space=2nm (c) Mesh space=4nm

Figure 4.2: Test meshes to evaluate the PM forces between particles as a function of mesh size. The distance between two particles is fixed to 2 nm for all cases. The PM forces between particles strongly depend on the mesh size. For instance, the forces between i and j show (a) 100%, (b) 56.3%, and (c) 14.0% of the actual forces. Note that the truncation error in the PM solution is ignored throughout the test.

In Fig. 4.5, most of the scattering rates are lower in PM-EMC. Figure 4.6 shows scattering rates along the direction of current flow, which shows that the optical emission is lower in PM-EMC. Even though the ionized impurity scattering is higher in PM-EMC, the influence is limited since the channel is relatively long and most of the impurity scatterings occur inside the source and drain regions.

In summary, when we increase the mesh size in PM-EMC, the energy will be lowered and most of the scattering rates will be lowered. This explains the reason for the increase of on-current for sparse mesh application. Unlike PM-EMC, the average energy and on-current of P^3M-EMC are conserved for a wide range of mesh sizes. Figure 4.4 also indicates that PM-EMC can be as accurate as P^3M-EMC if very fine mesh size is applied. However, it is computationally expensive as shown in Fig. 4.7. Comparison of simulation time between PM-EMC and P^3M-EMC with the same mesh size also shows that, despite extra calculations for the P^3M method, the increase of simulation time is marginal. Considering the results in Figs. 4.4 and 4.7, we can estimate that the computational time can be reduced by 80$\sim$90% by using the proposed P^3M-EMC without sacrificing accuracy.

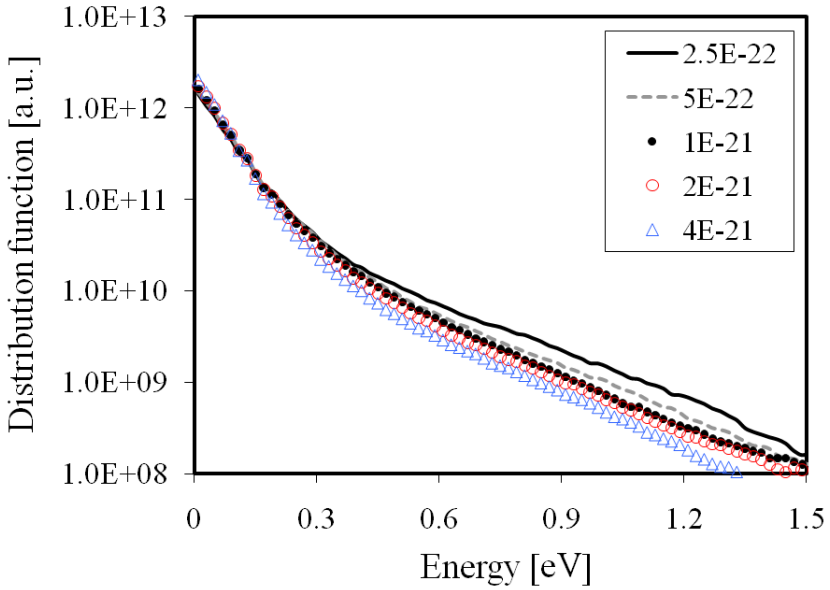

(a)

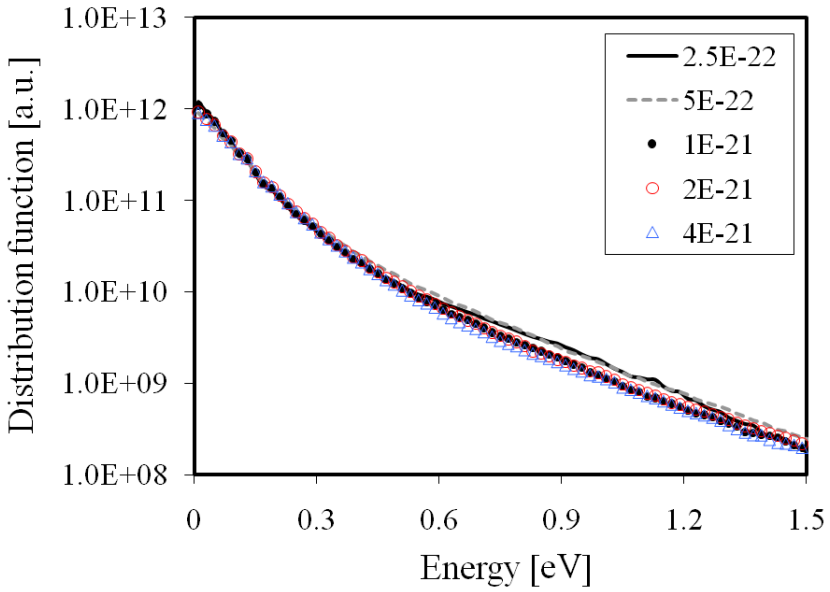

(b)

Figure 4.3: Distribution functions in the channel region for (a) PM-EMC and (b) P^3M-EMC with various mesh sizes [cm^3]. Considerable variations are observed for the PM-EMC method. Distribution functions for P^3M-EMC also show some variations, but the improvement is evident.

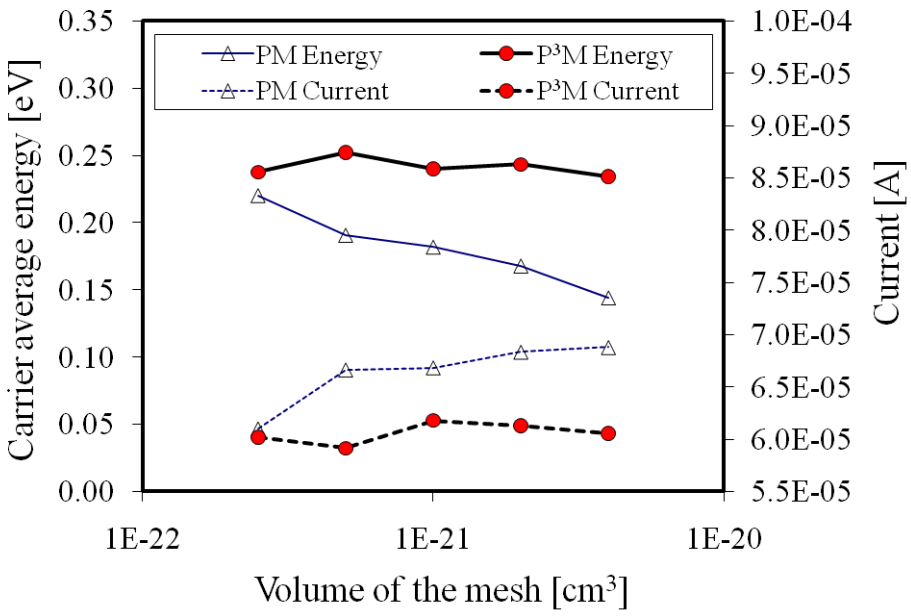

Figure 4.4: Average energy of the carriers and the corresponding on-currents of the SGT. Decrease of average energy in PM-EMC reduces the scattering rates, e.g., optical phonon scattering, which leads to the increase of on-current.

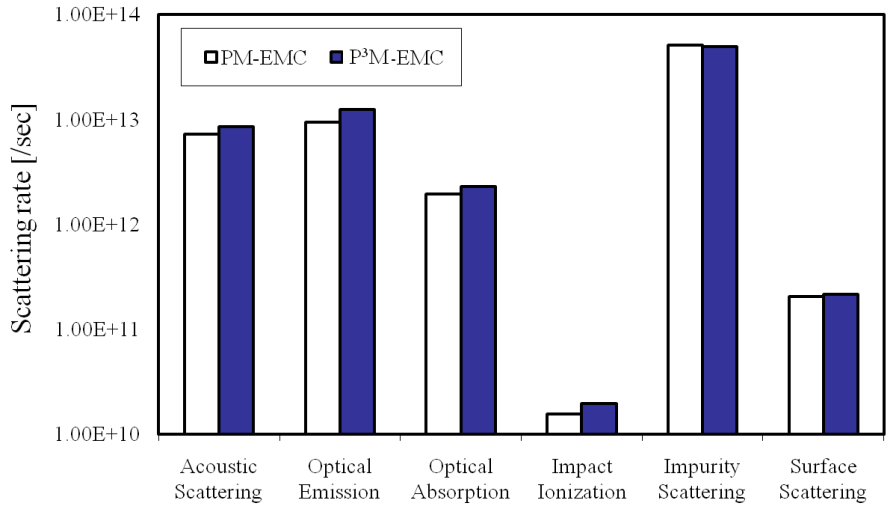

Figure 4.5: Comparison of the scattering rates between PM-EMC and P^{3}M-EMC. The volume of the mesh is set to 1×10^{-21} cm^3. All scattering rates except impurity scattering are lower in PM-EMC. This explains the increase of current in sparse mesh applications.

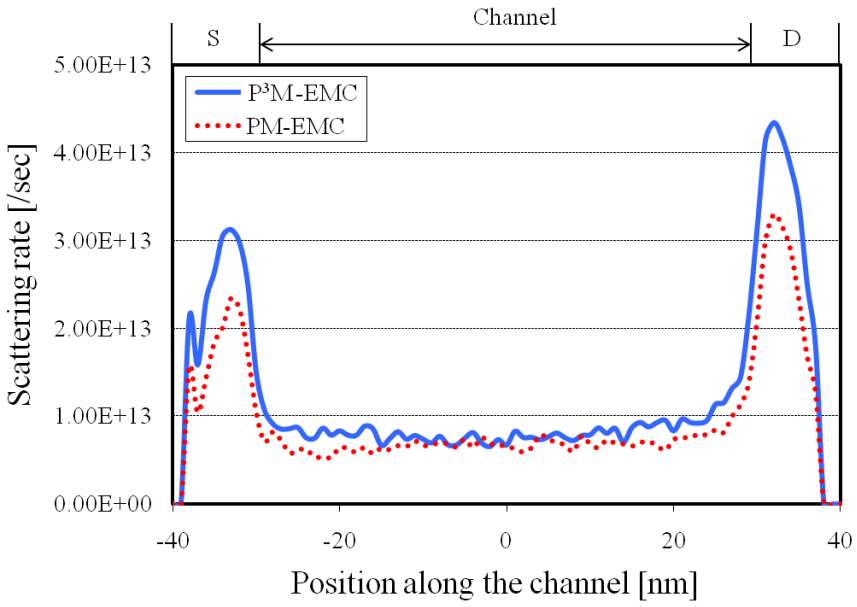

(a)

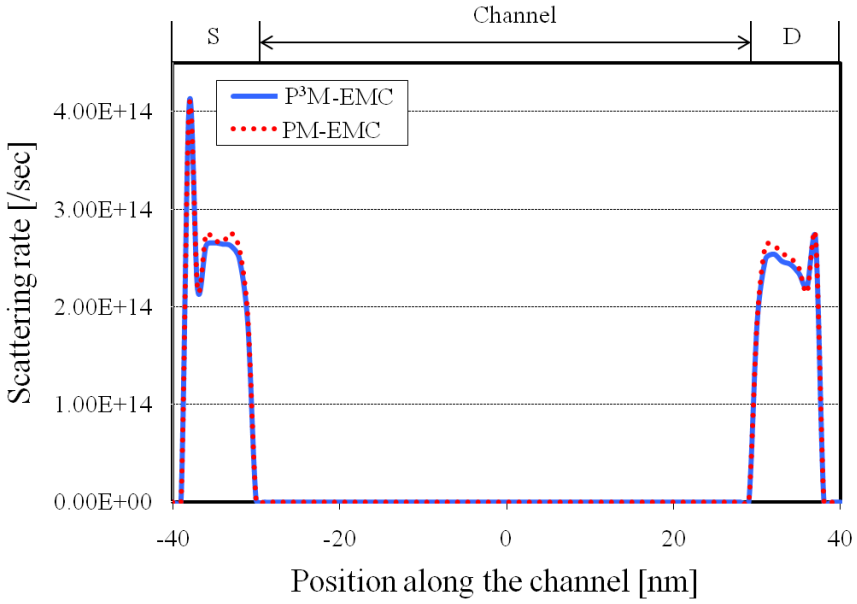

(b)

Figure 4.6: Scattering rates along the channel direction for (a) optical emission and (b) ionized impurity scattering based on Ridley model. Unlike the case of the optical emission, impurity scattering occurs mostly inside contact region.

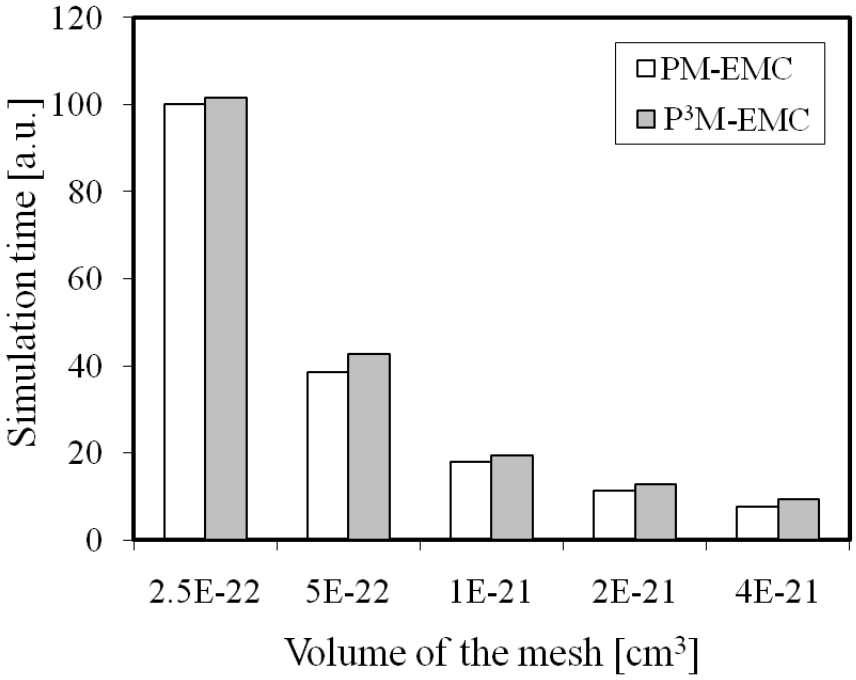

Figure 4.7: Simulation time as a function of mesh size [cm^3]. The simulation time can be reduced significantly by using coarse mesh combined with P^{3}M-EMC approach. For the same size of the mesh, even with the additional computations, simulation time of P^{3}M-EMC is close to that of PM-EMC because the simulation time is mainly determined by the calculation of 3-D Poisson's equation.

4.2 Analysis of Coulomb Scattering using P^{3}M-EMC Simulation

In this section, both kinds of Coulomb scatterings, i.e., carrier-carrier and carrier-impurity scattering, are considered by P^{3}M-EMC simulation.

The influence of carrier-carrier scattering has been controversial for decades and it needs to be analyzed as the carrier density increases in highly scaled devices, which may make it more important. Furthermore, analysis of carrier-impurity scattering has great importance in two aspects. One is the analysis of random dopant fluctuation. As the volume of the semiconductor device decreases super-linearly, stochastic variations in number and positions of impurities are becoming more influential on the device performance [54–58]. Device characteristics such as threshold voltage (V_{th}) and on-current (I_{on}) can vary significantly due to the intentional or unintentional dopants diffused from the adjacent region. These variations in number and position of dopants as shown in Fig. 4.8 are called random dopant fluctuation (RDF), which is one of the key obstacles to device development currently and in the near future [59]. The other is the analysis of the ionized impurity scattering inside the heavily doped source and drain regions. As a result of continuous scaling, dimensions of the source and drain regions have significantly decreased as well as the channel region. The trend results

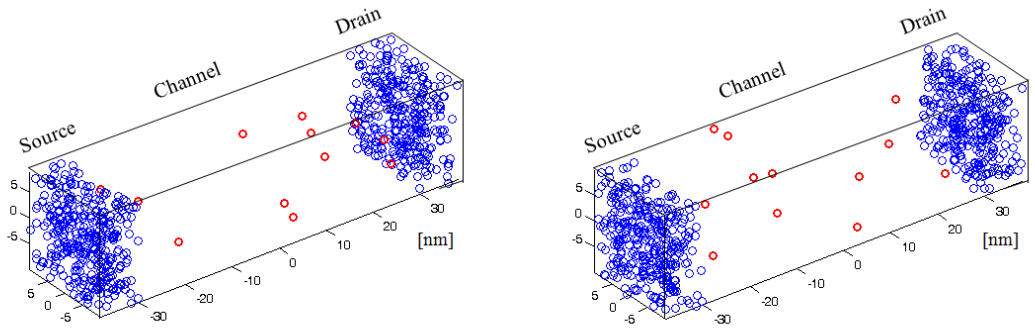

(a) (b)

Figure 4.8: Examples of random dopants in MOSFETs. Channel doping is set to 5×10^{17} /cm^3 and source/drain doping is set to 1×10^{20} /cm^3.

in the undesirable increase of source and drain series resistance. Therefore, the application of heavily doped source and drain is inevitable.

Meanwhile, the channel doping has decreased with the introduction of fully depleted multi-gate structures including FinFET, trigate, and surround-gate-transistor (SGT) [2, 5, 7, 60]. Consequently, the number of scatterings inside the channel is expected to decrease due to the scaling and the lightly or undoped channel. Accordingly, the impurity scattering inside the heavily-doped source and drain region is expected to become more important to the device performance [9].

In MOCA3D, the effect of carrier-impurity scattering is included using the scattering rate method based on Ridley's model [50]. In this model, scattering depends on the mesh defined impurity concentration. This implies that the method cannot properly treat the granular effect which is essential for the analysis of RDF. Furthermore, the heavily doped source and drain regions may show various effects including plasma oscillation, i.e., self-consistent spatiotemporal variations of the electron density and electric field [61]. It is difficult to treat these effects using the mesh defined doping concentration. We believe that our P^3M method can be used for the analysis of granular effect including RDF inside the channel and the carrier-impurity interaction inside the heavily doped source and drain.

For the rest of the chapter, double gate structure is used for the analysis (see Fig. 4.9). One of the merits of the structure is that the same structure can be used for the comparison with the 2-D simulation.

4.2.1 Electrostatic potential energy

Average thermal energy of an electron is known to be about $\frac{3}{2}kT$, which is 38 meV at 300 K. If we assume that electrons are an ideal gas inside an isolated system, the total energy would be $\frac{3}{2}NkT$, where N is the number of electrons.

However, the expression is valid only for the ideal gas, in which particles do not interact with each other. On the other hand, electrons inside the heavily doped contact region can be considered as a non-ideal gas and they are interacting with each other. Therefore, the

electron energy can deviate from the value $\frac{3}{2}kT$. Moreover, as in real devices, we introduce discrete point charges rather than conventional continuous doping for source and drain. Therefore, the interpretation of the electron kinetic energy can be quite different from the conventional knowledge.

As we include the discrete charges, the electrostatic potential energy will also be included depending on the configuration of the discrete dopants. The electrostatic potential energy, U_E, can be expressed as

$$U_E = \frac{1}{4\pi\varepsilon}\frac{q_i q_j}{r_{ij}} \tag{4.1}$$

where q is the electric charge, ε is the dielectric constant, and r is the distance between two particles i and j.

In order to understand the electrostatic potential energy, let us assume two stationary charge particles with infinite distance in between. One is an electron and the other is a positive charge. Due to the infinite distance, electrostatic potential energy will be zero as we can expect from the equation (4.1). Besides, the kinetic energy of the two particles will be zero since they are at rest. When we move the electron i slowly to the positive ion j, without changing of kinetic energy of i, the stored energy – or, in other words, required work – represents the electrostatic potential energy.

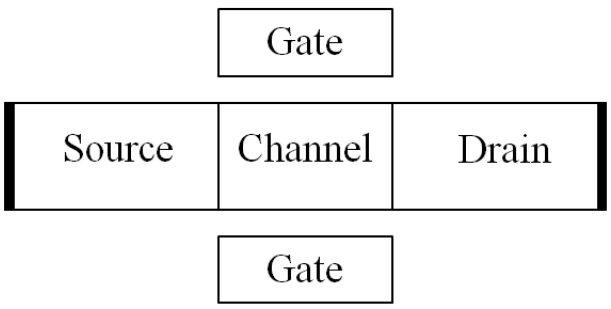

Structure	:	Double-gate structure
Gate length	:	40 nm ~ 60 nm
Si thickness	:	20 nm
Si depth	:	30 nm
Bias conditions	:	V_{GS}=V_{DS}=1.0 V
Channel doing	:	B 1×10^{10} /cm^3
S/D doping	:	As 3×10^{19} /cm^3

Figure 4.9: Double-gate structure is used for the analysis of Coulomb scattering. Doping concentrations are varied depending on the simulation conditions.

In this example, the electrostatic potential energy is negative since the charges have opposite signs. As explained, the basic assumption of this electrostatic potential energy is that the kinetic energy does not change as it approaches the other particle.

In reality, however, we can expect the increase of corresponding kinetic energy rather than the storage of negative potential energy since the electron will gain speed as it approaches the positive ion due to the attractive force between them.

4.2.2 Comparison with the PM method

As described above, the introduction of electrostatic potential energy can explain the increase of electron kinetic energy inside the contact region as in Fig. 4.10. Electrons are injected at the left side of source region and their kinetic energy will increase as many positive ions are attracting from the right side. However, the energy will decrease as they pass more than half of the source region and leave more positive ions behind. The drop of the average energy is obvious in Fig. 4.10. Figure 4.11 shows the average kinetic energy of electrons along the

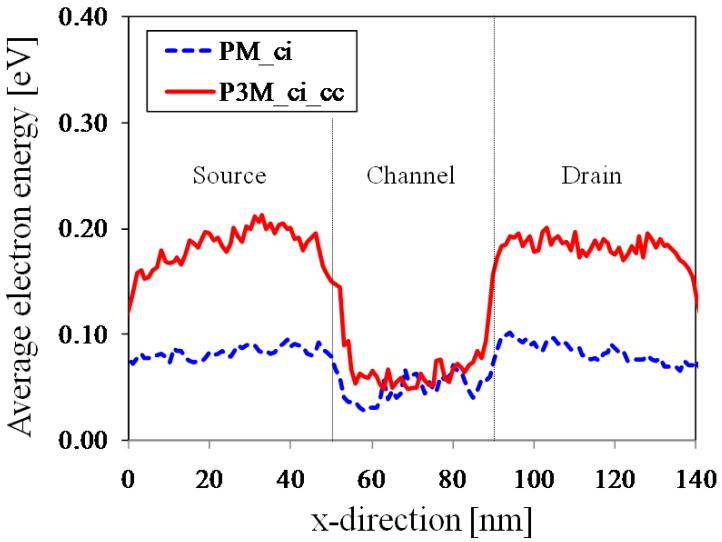

Figure 4.10: Average energy of the electrons in double gate structure with Vg=Vd=0.5 V. Electron energy especially inside the source and drain gets much higher by the introduction of discrete dopants. In the case of P^3M, the average carrier energy drops and increases sharply as carriers leave the source and approach the drain region, respectively.

channel when Vg = Vd = 1.0 V. Figure 4.12 shows the corresponding average speed, v, which can be calculated by $\sqrt{{v_x}^2 + {v_y}^2 + {v_z}^2}$. As we can expect from the increased kinetic energy, average speed of the electrons with discrete dopants is higher than with the scattering rate method. Figure 4.13 shows average velocity of the electrons along the channel, i.e. the direction of the current flow. One of the important findings from Figs. 4.11, 4.12, and 4.13 is that even with the increased kinetic energy and speed, the velocity in channel direction is close to that of continuous doping. To the best of our knowledge, conventional scattering rate methods for the impurity scattering are designed to reproduce the measured mobility. Furthermore, a fit function needs to be included to improve the accuracy of the method for highly doped cases [35]. Basically, the mobility represents the velocity of the carriers under the action of given electric field. In our simulation, Coulomb's law accounts for the behavior of the electrons including carrier-carrier and carrier-impurity scattering. Accordingly, the mobility inside the contact is also treated by Coulomb's law. In this regard, based on the results from Fig. 4.13, we believe that the mobility or the current inside the source and drain regions for the PM and the P^3M methods are quite similar.

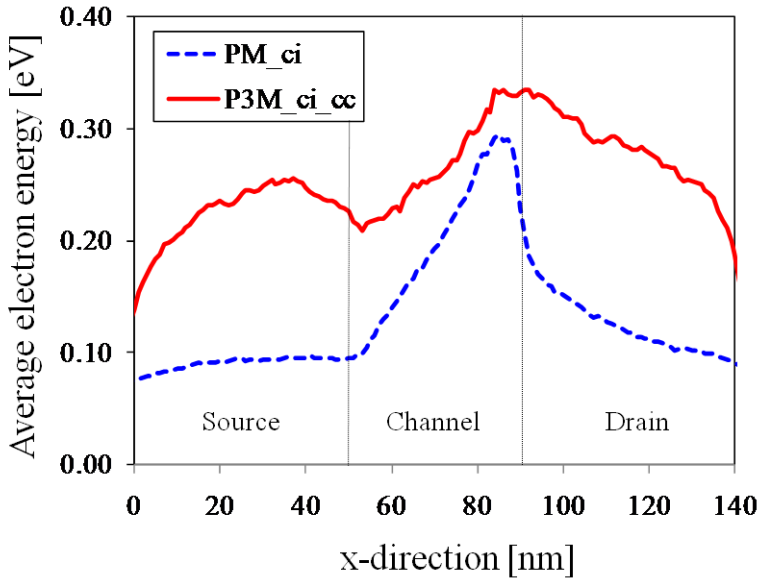

Figure 4.11: Average energy of the electrons in double gate structure with Vg=Vd=1.0 V. High energy inside the contact also affects the energy inside the channel significantly.

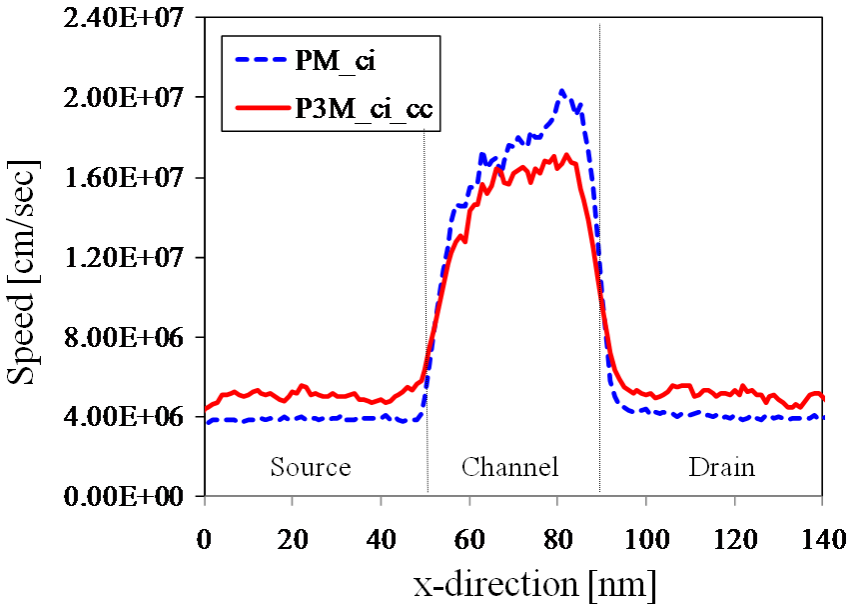

Figure 4.12: Average speed of the electrons along the channel. P^{3}M shows higher speed inside the contact region and lower speed inside the channel.

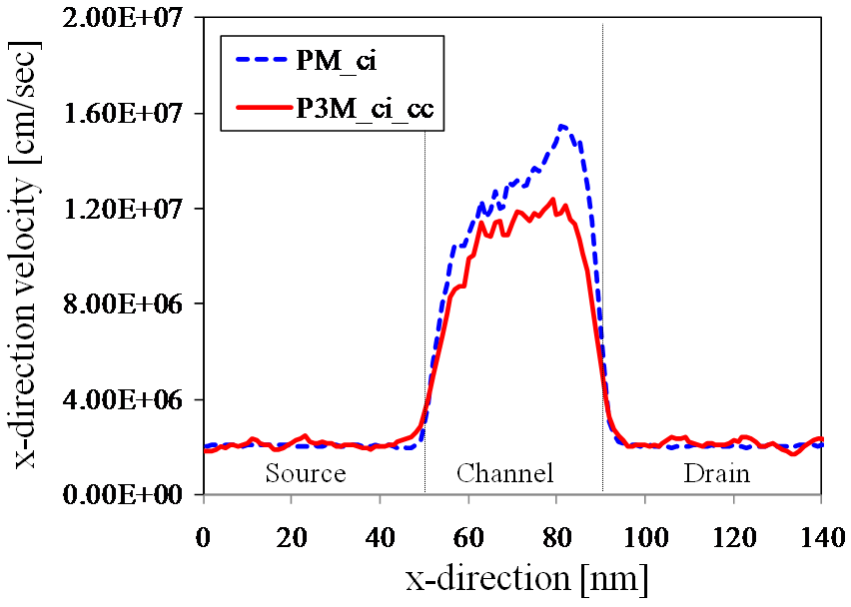

Figure 4.13: Average net velocity of the electrons along the channel. P^{3}M shows similar velocity with PM inside the contact region and lower velocity inside the channel.

However, we can also notice that the speed and the velocity of the electrons inside the channel are quite different. Probably, this is due to the average energy difference of injected carriers into the channel.

We expect that it will be more difficult to accelerate energetic – in other words, high-speed – carriers with given electric field inside the channel. Therefore, the speed or the velocity inside the channel is lower in the case of P^3M. This is one of the most important observations since the decrease of the velocity inside the channel is expected to result in decrease of on-state current. In this example, the on-current is reduced by 12.2%. The reproduction of mobility curve in PM method can show that carrier velocity in source and drain can match the experimental data. However, due to the uncertainty and non-linear properties inside the channel, there is no proper way to confirm whether the scattering rate method holds inside the channel or not. Therefore, match with an n-type resistor does not necessarily mean that the method can also be applied for the channel region especially when the model includes fitting parameters.

Our approach, on the other hand, can match the mobility curve using Coulomb's law and does not include any fitting parameter, which will be discussed later. We believe that the electrostatic properties including Coulomb's law are also true in the channel, and thus the behavior of the carriers can be described properly. Furthermore, the screening effect, which is hard to deal with using scattering rate method, can also be treated implicitly by the forces between charge particles.

To support the validity of the P^3M method over the PM method, we varied the initial condition of the injected electrons for both cases. The average energy of the injected electrons is varied and the results are shown in Figs. 4.14 and 4.15.

In the source region of the PM method, we can clearly notice that the energy of the electrons with initial energy of 26 meV is higher than for the 1 meV case. And the energy inside the channel and drain also shows considerable change. However, in the case of the P^3M, the change is reduced significantly and thus shows that the method is insensitive to the initial condition of the carriers.

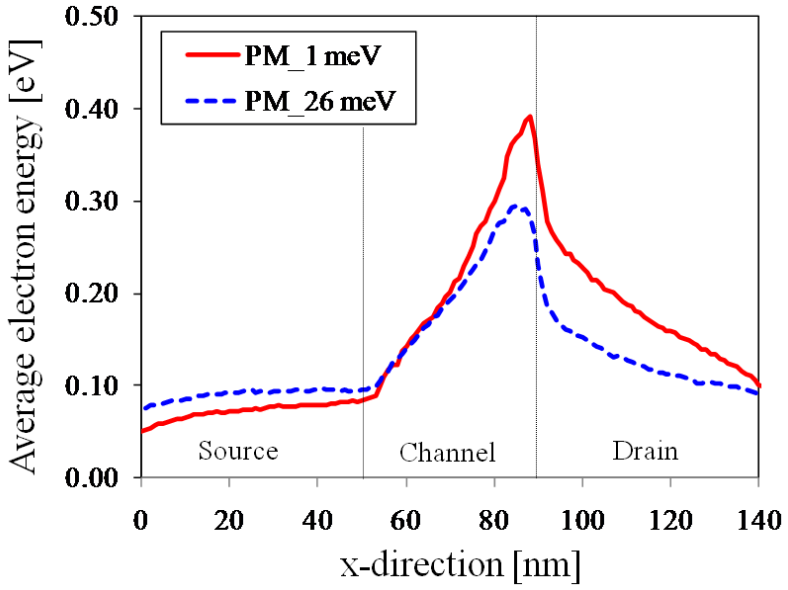

Figure 4.14: Average energy of the electrons as a function of initial electron energy for the PM method. We can notice that the initial condition has strong influence on overall energy distribution.

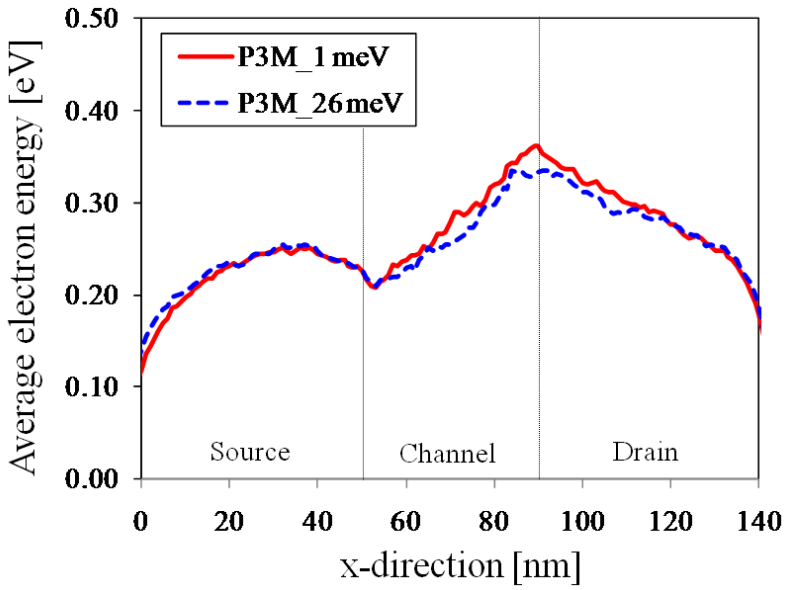

Figure 4.15: Average energy of the electrons as a function of initial electron energy for the P^3M method. We can notice that the influence of initial condition has been reduced significantly by the P^3M method.

In terms of the on-current, the PM method shows 77.6 μA and 62.3 μA for the 1 meV case and 26 meV case, respectively. The corresponding currents for the P^{3}M method are 57.5 μA and 56.4 μA, which also shows insensitivity to the initial condition.

Figure 4.16 shows electron distributions inside the source region for two cases. Here again we see the increased energy inside the source by P^{3}M and less sensitivity to the variation of initial electron energy.

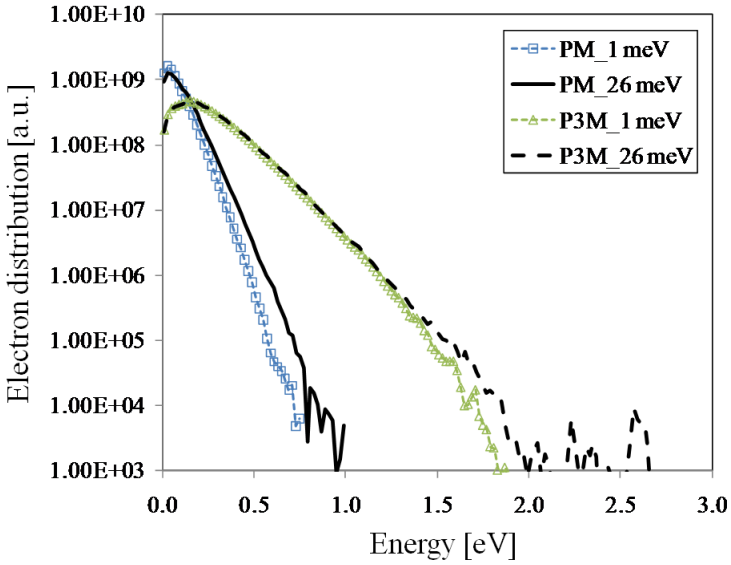

Figure 4.16: Electron distribution as a function of energy. The electron energy with discrete dopants is much higher than that with continuous doping. And the P^{3}M method is less influenced by initial condition.

4.2.3 Considerations on carrier-carrier and carrier-impurity scattering

In Fig. 4.17, we compare the influence of the carrier-carrier scattering and the carrier-impurity scattering. We observe that electron energy is increased slightly by the implementation of carrier-carrier scattering. On the other hand, the carrier-impurity scattering shows significant change of electron energy which also affects the channel region. Overall, the carrier-impurity scattering dominates over carrier-carrier scattering. The trend also can be found in Fig. 4.18, which shows the changes in on-current as we include carrier-carrier scattering and/or carrier-impurity scattering. The corresponding electron energy distributions can be found in Figs. 4.19, 4.20, and 4.21.

It is worth analyzing the reason for the significant differences between two Coulomb scatterings. In our simulation frame, there are a couple of differences between two scattering mechanisms. In the case of carrier-carrier scattering, both carriers are free to move to maintain the distance between them. In carrier-impurity scattering, on the other hand, ionized impurity is considered as a fixed particle.

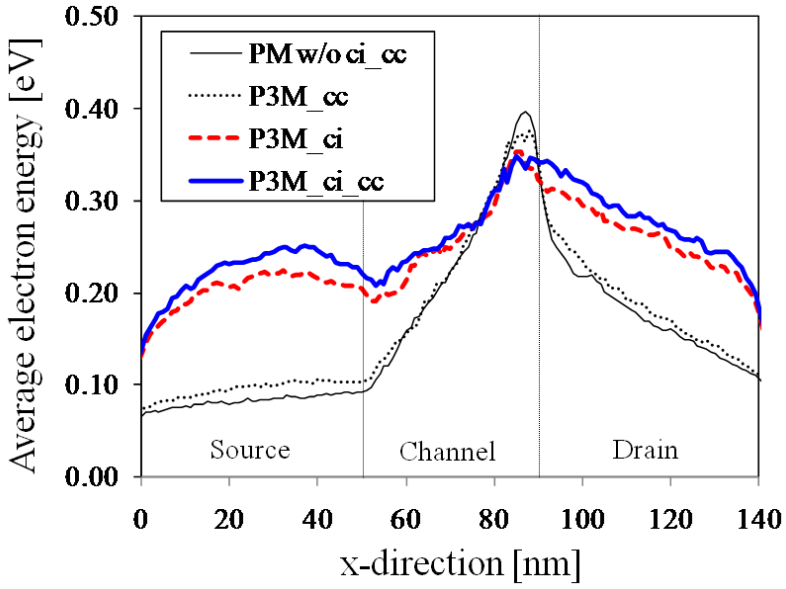

Figure 4.17: Average electron energy along the channel. The increase of electron energy is mostly due to the carrier-impurity interaction.

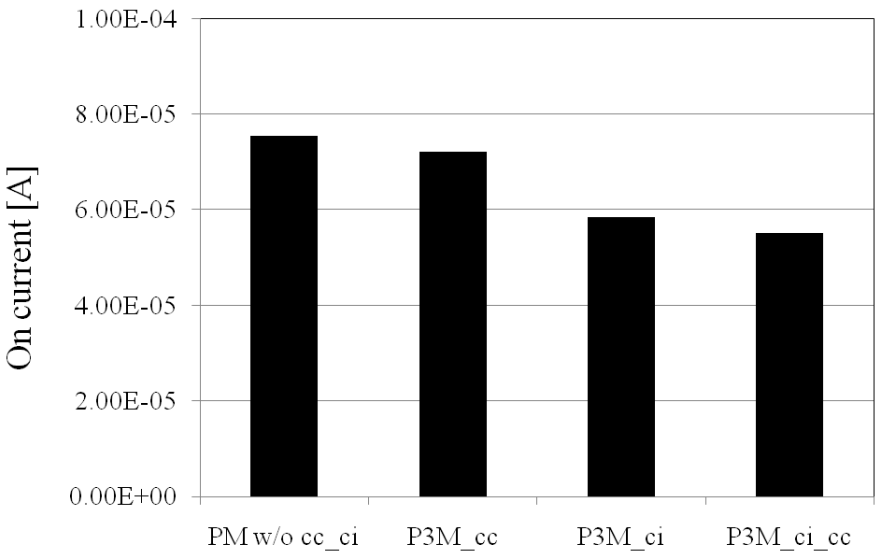

Figure 4.18: On-current according to the configuration of the simulation. We can notice that the the decrease of current is mainly due to the carrier-impurity scattering. Carrier-carrier scattering also contributes to the decrease of on state current.

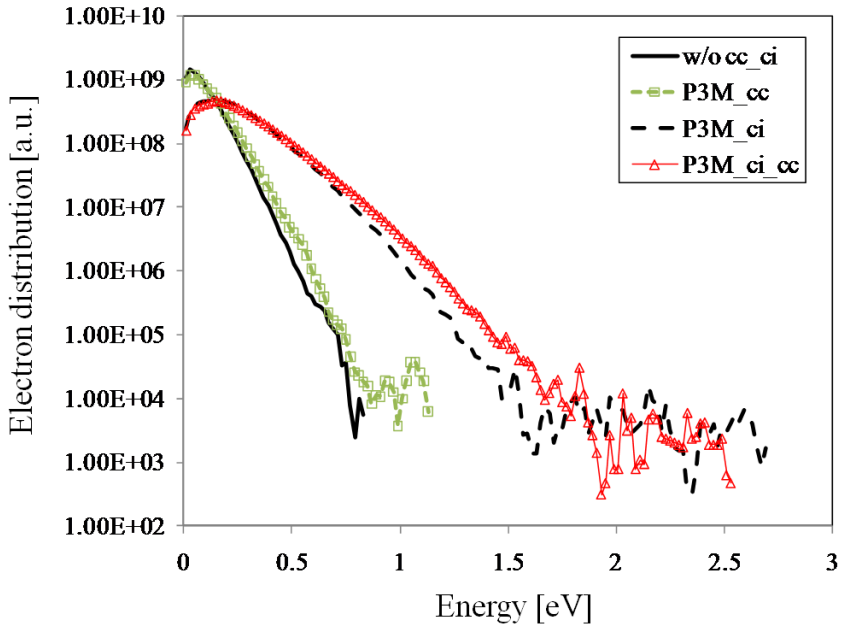

Figure 4.19: Electron distribution inside the source. Electron energy increases mainly due to the consideration of carrier-impurity scattering.

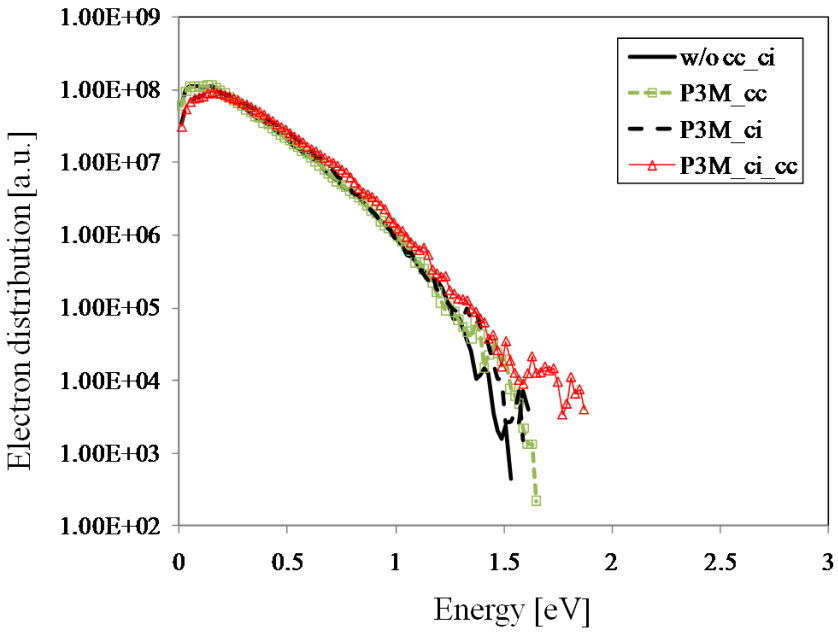

Figure 4.20: Electron distribution inside the channel.

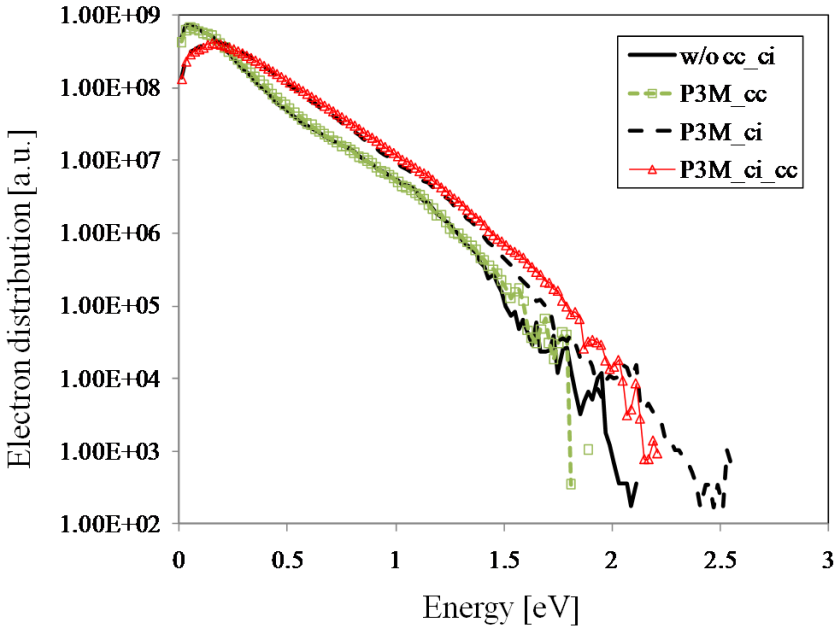

Figure 4.21: Electron distribution inside the drain.

We believe that a more important difference is the nature of the force between them. For instance, inside the source and drain region with n-type dopants, the force between electrons is repulsive but that between electron and ionized impurity is attractive. In order to evaluate the difference, we observed the number of short-range interactions and the average distance of them for a certain amount of time.

Table 4.1 shows that the number of short-range interactions between carrier and impurity is more than twice the number of carrier-carrier scatterings. Furthermore, the average distance between interacting particles is smaller. Figure 4.22 shows the number of scatterings as a function of distance between charge particles. Considering the fact that the force between two charge particles is inversely proportional to the square of the distance, we also plot the influence of both scatterings as shown in Fig. 4.23. To some extent, the results explain the reason for the high influence of carrier-impurity scattering.

It is important to note that relatively small change by the carrier-carrier scattering does not necessarily mean that the effect of carrier-carrier scattering is very weak. As shown in the results, the number of carrier-carrier scatterings is less than half the number of carrier-impurity scatterings even though the numbers of both particles are not that different considering charge neutrality. This implies that the repulsive force between electrons inside source and drain tends to maintain the distance between electrons. Therefore, fewer other electrons are inside the short range. In some sense, the electron-electron interactions can be captured by the PM method provided that the mesh size is reasonably small. Remember that during the evaluation of P^3M-EMC simulation using the analysis of carrier-carrier scattering, we observed the considerable influence of carrier-carrier scattering when sparse mesh is applied. On the other hand, the free electrons tend to move close to positive ionized impurities inside the source and drain, which results in more interactions and more influence on the device performance. In this regard, we can conclude that very dense mesh will be required for the PM method to capture the influence of carrier-impurity scattering inside the source and drain.

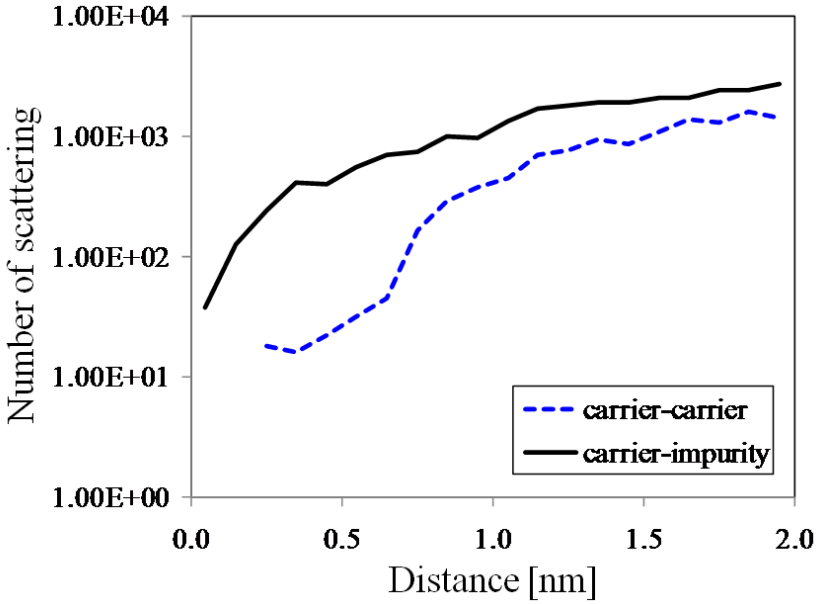

Figure 4.22: Number of Coulomb scatterings inside the short range. We can observe that the carrier-impurity scattering can be dominant considering the frequency and distance between interacting particles.

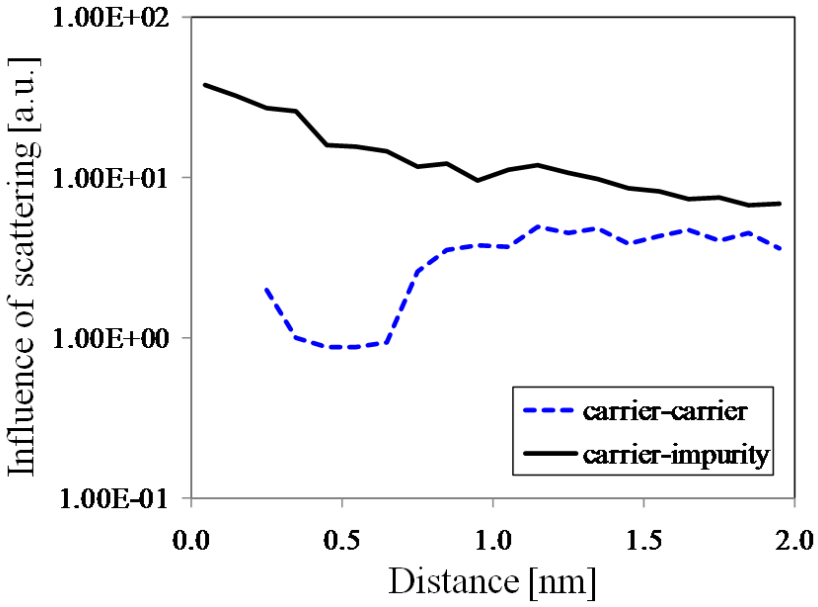

Figure 4.23: Influence of each kind of Coulomb scattering as we consider the distance between interactions. This shows the reason for the much greater influence of carrier-impurity scattering compared to carrier-carrier scattering.

Table 4.1: Number of short-range interactions (r_{sr}=2 nm).

	Carrier-Carrier	Carrier-Impurity
Number	13506	30379
Avg. Distance	1.50 nm	1.31 nm

4.3 Low-Field Electron Mobility Extraction

The validity of the proposed method for the calculation of Coulomb scattering, i.e. carrier-carrier scattering and carrier-ionized impurity scattering, can be verified by low-field mobility calculation.

For the evaluation, an n-type resistor is used and the doping concentrations are varied from 1e15 /cm^3 to 1e20 /cm^3. External bias, which is the source of the directional current flowing, is determined to maintain the constant electric field, 5000 V/cm.

We have learned from the preliminary simulation results that if the applied field is too low, the simulation results show more fluctuations. Accordingly, it is hard to obtain stable mobilities, especially for the heavily doped resistors. It is important to note that variations of device characteristics due to the random dopants are natural in highly scaled devices, however, which also can be an obstacle for the calculation of nominal mobility values. For fair comparison, the size of the resistor is scaled to maintain a number of electrons.

In order to extract the mobility, we need to take into account the situation of mobility measurement. Therefore, it is required to modify the configuration of the simulation in such a way that it imitates the mobility measurement. Figure 4.24 illustrates the resistor used for the simulation. Number and positions of the discrete dopants are randomly generated based on the nominal doping levels.

At the beginning of the simulation, electrons are positioned to satisfy charge neutrality. We defined a mobility calculation region in which electrons drift under the action of the applied field. Even though the local field as a result of local charge distribution can be very high, the direction of the local field is random and thus the average electric field is close to the applied field. Basically, we maintained the distribution of ionized impurities and electrons even for the outside of the calculation region. This is to eliminate the discontinuity of charge

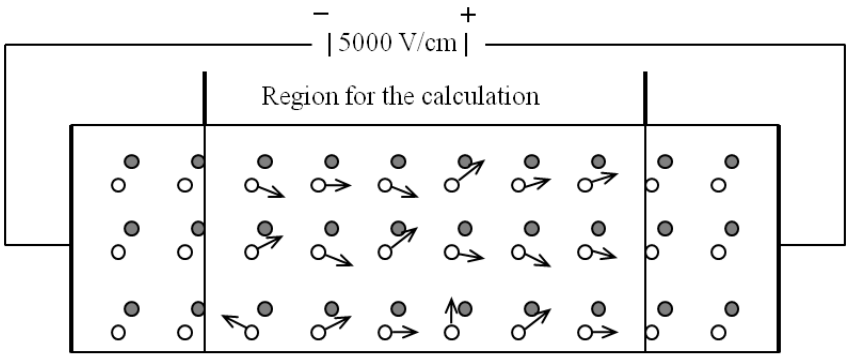

Figure 4.24: Configuration of mobility calculation using n-type resistor. Black dots are positive ions and white circles are free electrons.

distribution at the boundary. However, the positions of the outside electrons are fixed to prevent them from entering the calculation area. Once the electrons inside the calculation region leave the area, they are re-injected at the other side of the calculation region to continue the drift. Furthermore, wave vector **k** is maintained to imitate the situation of continuous drift in bulk silicon. For the interfaces parallel to the applied electric field, mirror-like reflective boundary conditions are applied. Figure 4.25 shows the extracted mobilities as a function of doping concentration, which is in good agreement with experimental data.

Unlike the conventional scattering rate methods, no fitting parameter is used for the mobility extraction. It only relies on the forces based on the long-range self-consistent Poisson's solution and coulombic forces between short-range charge particles. The results confirm that the P^3M method is an effective way to include the Coulomb scattering for a wide range of the doping concentrations.

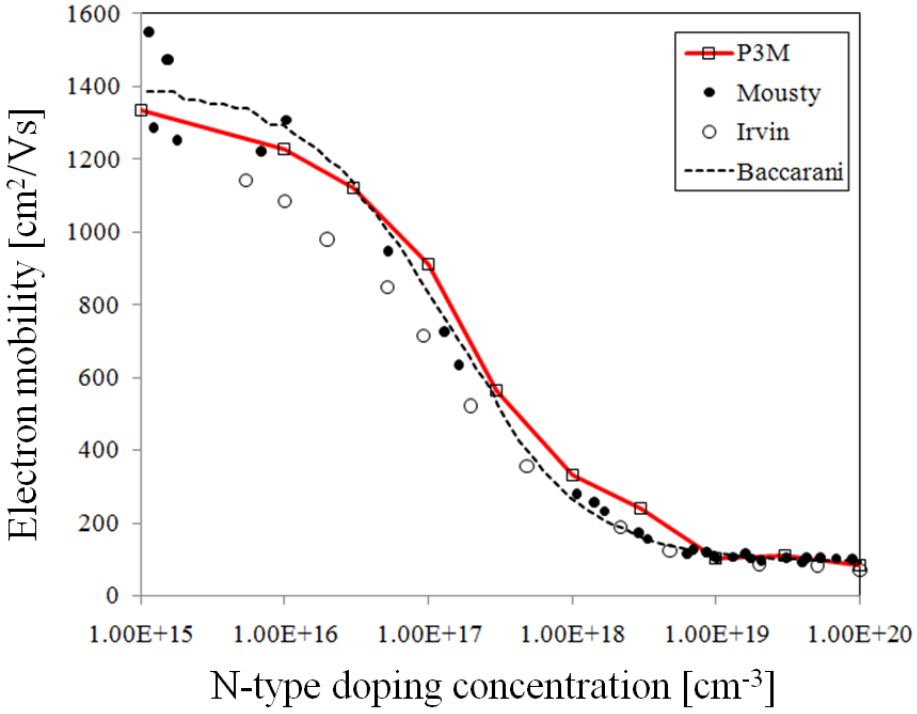

Figure 4.25: Low-field electron mobility as a function of doping concentration of bulk silicon at 300 K. Open and closed circles are the measurement data in [62] and in [63], respectively. The broken line is best fit for [64]. These data are also introduced in [65].

4.4 Analysis of Random Dopant Fluctuation (RDF)

Many researches have been performed to investigate the RDF [57, 58]. However, we believe that the P^3M approach is one of the most accurate methods to treat the granular effect of dopants. The analysis of the RDF is not intended to be performed extensively, but it is worthwhile to verify that the developed method is suitable for the purpose. In this study, we used the on-state current to measure the variability. On-current is closely related to the threshold voltage, V_{th}, which is the most common parameter that can be used to measure the fluctuation. It is worth noting that it is inefficient to obtain V_{th} using the EMC method due to the computational burden.

Figure 4.26 shows examples of random dopants inside the source and drain. Source and drain doping concentrations are varied from 3×10^{18} to 3×10^{20} /cm^3. More than 10 simulations are performed for each doping level to estimate the variation of on-state current. Figure 4.27 shows the average current according to the doping levels. Figure 4.28 shows the standard deviation of on-currents. To estimate the relative variation from the average, standard deviation of the on-current is divided by average on-current for each doping concentration (see Fig. 4.29). The simulation results show that the variation increases significantly as we decrease the doping concentration below 1×10^{19} /cm^3. This implies that we need to maintain heavily doped source and drain to increase the drive current and also to reduce the variability.

We also varied the channel doping from 2×10^{17} to 1×10^{19} /cm^3 for the same structure. Figure 4.30 shows average number of impurities according to the doping concentration. Figure 4.31 represents standard deviation of number of dopants. Standard deviation of on-current (see Fig. 4.32) shows higher deviation with higher channel doping. This trend is even obvious in Fig. 4.33, in which the relative variation of current from average is presented.

This implies that the on-current fluctuation decreases for undoped or lightly doped cases and thus is immune to the fluctuation [57]. In Figs. 4.34 and 4.35, on-currents are compared with the inverse of number of dopants. The results show that in the lightly doped channel, the correlation between number of dopants and current is weak. On the other hand, in the

heavily doped channel, the current is closely related to the number of dopants inside the channel.

We expect that at the early stage of device development, the data of variability as functions of various conditions including doping concentrations can be obtained, which can be used to suggest a guideline for the device configurations.

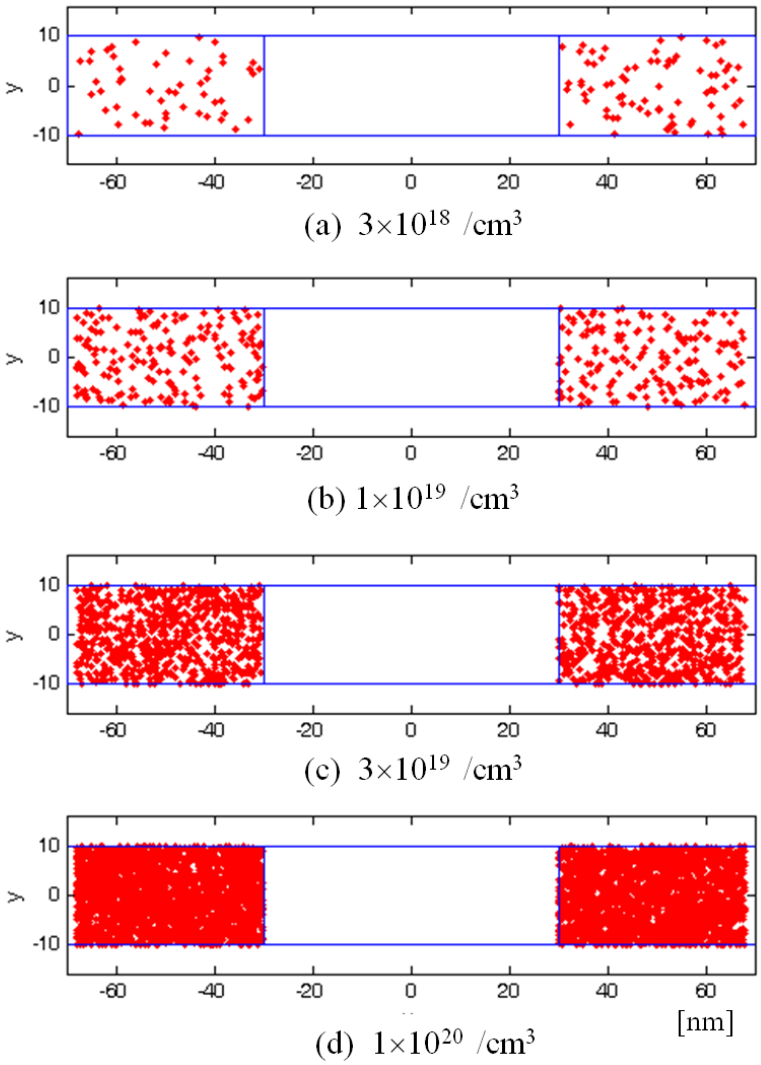

Figure 4.26: Examples of random dopants inside source and drain. X-axis shows the position along the channel direction of double-gate MOSFET. For the simplicity, 2-D view is illustrated here.

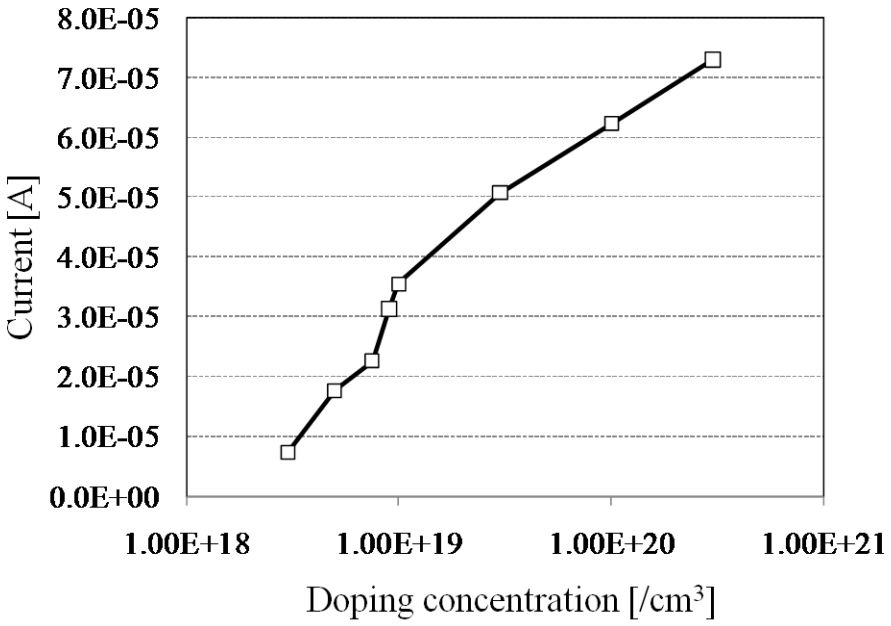

Figure 4.27: Average current as a function of source and drain doping concentration. Dependency on drive current is obtained with the variation of doping level.

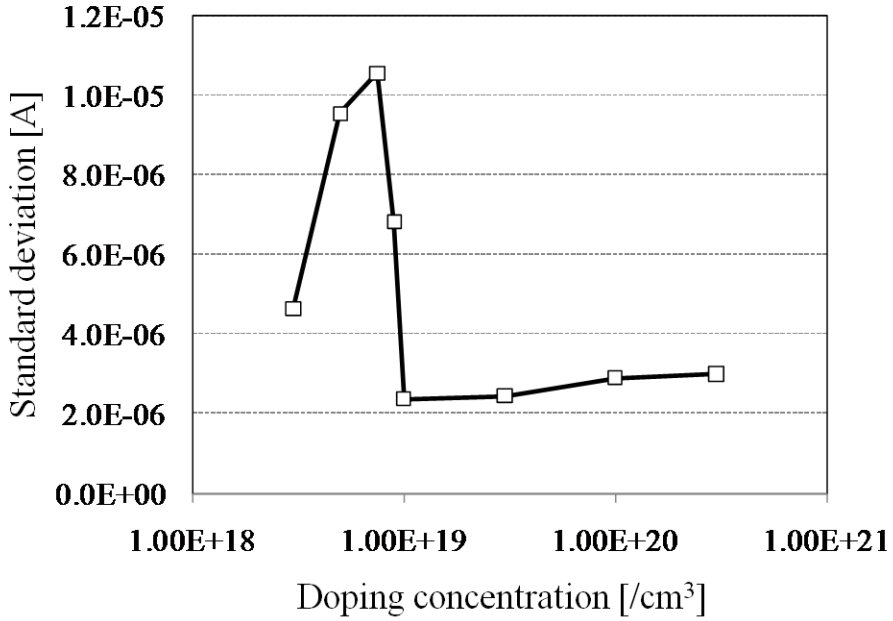

Figure 4.28: Standard deviation of on-current as a function of doping concentration.

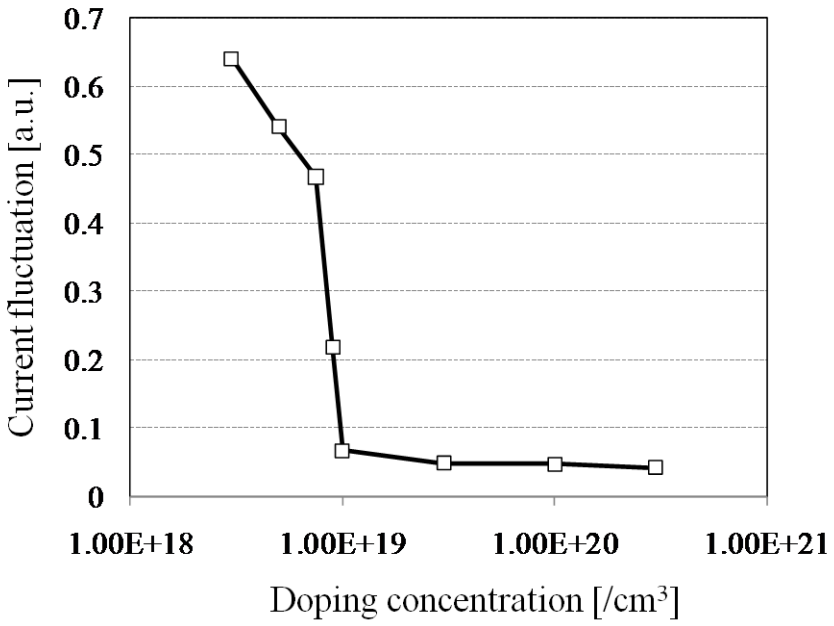

Figure 4.29: Current variation as a function of doping concentration inside the source and drain. Standard deviation of the current divided by average current is used to describe current fluctuation.

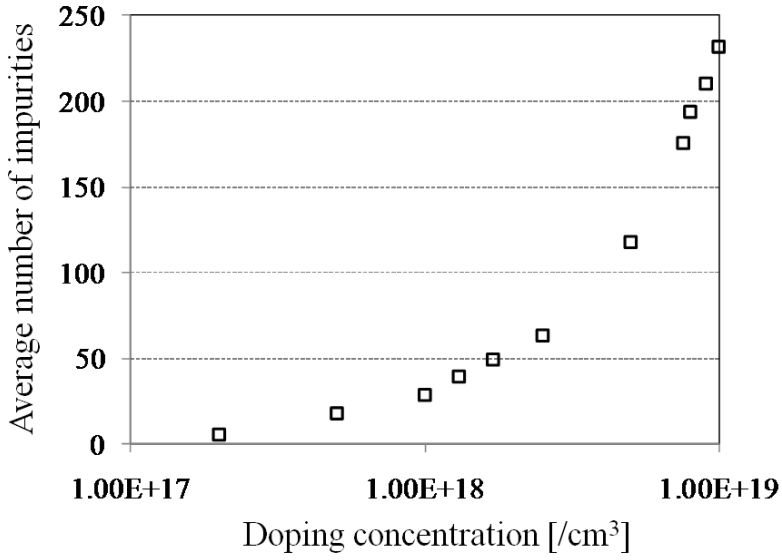

Figure 4.30: Average number of ionized impurities inside the channel. The volume of the channel region is set to 3.6×10^{-17} cm^3.

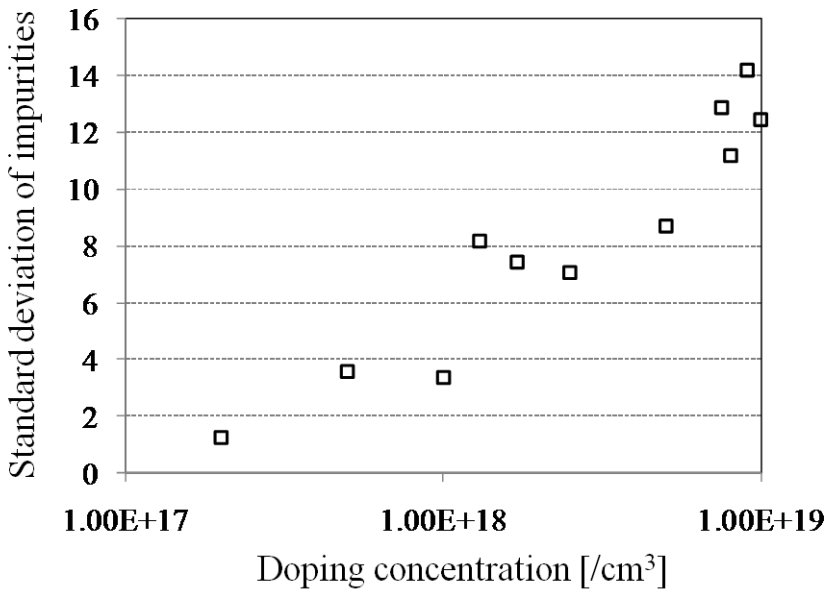

Figure 4.31: Standard deviation of number of impurities as a function of doping concentration.

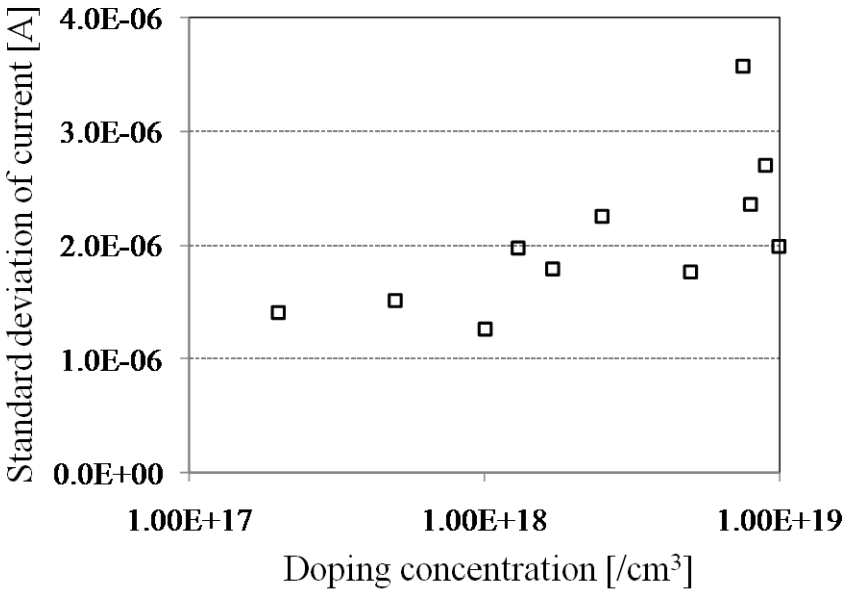

Figure 4.32: Standard deviation of current as a function of doping concentration.

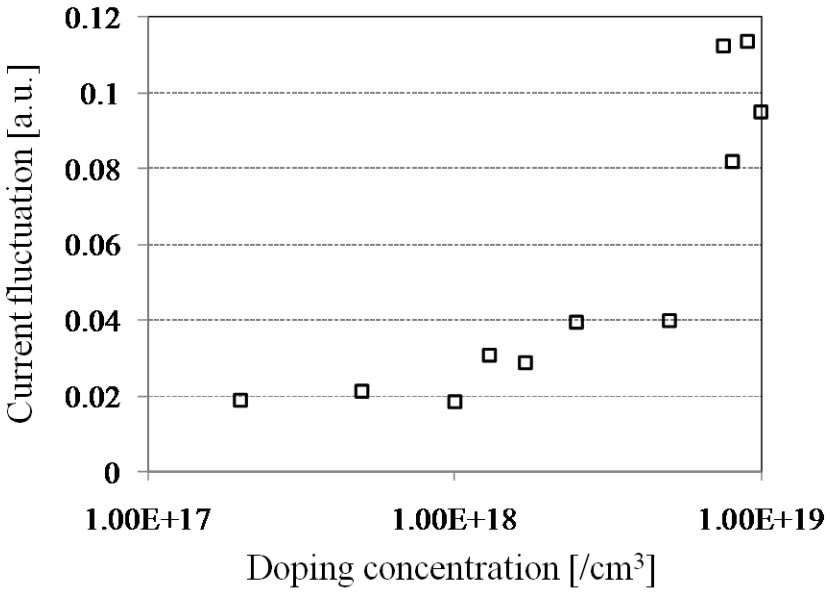

Figure 4.33: Current variation as a function of doping concentration inside the channel. Standard deviation of the current divided by average current is used to describe current fluctuation.

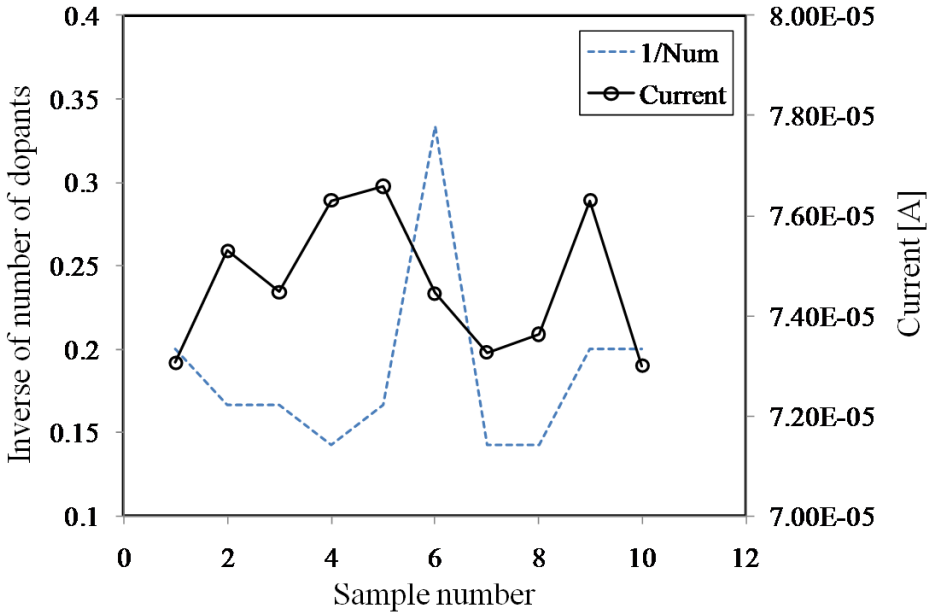

Figure 4.34: Variation of current as a function of number of dopants. Channel doping is set to $2 \times 10^{17}/\text{cm}^3$.

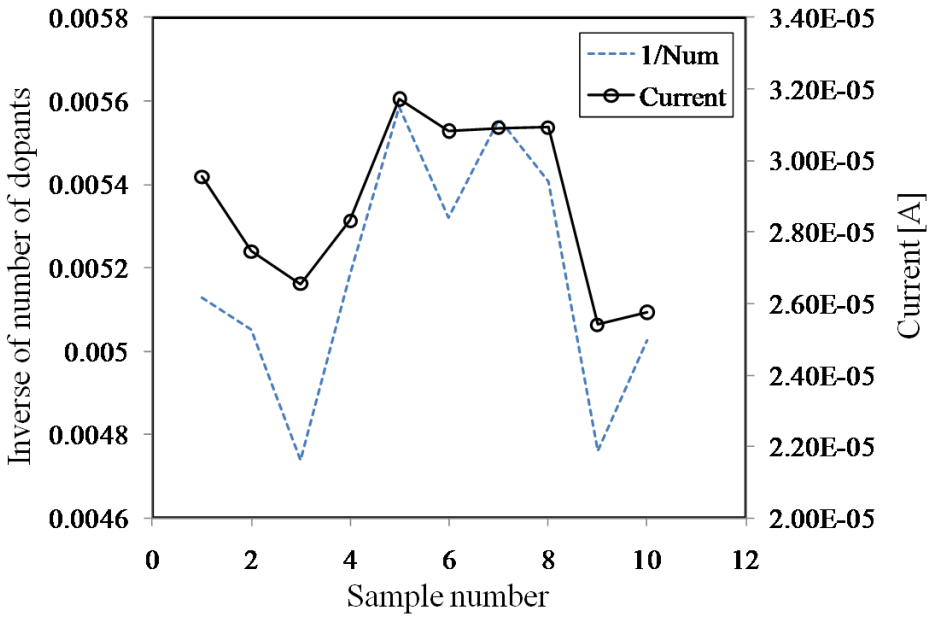

Figure 4.35: Variation of current as a function of number of dopants. Channel doping is set to $8 \times 10^{18}/\mathrm{cm}^3$.

4.5 Conclusion

The modified P^{3}M method introduced in the previous chapter is implemented on the EMC simulator, MOCA3D. The evaluation is performed and the properties of the P^{3}M based method are compared with those of the PM based method. This can also be considered as a comparison between the P^{3}M based method and the scattering rate based method for Coulomb scattering.

The critical shortcomings of the PM based scattering rate method are presented. We show that the energy of the carriers can be lowered by the Coulomb interaction due to the limitation of mesh force calculation for the short-range charge particles. And the limitation is a function of mesh size, which makes the problem more complicated to solve. We also show that the energy loss by the interaction can be avoided by the application of P^{3}M. The evaluation results based on the distribution function, carrier energy, and on-current reveal that the accuracy of the force between particles can be maintained for a wide range of mesh

sizes as we apply the P^3M method. Accordingly, up to 80∼90% of simulation time can be saved by the P^3M method while achieving the same accuracy as the PM method.

The average energy profile of carriers is obtained after we introduce discrete dopants, which shows that the energy can be quite different than previously thought. The higher energy inside the contact is explained with the concept of electrostatic potential energy.

The device simulations with carrier-carrier and carrier-impurity scattering show that, in particular inside the contact, the impurity scattering is more influential than carrier-carrier scattering. The source of the differences between two scattering mechanisms is discussed. We show that carrier-impurity interactions are more frequent and stronger than carrier-carrier interactions.

Mobility extraction using n-type resistor shows that the proposed method can reproduce measured data only with the long-range self-consistent electrostatics and the Coulomb force inside the short range.

Furthermore, RDF is analyzed using P^3M-EMC simulator as a function of source/drain doping and channel doping. The simulation shows that the method can be used to obtain various properties with the random variation of variables.

CHAPTER 5

APPROXIMATE TWO–DIMENSIONAL P^{3}M METHOD

In this study, a 2-D P^{3}M method is developed for the calculation of carrier-carrier scattering and carrier-impurity scattering in 2-D EMC frame. Despite the conceptual difficulties of considering discrete charges in 2-D MC, it is an attractive option considering wide applications of 2-D MC due to its simplicity and computational advantages.

5.1 Introduction to 2-D P^{3}M Method

2-D MC simulation is still considered as a very popular approach for the carrier transport simulation. In this regard, the development of a 2-D P^{3}M method is expected to improve the performance and accuracy of the 2-D particle-based simulations. Moreover, the comparison with the 3-D P^{3}M can measure the validity and the limitations of the 2-D MC simulations.

In order to develop the 2-D P^{3}M method, we need to obtain the equation for the 2-D electric field calculation. The equation is based on the assumption that a charge is described as a line charge rather than a point charge. The derivation starts from the electric field from a line charge as described in Fig. 5.1. Using Gauss's law, equation (5.1), the electric field between two line charges can be equation (5.2). Based on the equation, the direct force and the reference force can be calculated by equation (5.3) and equation (5.4), respectively.

In Fig. 5.2, we compare the obtained equation with the solution of the 2-D Poisson's equation. We successfully show that the equation (5.3) is equivalent with the the 2-D Poisson's equation. Moreover, the equation (5.4) can also be used to reproduce the 2-D local mesh force, i.e., the reference force, which enables us to eliminate the double counting mesh force inside the short range (see Fig. 5.3).

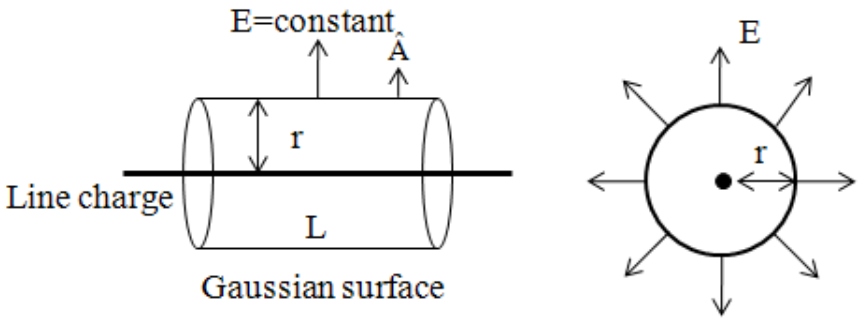

Figure 5.1: Illustration of electric field, **E**, from a long line charge with distance **r**. The electric field is perpendicular to the line charge and has the same value at any fixed distance from the line charge. The same expression can be used to calculate electric field between two long line charges when we assume a charge is distributed evenly along a line.

$$\begin{aligned}
\oint_{surface} \vec{E} \cdot d\vec{A} &= \frac{q}{\varepsilon} && (5.1)\\
&= \oint_{Cyl} \vec{E} cos(\theta) dA = \int_{Walls} \vec{E} cos(0) dA + \int_{Ends} \vec{E} cos(\frac{\pi}{2}) dA \\
&= E \int_{Walls} l dA + E \int_{Ends} 0 dA = E \int_{Walls} l dA = \int_0^L 2\pi r dl = E 2\pi r L \\
E &= \frac{q}{2\pi\varepsilon} \frac{1}{rL} && (5.2)
\end{aligned}$$

where q is the electric charge, ε is the dielectric constant, r is the distance, and L is the specified length of a line charge. Direct and reference force equations for 2-D are very similar with 3-D, described as

$$F_{ij} = \frac{q_i q_j}{2\pi\varepsilon L} \frac{(r_i - r_j)}{|r_i - r_j|^2} \quad (5.3)$$

$$F_{ij}^r = \sum_{m \neq n} \frac{w_{i_n} w_{j_m} q_i q_j}{2\pi\varepsilon L} \frac{(r_{i_n} - r_{j_m})}{|r_{i_n} - r_{j_m}|^2} \quad (5.4)$$

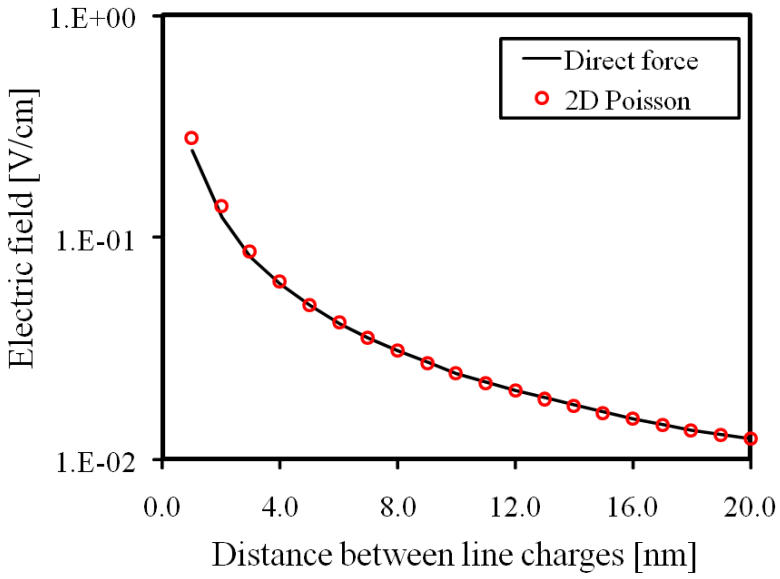

Figure 5.2: Electric field versus distance between line charges. The circles show the electric field by the 2-D Poisson equation. The solid line is from the obtained equation (5.3). In this figure, L is set to 1 cm.

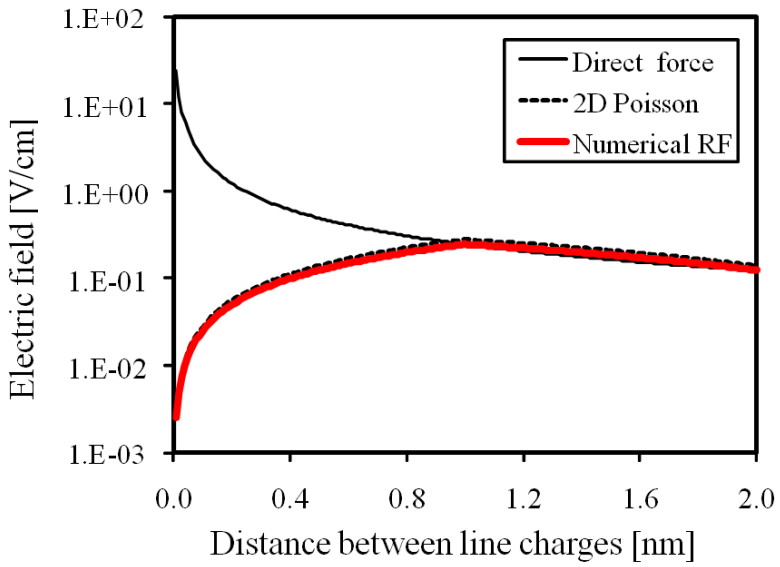

Figure 5.3: Reference forces (RF) and the direct force are described. Numerical RF is based on equation (5.4). CIC scheme is used and r_{sr} is set to 2 meshes (i.e. 2 nm). Uniform square mesh, 1×1 nm, is used and the particle i is assumed to be at the mesh node and j is moved along the mesh line.

5.2 Implementation of 2-D P^3M Method

The main challenge in 2-D P^3M arises from the inherent assumption of the 2-D particle-based simulations. A charge particle is considered as a line charge on which an elementary electric charge is evenly distributed as shown in Fig. 5.4 (a). A more realistic picture of the point-like charges can be illustrated as Fig. 5.4 (b) and (c).

In 2-D P^3M, we noticed that the simple implementation of equation (5.3) was not sufficient for the direct force in short range. Our evaluation results revealed that the direct force from equation (5.3) was too weak to reproduce the strong coulombic force between short-range point charges (see Table 5.1).

To cope with the problem, we introduce quasi 3-D approach, in which we randomly generate imaginary positions in z-direction for the particles inside the 2-D short range (see Fig 5.5 (a)) as shown in Fig 5.5 (b). Therefore the distance between two charge particles can be calculated using the position of the third direction. Consequently, Coulomb's law in 3-D can be applied to obtain coulombic short-range forces as in 3-D P^3M approach.

Figures 5.6, 5.7, and 5.8 show the change of distribution function as we include carrier-carrier scattering and/or carrier-impurity scattering. The distribution functions can be compared with 3-D cases (see Fig. 4.19, 4.20, and 4.21), which show reasonable agreement. In the source region with 3-D P^3M, the influence of carrier-impurity scattering is much higher than that of carrier-carrier scattering, which can be done naturally in 3-D with coulombic force calculation as explained in the previous chapter. In 2-D, on the other hand, the effect of carrier-carrier scattering is suppressed and the effect of carrier-impurity scattering is enhanced to match the shape of 3-D. It is necessary in the sense that the force between line charges in 2-D is not strong enough to make reasonable movements of the particles.

Table 5.1: Electric field as a function of particle distance in 2-D and 3-D [V/cm].

	1.0 nm	0.1 nm
3-D	1.2e6	1.2e8
2-D	4.8e3	4.8e4

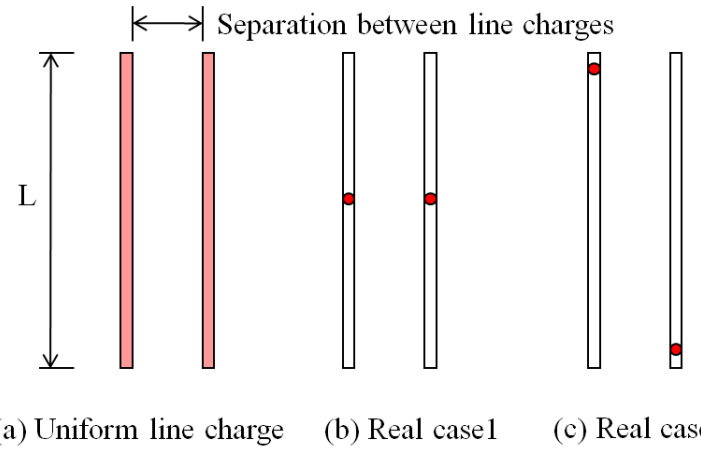

Figure 5.4: (a) Illustrates the charges in 2-D particle-based simulations. Notice that the vertical lines represent the depth (z) direction in 2-D (xy) simulation. A charge is uniformly distributed on a line which extends specified depth L. In reality, the charge particles can be as close as the 2-D separation itself as in (b) or the distance can be larger than L as in (c).

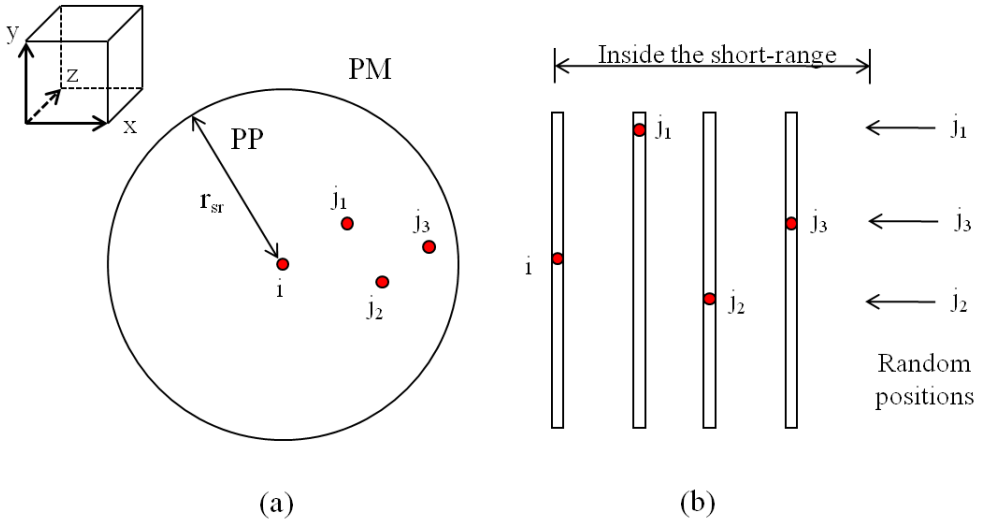

Figure 5.5: (a) Illustrates an example of charges inside the short range in 2-D MC simulation. (b) Shows the random positions of partner particles j_1, j_2, and j_3. After the distance evaluation with primary particle i, the simulator can decide which particles belong to short range and they will be considered in the calculations.

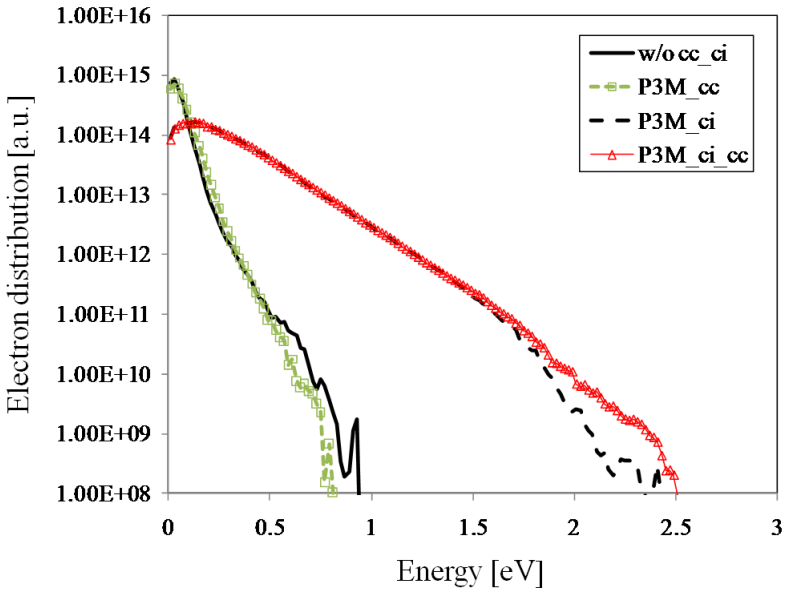

Figure 5.6: Electron distribution inside the source. The graph can be compared with Fig. 4.19 in 3-D.

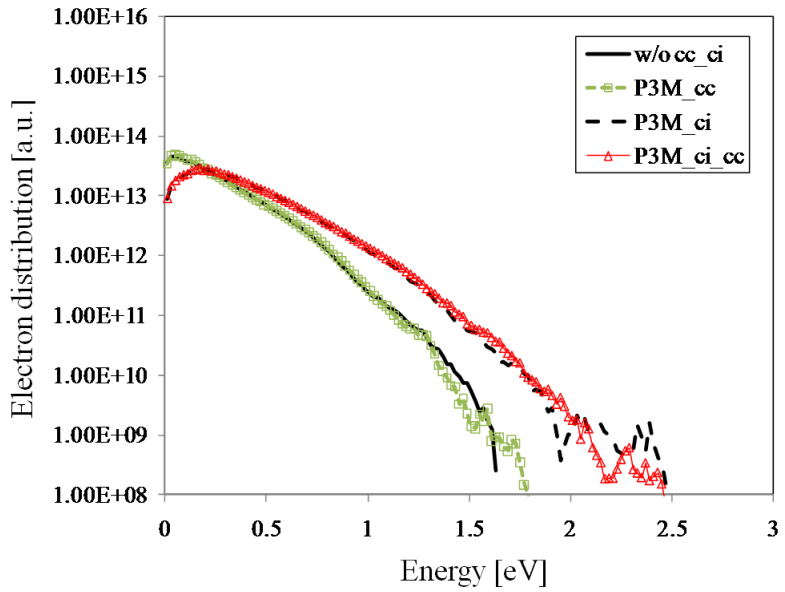

Figure 5.7: Electron distribution inside the channel. The graph can be compared with Fig. 4.20 in 3-D.

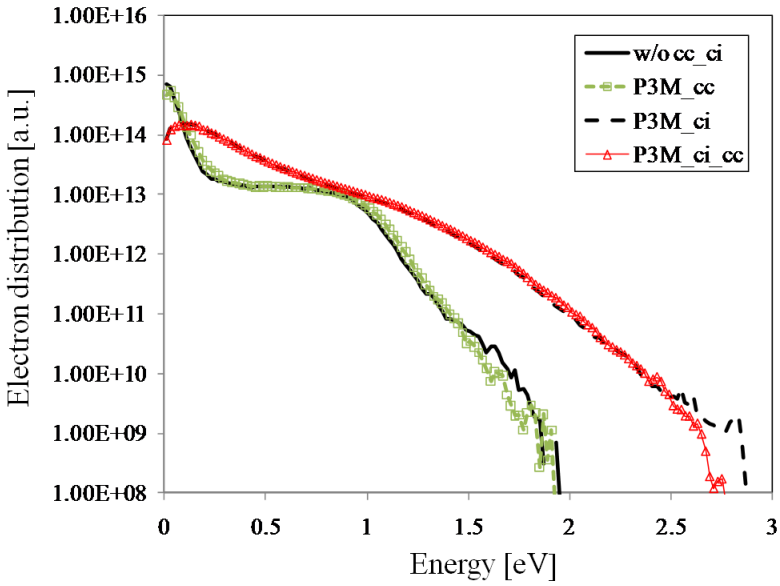

Figure 5.8: Electron distribution inside the drain. The graph can be compared with Fig. 4.21 in 3-D.

Low field mobilities are calculated using an n-type resistor as in 3-D. The number and the positions of the discrete-dopants are generated randomly for various doping levels. Carriers leaving the resistor are re-injected on the other side with the same wave vector, **k**, to mimic the situation of bulk simulation. Figure 5.9 shows that our approach using random discrete dopants in 2-D MC can successfully reproduce the impurity scattering properties for a wide range of doping concentrations. For the mobility fitting, we divided the doping concentration into three parts, and a different regression model is used for each region. Using the method, the granular effect can be included in the 2-D MC framework, and accordingly, simulation time and complexity can be improved significantly.

Moreover, during the procedure, we investigated the properties and the limitations of the 2-D MC simulation. In 3-D, the Coulomb scattering can be accounted for when meshes between charges are fine enough, which is equivalent to P^3M. On the other hand, in 2-D, Coulomb scattering cannot be treated by fine mesh since the force between charge particles is too weak as we observed in Table 5.1.

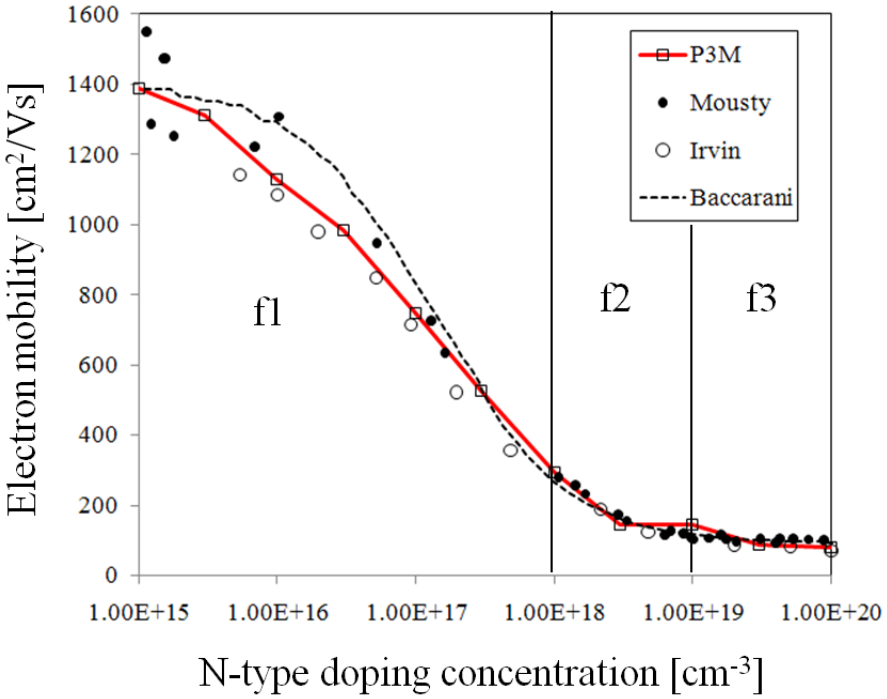

Figure 5.9: Low-field electron mobility as a function of doping concentration of bulk silicon at 300 K. Open and closed circles are the measurement data in [62] and in [63], respectively. The broken line is best fit for [64]. These data are also introduced in [65]. Three fitting models are used for the specified regions.

5.3 Conclusion

In this chapter, the 2-D P^{3}M method is developed for the first time to treat the Coulomb interaction based on the modified 3-D P^{3}M approach. Even with the limitations of 2-D, the method can be attractive considering the simplicity and less computational cost over 3-D. The equation for the direct force and for the numerical reference force is obtained by Gauss's law to find the electric field between two line charges. The accuracy of the equation is confirmed by the comparison with the 2-D Poisson's solution.

The main challenge for the 2-D P^{3}M is due to the line charge approximation, which is the intrinsic limitation of the 2-D transport simulation.

Our evaluation results reveal that the direct pair forces in 2-D are not strong enough to

represent the strong coulombic interactions of short-range charge particles. To cope with the problem, we introduce a quasi 3-D approach, in which we generate random positions of charge particles in an imaginary third direction. By doing so, we can evaluate the 3-D distance inside the 2-D short range, and accordingly the Coulomb's law as in 3-D can be applied to consider strong interaction between particles.

We show that the distribution function can be modulated by fitting parameters to mimic the shape of the 3-D distribution function by limiting the influence of carrier-carrier interaction and enhancing the influence of carrier-impurity scattering.

The mobility curve is also obtained by the method, which matches well with the measured data. In this evaluation, three simple regression models are used for the fitting of three different doping ranges. The same parameters used for the modification of the distribution function are used for the purpose.

The integration and evaluation of the method yielded valuable comparisons between the 2-D and 3-D EMC method. In 3-D, the Coulomb interactions can be accounted for depending on the mesh size. This will result in some double computation of the Coulomb scattering especially when we also apply scattering rate method.

However, in 2-D the Coulomb scattering will not be considered even with the fine mesh. The solution can be using scattering rate method or using 2-D P^3M method as shown in this chapter. Considering the limitation of the scattering method, the 2-D P^3M method can be a good option. We believe that it is still the early stage of 2-D P^3M development and there is room for improvement of the method.

CHAPTER 6

SUMMARY

In this study, a modified particle–particle–particle–mesh (P^3M) method is developed to treat Coulomb scattering, i.e. carrier-carrier scattering and carrier-impurity scattering. Even though the scattering rate method based on Fermi's golden rule is popular for the consideration of Coulomb interaction, there are many problems associated with the approach.

A promising alternative, the P^3M method, is known as a very accurate and efficient method to calculate inter-particle forces for many particle systems with less computational burden. However, it has not been widely used in semiconductor device simulation.

We believe that the double counting issue due to the overlap of the simulation domain and the uncertainty in the existing solution, i.e. the analytical reference force, are responsible for the difficulties in the application of the P^3M method.

In our study, the ambiguity of the analytical solution for the reference force was eliminated by introducing a straightforward numerical reference force evaluation scheme. In the method, Coulomb's law and the PP method are used to evaluate local mesh forces induced by local charge particles. The improvement of accuracy and efficiency over the existing solution have been verified with various applications including the variations of short-range radius, charge assignment scheme, and mesh scheme. Furthermore, we showed that the accuracy of the method can be even better with the application of fitting parameters which can be obtained using the properties of discrepancy between the PM and the PP method.

The shortcomings of the PM based scattering rate method have been revealed as we compared the properties with the P^3M based method. The energy of the carrier can decrease during the short-range Coulomb interaction, which is due to the limitation of the PM method. On the other hand, the energy can be maintained for a wide range of mesh size with the

application of P^3M. Accordingly, we can reduce the number of meshes and have corresponding speed gain while maintaining accuracy.

P^3M-EMC simulation with discrete dopants showed that the average energy of carriers inside the contact can be much higher than previously thought. The change was explained with the concept of electrostatic potential energy. The increase of carrier energy also considerably changes the device characteristics inside the channel region.

The validity of the modified P^3M-EMC was confirmed with the mobility extraction using an n-type resistor. The scattering rate method, e.g. Ridley's model, also can reproduce the mobility curve. However, it is doubtful whether the non-linear behavior of carriers inside the channel can also be treated by the approach. On the other hand, in the P^3M-EMC method, the mobility curve is obtained by long-range electrostatic simulation and short-range Coulomb's law, which is expected to hold even inside the channel.

The influences of carrier-carrier and carrier-impurity scattering were compared and the results showed that the impurity scattering is more influential inside the contact region. We believe that the main difference comes from the nature of the forces. In other words, the attraction force between carrier and impurity can be more influential than the repulsive force between carriers. Accordingly, carrier-carrier scattering can be treated by the PM method with reasonable mesh size.

In order to take advantage of the accuracy of P^3M-EMC, an attempt has been made to analyze random dopants fluctuation (RDF) with the variation of source/drain doping and channel doping. The results show the possibility that the simulation can provide a guideline for the variability analysis.

A two-dimensional P^3M-EMC method was introduced. An equation for the electric field calculation between line charges was applied for the reference force calculation. We also showed that the direct force between line charges was too weak to represent the proper interactions between charge particles in reality. To treat the problem, we introduced a quasi 3-D approach, which enabled us to use the same approach with the case of 3-D.

We believe that the modified P^3M approach in 3-D has significantly improved the accu-

racy and applicability of the original P^3M method and can be used widely for the consideration of Coulomb scattering. Moreover, the proposed 2-D P^3M can be a promising option to consider the granularity of the carrier and ionized impurities in 2-D simulation frame.

REFERENCES

[1] D. Antoniadis, I. Aberg, C. N. Chleirigh, O. Nayfeh, A. Khakifirooz, and J. Hoyt, "Continuous MOSFET performance increase with device scaling: The role of strain and channel material innovations," *IBM Journal of Research and Development*, vol. 50, pp. 363–376, July 2006.

[2] B. Yu et al., "FinFET scaling to 10nm gate length," in *IEDM Technical Digest*, 2002, pp. 251–254.

[3] G. Pei and J. Kedzierski, "FinFET design considerations based on 3-D simulation and analytical modeling," *IEEE Transactions on Electron Devices*, vol. 49, pp. 1411–1419, 2002.

[4] G. Kathawala, B. Winstead, and U. Ravaioli, "Monte Carlo simulations of double-gate MOSFETs," *IEEE Transactions on Electron Devices*, vol. 50, pp. 2467–2473, 2003.

[5] B. Doyle and S. Datta, "High performance fully-depleted tri-gate CMOS transistors," *IEEE Electron Device Letters*, vol. 24, pp. 263–265, 2003.

[6] A. Sharma and S. Zaidi, "Mobility and transverse electric field effects in channel conduction of wrap-around-gate nanowire MOSFETs," *IEE Proceedings Circuits, Devices, and Systems*, vol. 151, pp. 422–430, 2004.

[7] H. Takato et al., "High performance CMOS surrounding gate transistor (SGT) for ultra high density LSIs," in *IEDM Technical Digest*, 1988, pp. 222–225.

[8] "Monte Carlo simulation of semiconductor devices," 2011. [Online]. Available: http://www.research.ibm.com/DAMOCLES/home.html

[9] M. Fischetti et al., "Scaling MOSFETs to 10 nm: Coulomb effects, source starvation, and virtual source model," *Journal of Computational Electronics*, vol. 8, no. 2, pp. 60–77, 2009.

[10] K. Tomizawa, *Numerical Simulation of Submicron Semiconductor Devices*. Norwood, MA: Artech House, 1993.

[11] W. Lee and U. Ravaioli, "A simple and efficient method for the calculation of carrier-carrier scattering in Monte Carlo simulations," in *IEEE International Conference on Simulation of Semiconductor Processes and Devices (SISPAD)*, 2010, pp. 131–134.

[12] C. J. Wordelman and U. Ravaioli, "Integration of a particle–particle–particle–mesh algorithm with the ensemble Monte Carlo method for the simulation of ultra-small semiconductor devices," *Electron Devices*, vol. 47, pp. 410–416, 2000.

[13] C. Jacoboni and L. Reggiani, "The Monte Carlo method for the solution of charge transport in semiconductor with application to covalent materials," *Reviews of Modern Physics*, vol. 55, pp. 645–705, 1983.

[14] S. Barraud, P. Dollfus, S. Galdin, and P. Hesto, "Short-range and long-range coulomb interactions for 3D Monte Carlo device simulation with discrete impurity distribution," *Solid-State Electronics*, vol. 46, pp. 1061–1067, 2002.

[15] W. J. Gross, D. Vasileska, and D. K. Ferry, "A novel approach for introducing the electron-electron and electron-impurity interactions in particle–based simulations," *IEEE Electron Device Letters*, vol. 20, pp. 463–465, 1999.

[16] S. M. Sze, *Physics of Semiconductor Devices*. New York, NY: J. Wiley and Sons, 1981.

[17] W. S. Choi and J. K. Ahn, "A time dependent hydrodynamic device simulator SNU-2D with new discretization scheme and algorithm," *IEEE Transactions on CAD*, vol. 13, p. 898, 1994.

[18] A. Forghieri and R. Guerrieri, "A new discretization strategy of the semiconductor equations comprising momentum and energy balance," *IEEE Transactions on CAD*, vol. 7, p. 231, 1988.

[19] M. V. Fischetti and S. E. Laux, "Monte Carlo analysis of electron transport in small semiconductor devices including band-structure and space-charge effects," *Physical Review B*, vol. 38, pp. 9721–9745, 1988.

[20] M. V. Fischetti and S. E. Laux, "Monte Carlo study of electron transport in silicon inversion layers," *Physical Review B*, vol. 48, pp. 2244–2274, 1993.

[21] Z. Aksamija, "Simulation of thermal effects in semiconductor materials and devices," Ph.D. dissertation, University of Illinois at Urbana-Champaign, 2009.

[22] M. S. Lundstrom, *Fundamentals of Carrier Transport*, 2nd ed. Cambridge, UK: Cambridge Univ. Press, 2000.

[23] C. Jacoboni and P. Lugli, *The Monte Carlo Method for Semiconductor Device Simulation*. New York, NY: Springer-Verlag, 1989.

[24] H. Kosina and M. Nedjalkov, "The Monte Carlo method for semi-classical charge transport in semiconductor devices," *Mathematics and Computer in Simulation*, vol. 55, pp. 93–102, 2001.

[25] W. Fawcett, A. D. Boardman, and S. Swain, "Monte Carlo determination of electron transport properties in gallium arsenide," *Journal of Physics and Chemistry of Solids*, vol. 27, pp. 1963–1990, 1970.

[26] A. Duncan, U. Ravaioli, and J. Jakumeit, "Full-band Monte Carlo investigation of hot carrier trends in the scaling of MOSFETs," *IEEE Transactions on Electron Devices*, vol. 45, pp. 90–96, 1996.

[27] K. Hess, *Monte Carlo Device Simulation: Full Band and Beyond*. Norwell, MA: Kluwer Academic Publishers, 1991.

[28] K. Hess, *Advanced Theory of Semiconductor Devices*. New York, NY: IEEE Press, 2000.

[29] W. McMahon, A. Haggag, and K. Hess, "Reliability scaling issues for nanoscale devices," *IEEE Transactions on Nanotechnology*, vol. 2, pp. 33–38, 2003.

[30] J. Jakumeit, U. Ravaioli, and K. Hess, "Calculation of hot electron distributions in silicon by means of an evolutionary algorithm," *Journal of Applied Physics*, vol. 80, pp. 5061–5066, 1996.

[31] A. Kepkep and U. Ravaioli, "3-D parallel Monte Carlo simulation of sub-0.1 micron MOSFETs on a cluster based supercomputer," *Journal of Computational Electronics*, vol. 1, pp. 171–174, 2002.

[32] A. Pacelli, "Transport phenomena and hot electron effects in scaled MOSFET devices," Ph.D. dissertation, Polytechnic Institute of Milan, Italy, 1997.

[33] G. A. Kathawala, M. Mohamed, and U. Ravaioli, "Monte Carlo simulation of double-gate MOSFETs," *IEEE Transactions on Eelectron Devices*, vol. 50, pp. 2467–2473, 2003.

[34] G. A. Kathawala, "Monte Carlo simulation of nanostructures: Semiconductor devices to ion channels," Ph.D. dissertation, University of Illinois at Urbana-Champaign, 2005.

[35] B. Winstead, "Monte Carlo simulation of silicon devices including quantum correction and strain," Ph.D. dissertation, University of Illinois at Urbana-Champaign, 2001.

[36] C. Wordelman, "Three-dimensional granular Monte Carlo simulation of semiconductor devices," Ph.D. dissertation, University of Illinois at Urbana-Champaign, 2000.

[37] A. Trellakis, "Computational approaches to silicon based nanostructures," Ph.D. dissertation, University of Illinois at Urbana-Champaign, 2000.

[38] C. H. Lee, "Full band ensemble Monte Carlo simulation of silicon devices," Ph.D. dissertation, University of Illinois at Urbana-Champaign, 1994.

[39] J. R. Chelikowsky and M. L. Cohen, "Nonlocal pseudopotential calculations for the electronic structure of eleven diamond and zinc-blend semiconductors," *Physical Review B*, vol. 14, pp. 556–582, 1976.

[40] M. L. Cohen and T. Bergstresser, "Band structures and pseudopotential form factors for fourteen semiconductors of the diamond and zinc-blende structures," *Physical Review*, vol. 141, pp. 789–796, 1966.

[41] M. S. Lundstrom and J. Guo, *Nanoscale Transistors: Device Physics, Modeling and Simulation*. New York, NY: Springer, 2006.

[42] E. Cartier, M. Fischetti, E. Eklund, and F. Feely, "Impact ionization in silicon," *Applied Physics Letter*, vol. 62, pp. 3339–3341, 1993.

[43] J. Tang and K. Hess, "Impact ionization of electrons in silicon (steady state)," *Journal of Applied Physics*, vol. 54, pp. 5139–5144, 1983.

[44] R. M. Yorston, "Free-flight time generation in the Monte Carlo simulation of carrier transport in semiconductors," *Journal of Computational Physics*, vol. 64, pp. 177–194, 1986.

[45] Y. Taur and T. H. Ning, *Fundamentals of Modern VLSI Devices*. Cambridge, UK: Cambridge Univ. Press, 1998.

[46] D. K. Ferry, "The onset of quantization in ultra-submicron semiconductor devices," *Superlattice Microstructures*, vol. 27, pp. 61–66, 2000.

[47] B. Winstead and U. Ravaioli, "A quantum correction based on Schrödinger equation applied to Monte Carlo device simulation," *IEEE Transactions on Electron Devices*, vol. 50, pp. 440–446, 2003.

[48] H. Hahm, "Enhancement of Monte Carlo simulations on 3d nanoscale semiconductor devices," Ph.D. dissertation, University of Illinois at Urbana-Champaign, 2008.

[49] R. W. Hockney and J. W. Eastwood, *Computer Simulation Using Particles*. New York, NY: McGraw-Hill, 1981.

[50] B. K. Ridley, "Reconciliation of the Conwell-Weisskopf and Brooks-Herring formulae for charged-impurity scattering in semiconductors: Third-body interference," *Journal of Physics C: Solid State Physics*, vol. 10, pp. 1586–1593, 1977.

[51] A. W. Duncan, "Full-band Monte Carlo simulation of hot electrons in scaled silicon devices," Ph.D. dissertation, University of Illinois at Urbana-Champaign, 1996.

[52] H. Couchman, "Mesh-refined p^3m: A fast adaptive n-body algorithm," *The Astrophysical Journal Letters*, vol. 368, pp. 23–26, 1991.

[53] J. Navarro, C. Frenk, and D. White, "A universal density profile from hierarchical clustering," *The Astrophysical Journal*, vol. 490, pp. 493–508, 1997.

[54] A. Balasubramanian, P. R. Fleming, B. L. Bhuva, O. A. Amusan, and L. W. Massengill, "Effects of random dopant fluctuations (RDF) on the single event vulnerability of 90 and 65 nm CMOS technologies," *IEEE Transactions on Nuclear Science*, vol. 54, pp. 2400–2406, 2007.

[55] M. H. Chiang, J. N. Lin, K. W. Kim, and C. T. Chuang, "Discrete dopant fluctuation in limited-width FinFETs for VLSI circuit application: A theoretical study," in *IEEE International Conference on ICICDT*, 2010, p. 104.

[56] L. Du and S. Zhang, "RDF effect induced by source/drain doping in nano-scale UTB SOI MOSFET with nominally un-doped channel," in *IEEE International Conference on EDSSC*, 2006, pp. 1–4.

[57] G. Roy, A. R. Brown, F. Adamu-Lema, S. Roy, and A. Asenov, "Simulation study of individual and combined sources of intrinsic parameter fluctuations in conventional nano-MOSFETs," *IEEE Transactions on Electron Devices*, vol. 53, pp. 3063–3070, 2006.

[58] T. Tanaka, T. Usuki, T. Futatsugi, Y. Momiyama, and T. Sugii, "V_{th} fluctuation induced by statistical variation of pocket dopant profile," in *IEDM Technical Digest*, 2000, pp. 271–274.

[59] "International technology roadmap for semiconductors," 2009. [Online]. Available: http://www.itrs.net/Links/2009ITRS/Home2009.htm

[60] Y. Yamamoto, T. Hidaka, H. Nakamura, H. Sakuraba, and F. Masuoka, "Decananometer surrounding gate transistor (SGT) scalability by using an intrinsically-doped body and gate work function engineering," *IEICE Transactions on Electronics*, pp. 560–567, 2006.

[61] V. Ryzhii, A. Satou, W. Knap, and M. S. Shur, "Plasma oscillations in high-electron-mobility transistors with recessed gate," *Journal of Applied Physics*, vol. 99, pp. 084 507/1–5, 2006.

[62] J. Irvin, "Resistivity of bulk silicon and of diffused layers in silicon," *Bell System Technical Journal*, vol. 41, pp. 387–410, 1962.

[63] F. Mousty, P. Ostoja, and L. Passari, "Relationship between resistivity and phosphorus concentration in silicon," *Journal of Applied Physics*, vol. 45, pp. 4576–4580, 1974.

[64] G. Baccarani, "Electron mobility empirically related to the phosphorus concentration in silicon," *Solid-State Electronics*, vol. 18, pp. 579–580, 1975.

[65] C. Jacoboni, C. Canali, G. Ottaviani, and A. A. Quaranta, "A review of some charge transport properties of silicon," *Solid-State Electronics*, vol. 20, pp. 77–89, 1987.

AUTHOR'S BIOGRAPHY

Wonsok Lee was born in Kyungpook province in Korea on December 11, 1973. He received a bachelor's degree in 1999 and a master's degree in 2001 at Kyungpook National University in Daegu, Korea. Since 2001, he has worked for the TCAD group in Samsung Electronics and received sponsorship from the company for his Ph.D. study in 2005. He started his Ph.D. at the University of Illinois at Urbana-Champaign in 2006.